博士論文（要約）

Theoretical Analysis on Wave Dynamics in Cellular Chaotic Neural Networks

（セルラーカオスニューラルネットワークの波動ダイナミクスに関する理論的解析）

李 楊
(Yang Li)

指導教員:　合原一幸 教授
(Prof. Kazuyuki Aihara)

December 8, 2017

東京大学大学院　情報理工学系研究科　数理情報学専攻

Abstract

Wave dynamics emerge widely in spatially extended dynamical systems, including biological and artificial neural networks. This thesis investigates the wave dynamics in a cellular chaotic neural network (CNN) under simplified settings, dealing with both characterization and control of waves. Specifically, the plane wave dynamics is studied from the point of view of local bifurcation theory with an emphasis on the Bogdanov–Takens (BT) bifurcation; and the control of spiral wave dynamics is considered on the basis of a dynamic phase space constraint (DPSC) method.

First, to facilitate the BT bifurcation analysis, computation of its parameter-dependent normal form on the center manifold for n-dimensional, m-parameterized continuous-time systems is studied using the homological method. In the general case, a revision to the existent result on the parameter transformation is obtained, which is necessary for determining the bifurcation diagrams to the second order. In the case of enduring equilibria, simple formulas are obtained for the transformation of parameters, enabling the formulation of explicit transversality conditions and bifurcation diagrams to at most the second order. Moreover, in $\mathbf{Z}_2$-symmetric systems, the calculation can be further limited within certain subspaces. These results either revise or simplify existent studies, thereby facilitating quick computation of parametric normal forms for BT bifurcations in applications.

Next, the previously derived formulas are used to analyze the plane wave dynamics in the neural field model of the cellular CNN, which is a variant reaction-diffusion system with a singular and nonlinear spatial coupling. The BT bifurcation occurs in the three-dimensional traveling wave system for all wave speed values, indicating the existence of periodic waves, fold of periodic waves, and solitary waves with relatively high speeds, and periodic waves and single fronts/backs with slow speeds. The occurrence of the Bautin bifurcation reveals the existence of fold of periodic waves with relatively slow speeds as well. Moreover, the approximate dispersion relation for small-amplitude periodic waves is obtained, and the stability of these waves is analyzed. All these results are also verified or supplemented by numerical continuation studies. This part of research describes the overall plane wave dynamics in oscillatory media (with a $\mathbf{Z}_2$ symmetry) in the parameter space, serving as a supplement to the existent analysis of plane wave dynamics in typical excitable media.

Finally, the spiral wave dynamics in the simplified cellular CNN is investigated. It is shown by simulation that random initial conditions lead to stably rotating chaotic spiral

waves in the network, which demonstrate amplitude reduction near the phase singularity. A DPSC method is proposed for eliminating the spiral waves, where a control signal is constructed to indicate the presence of spiral waves and a limiting threshold modulated by the control signal is imposed on the refractory internal state of the network. Such a control scheme turns out to be successful in redirecting the network from a spiral wave state into either a plane wave (PW) state or a synchronized oscillation (SO) state. The pre-, intra-, and post-control dynamics exhibit different characteristics in the frequency domain; the PW-inducing and SO-inducing control processes are also distinct. Furthermore, a partial selectivity of the control results between PW and SO by varying the control parameters is discovered. This scheme surpasses existent methods of removing spiral wave in the sense that not only homogeneous states are produced and that the control does not need to be turned off manually.

The results of this thesis provide fundamentals of the traveling wave dynamics in the cellular CNN and may help to facilitate the future application of such networks. These results may also be beneficial to the study of wave dynamics in other spatially extended dynamical systems.

Keywords Bogdanov–Takens bifurcation, Parameter-dependent normal form, Chaotic neural network, Variant reaction-diffusion system, Traveling wave, Spiral wave, Chaos control, Dynamic phase space constraint

Contents

Chapter 1

Introduction

Traveling waves are quite ubiquitous phenomena: water waves, sound waves, and electromagnetic waves, etc. Generally, they are the spatial propagation of some abstract local motions (e.g., oscillations), where the state (e.g., phase) of an oscillator, rather than the oscillator itself, is transferred to other oscillators in certain directions. Traveling waves fall into different types in appearance: the most important might be periodic traveling waves (or called wave-trains), where the periodicity exists in both time and space; we can also have solitary waves (which are single pulses) and even single wave fronts/backs; with two and more spatial dimensions, spiral and scroll waves may appear. In the mathematical aspect, traveling waves play a fundamental role as the solutions to many spatially extended dynamical systems in both continuous and discrete forms [85], ranging from partial differential equations [95, 98] to cellular automata [15, 20, 65, 106]. These systems usually feature oscillatory or excitable local dynamics and diffusion-like spatial coupling, and they are widely used to model various real-world physical, chemical, neural, and ecological systems that accommodate traveling waves.

Traveling waves in the cortex

With the flourish of neuroscience, traveling waves in the vertebrate brain are attracting increasing attention. People have discovered traveling waves with different physiological origins, such as those with glial [29, 73] or hemodynamic [6] origins; nevertheless, the most studied species is the traveling waves of subthreshold activity, detected by multi-site monitoring of voltage-sensitive dyes, the local field potential, or other signals. The strong local synaptic connection between neurons forms an important physiological basis of the occurrence of such traveling waves.

The traveling waves of subthreshold activity are observed extensively in the neocortex [19, 71, 78, 79, 90, 99], as well as in the limbic system, such as the olfactory bulb [51] and the hippocampus [54, 104]. Spontaneous and evoked waves are both observed, which might play vital functional roles in signal integration over large regions [79] and information transmission between distributed brain parts [71]. Furthermore, these waves can

increase the probability and modulate the timing of single-neuronal firing, so traveling waves of spiking activity can be present with a similar pattern [79].

A particularly interesting type of traveling wave is the spiral wave, whose wave speed depends on the curvature of a wavefront, and the wavefronts of all phases intersect at a phase singularity. Such a topological defect in biological tissues may be pathological: a famous and well-studied example is that spiral waves underlie cardiac fibrillation [28, 68]. Recently, the involvement of cortical spiral waves in triggered and induced mammalian epileptic seizures has been demonstrated [89, 94]. Moreover, spiral waves are believed to be essential for the normal cortical functions by serving as rhythmic organizers of neuronal populations [100]. They depolarize the area surrounding a phase singularity in a mild and regular manner, thereby tuning the ongoing activity to higher excitable states to enhance responses during sensory processing.

Experimental studies have also demonstrated the differences between the cortical spiral waves in vivo and in vitro, using the technique of voltage-sensitive dye imaging [38, 39]. It is found that the cortical spiral waves in vivo generally have higher drift speeds, large dimensions of amplitude reduction, and shorter lifespans (before or after they evolve into or emerge from other states, respectively). These differences are believed to result from the long-range corticocortical or thalamocortical connections in the intact brain, which had been removed in a brain slice. In other words, these results indicate the existence of biological autonomous mechanisms for controlling the genesis, progression and termination of spiral waves in intact cortices, although the specific control scheme still remains unclear.

Traveling waves in neural networks

Spatially extended dynamical systems can be classified based on the continuousness and discreteness of their time, space and state variables [41]. For partial differential equation, all three items are continuous; when the space is discretized into elements, we get coupled differential equations or continuous-time neural networks; when both space and time are discretized, we obtain coupled lattice maps or discrete-time neural networks; for cellular automata, all three items are discrete. Traveling waves can be generated in systems of all types listed above, including cellular (i.e., locally-connected) neural networks [17].

Neural networks can be constructed using biologically realistic neuron models to develop platforms for the investigation of neurodynamics. Some important neuron models are the FitzHugh–Nagumo neuron, Hindmarsh–Rose neuron, and Hodgkin–Huxley neuron, and they are all expressed by ordinary differential equations. In cellular neural networks that comprise neurons of each of these species, traveling waves have been reported (see [22] for FitzHugh–Nagumo, [57] for Hindmarsh–Rose, and [102] for Hodgkin–Huxley neural networks, respectively). In addition, neural networks composed of other elements such as Chua oscillators [75] are also feasible media for traveling waves.

As for discrete-time neural networks, we pay particular attention to the chaotic neural network (CNN) proposed by Aihara et al [2]. Composed of chaotic neurons that manifest

chaotic dynamics similar to biological neurons, the CNN provides possible properties for both physiological and practical functionality. Specifically, it has attracted much interest as a prototype for dynamic associative memory [1, 3, 34, 46, 97]. In contrast to a convergent Hopfield network, the output of an associative CNN exhibits seemingly random itinerancy among all the basal patterns. Furthermore, when the weight connections in the associative CNN are local, traveling waves can be generated. Wave-like pattern formation behavior was observed in a cellular CNN where several colors are encoded [66]; subsequently, in large-scale cellular CNNs implementing color image association, multiple types of traveling waves, including plane waves (PWs), crossing PWs, and spiral waves of activation of stored patterns, were identified [67]. These results provide a novel mechanism of association as propagating alterations of local cell assemblies, rather than the conventional association scheme of global state transitions.

We should note that controlling the dynamics of neural networks as dynamical systems is also of interest. For example, the method of inducing target waves by periodic injection to suppress spiral waves was first proposed for excitable media that model CO catalytic oxidation and cardiac muscle [103]; this method was later applied to eliminate the spiral waves in the network of Hodgkin–Huxley neurons [59]. On the other hand, although there have been a series of studies proposing various methods of controlling the chaotic dynamics in fully-connected associative CNNs to facilitate their application [33, 34, 35, 36, 52], corresponding control methods for cellular associative CNNs that are able to modulate their traveling wave behavior, are still absent.

Traveling waves and bifurcations

As mentioned above, traveling waves emerge in both real and artificial neural networks, which are composed of individual neurons and are hence spatially discrete. If we concentrate on the collective wave behavior (e.g., plane waves) on a macroscopic scale rather than the pattern formation within small neuron assemblies, then a cellular neural network can be approximated as a continuous medium. Thus, the traveling waves in the original networks are approximated by the traveling wave solutions to the corresponding neural field models, expressed in partial differential equations.

The clarification of the behavior of these traveling wave solutions in parameter spaces can be done using bifurcation theory; such kind of study was initiated by Kopell and Howard [45]. By considering the Hopf bifurcation in the traveling wave equations obtained from reaction-diffusion equations, they proved the existence of a one-parameter family of plane wave solutions, under certain hypotheses for the Jacobian matrix of the equilibrium and the diffusion matrix. They also investigated the linear stability of the plane waves and concluded that with a near-identity diffusion matrix, small-amplitude waves are unstable. The famous λ–ω system, which comprises a circular limit cycle oscillation and a linear scalar diffusion term, was analyzed to illustrate their major results.

This research scheme later becomes quite standard and has been used to analyze the traveling wave solutions of many partial differential equations, ranging from the famous FitzHugh–Nagumo equation [13, 26, 27] and complex Ginzburg–Landau equation [60, 69, 70] to some less known equations (see [101], [105] and the references therein for examples). Typically, periodic traveling wave solutions with an infinitesimal amplitude emerge form Hopf bifurcations; with the changes of parameters, the period of these traveling waves might approach infinity as a result of homoclinic bifurcations, where they become solitary wave solutions. Bifurcation analysis also helped people to understand the traveling wave solutions to the partial differential equations that model many specific real-world systems, such as calcium in pancreatic acinar cells [88], gas-fluidized beds [21], multimode lasers [11], and population dynamics [9, 74]. We note that the emergence and annihilation of traveling waves can be due to other bifurcations as well [44].

The analysis of higher-codimensional bifurcations may provide more information about the traveling wave solutions [76]. By considering multiple parameters at a time, the bifurcation diagram usually contains multiple bifurcation boundaries of lower-codimensional bifurcations. For example, the generalized Hopf bifurcation of codimension two (Bautin bifurcation) involves supercritical and subcritical Hopf bifurcations together with a saddle-node bifurcation of limit cycles; the Bogdanov–Takens (BT) bifurcation of codimension two involves fold, Hopf, and homoclinic bifurcations, and in some cases, the heteroclinic bifurcation or saddle-node bifurcation for limit cycles can be involved. In this way, the analysis of such bifurcations may give further information about the existence of solitary waves, traveling fronts/backs, (coexisting) multiple periodic traveling waves and the corresponding parameter values or regions than the analysis of Hopf bifurcations only. The higher-codimensional bifurcations in typical excitable media (for example, the FitzHugh–Nagumo equation) has been investigated in [13, 26, 27]

Objective and content of the present thesis

This thesis sets foot in the investigation of the traveling wave dynamics in cellular chaotic neural networks under simplified conditions, concerning especially the fundamental characteristics of periodic plane waves and possible control schemes for chaotic spiral waves. To explore the parameter dependence of the traveling wave behavior, bifurcation analysis is carried out with an emphasis on the codimension-two BT bifurcation, for which we find simple formulas for the parametric center manifold reduction. These studies serve as essential preparations for further attempts of applying the cellular chaotic neural networks in memory retrieval and other information processing tasks as well as finding clues for the regulation of traveling wave dynamics in real nervous systems.

The content of this thesis is organized as follows:

In **Chapter 2**, we introduce briefly the fundamental notions of local bifurcation theory, including the key concepts such as topological equivalence, bifurcation, normal form, center manifold reduction, and some specific types of local bifurcations. Moreover, the derivation

of the normal forms for the BT bifurcation in planar systems will be explained in detail, which will be used directly as fundamentals during the generalization to n-dimensional systems ($n \geqslant 2$) in the next chapter.

Chapter 3 provides preparation for the following chapter, by considering the derivation of parameter-dependent normal forms of the BT bifurcation for n-dimensional, m-parameterized systems. Compared with some existent studies [12, 72], this thesis presents either revision or simplification, and hence enables quick determination of the parameter transformation and check of the transversality condition.

Specifically, in the general case where a saddle-node bifurcation is involved, a revision to the existing result is provided, which is necessary for determining the bifurcation diagrams up to the second order. More importantly, in the case of an enduring equilibrium where a transcritical or pitchfork bifurcation is involved, quite simple formulas are obtained for the transformation of parameters to the second order, leading to the formulation of explicit transversality conditions and bifurcation diagrams; moreover, in $\mathbf{Z}_2$-symmetric systems, the calculation can be further restricted within certain subspaces. The results facilitate the derivation of normal forms, check of transversality and depiction of bifurcation diagrams for the BT bifurcation.

In **Chapter 4**, a cellular chaotic neural network under simplified conditions is approximated to a neural field model with Liénard-type local dynamics and singular, nonlinear diffusive spatial coupling, for analyzing the plane wave dynamics in it. The plane waves in typical excitable media (the FitzHugh–Nagumo system) were analyzed from the angle of bifurcations in [13, 26, 27]; as a supplement, this thesis considers the plane waves in typical oscillatory media with symmetric local dynamics, which have different features.

The corresponding three-dimensional traveling wave system (with the two-dimensional local dynamics as its limit for the wave speed $c \to +\infty$) is analyzed with an emphasis on the BT bifurcation, using the technique given in the preceding chapter. The $\mathbf{Z}_2$-symmetric traveling wave system exhibits the BT bifurcation for every $c > 0$, indicating the existence of periodic waves, fold of periodic waves, and solitary waves with relatively high speed c, and periodic waves and traveling fronts with relatively low speed c. The Bautin bifurcation indicates fold of periodic waves for small c values as well. With the method of harmonic balance, the approximate dispersion relation of small-amplitude periodic plane waves is obtained. Moreover, a simple stability analysis shows that the periodic waves of sufficiently small amplitudes are unstable; the stability of periodic waves with larger amplitudes are investigated numerically.

In **Chapter 5**, the spiral wave dynamics in the cellular CNN is investigated, and a dynamic phase space constraint (DPSC) method is proposed to eliminate spiral waves. Different from previously existent methods [58, 84, 103] where the control must be stopped "manually" after a homogeneous state is obtained, the DPSC method can lead to not only homogeneous states (specifically, synchronized oscillation, SO) but also various PW states, where the control has automatically ceased.

In this method, a control signal is constructed from the feedback internal states of the neurons to detect phase singularities, before modulating a threshold value to truncate the refractory internal states of the neurons and terminate the spirals; then, the network was directed from a spiral wave state into either a PW state or an SO state. The intra-control and post-control dynamics were compared with the pre-control spiral wave dynamics, and the differences between the PW-inducing and SO-inducing control processes were also found. Furthermore, variations in the control parameter allowed partial selectivity of the control results, accompanied by modulated control processes. These results broaden the applicability of DPSC to chaos control, and may also facilitate the utilization of cellular CNNs in memory retrieval and the exploration of traveling wave dynamics in biological neural networks.

Finally, conclusions and prospects for this thesis are given in **Chapter 6**.

Chapter 2

Preliminaries of Local Bifurcation Theory

This chapter provides a brief introduction to the most fundamental concepts and notions of the bifurcation theory, with a focus on the local bifurcations that occurs at the equilibria of continuous-time dynamical systems. As an indispensable part of the qualitative theory of differential equations, "bifurcation" generally refers to the destruction of the topological equivalence relation of a family of systems, under variation of parameters. Different bifurcations are modeled by their corresponding normal forms; bifurcations occurring in high-dimensional systems are essentially represented by their restriction to an invariant center manifold of the lowest possible dimension. According to the minimum number of parameters needed for revealing their unfoldings, bifurcations are categorized into different codimensions. After introducing the codimension-one and codimension-two bifurcations, the codimension-two BT bifurcation is elucidated because of its particular importance in this thesis.

2.1 Topological equivalence

2.1.1 Topological equivalence relations

The topological equivalence relation of dynamical systems is used to indicate the qualitative similarity between the behavior of these systems; the necessary condition for such a similarity should include the same number, stability, and relative location of limit sets (equilibria and limit cycles, etc.); more precisely, two systems are pictured as equivalent, when a continuous function with a continuous inverse (i.e., a homeomorphism) relates their phase portraits. Hence people have the definition of topological equivalence [25, 47] as below.

Definition 1. *Two dynamical systems in $\mathbb{R}^n$ are topologically equivalent if there exists a homeomorphism $\boldsymbol{h} : \mathbb{R}^n \to \mathbb{R}^n$ that maps the orbits of one system to those of the other while preserving the direction of time.*

Definition 1 can be applied to both discrete- and continuous-time dynamical systems. For continuous-time systems, more strict equivalence relations are frequently used and can be viewed as sufficient conditions for the general topological equivalence in Definition 1. Considering the system

$$\dot{\boldsymbol{x}} = \boldsymbol{f}(\boldsymbol{x}), \quad \boldsymbol{x} \in \mathbb{R}^n, \tag{2.1}$$

and the system

$$\dot{\boldsymbol{y}} = \boldsymbol{g}(\boldsymbol{y}), \quad \boldsymbol{y} \in \mathbb{R}^n, \tag{2.2}$$

where $\boldsymbol{f}$ and $\boldsymbol{g}$ are smooth, we have the following definitions [47].

Definition 2. *Systems* (2.1) *and* (2.2) *are smoothly equivalent (or diffeomorphic) if there exists a diffeomorphism* $\boldsymbol{y} = \boldsymbol{h}(\boldsymbol{x})$ *such that, for all* $\boldsymbol{x} \in \mathbb{R}^n$,

$$\frac{\partial \boldsymbol{h}(\boldsymbol{x})}{\partial \boldsymbol{x}} \boldsymbol{f}(\boldsymbol{x}) = \boldsymbol{g}\left(\boldsymbol{h}(\boldsymbol{x})\right).$$

Definition 3. *Systems* (2.1) *and* (2.2) *are orbitally equivalent if there exists a smooth positive function* $r(\boldsymbol{x})$ *such that, for all* $\boldsymbol{x} \in \mathbb{R}^n$,

$$\boldsymbol{f}(\boldsymbol{x}) = r(\boldsymbol{x})\, \boldsymbol{g}(\boldsymbol{x}).$$

Definition 2 describes the situation where systems (2.1) and (2.2) can be transformed to each other by a smooth, invertible change of variables, $\boldsymbol{y} = \boldsymbol{h}(\boldsymbol{x})$; hence, the two systems are equivalent in almost every aspect and obviously satisfy the condition in Definition 1. Definition 3 describes the situation where the two systems can be obtained from each other by a time reparametrization (no reversal); thus, the orbits of these systems are identical everywhere in $\mathbb{R}^n$, only with different velocities of the phase point. In practice, people often combine smooth invertible changes of variables and time reparametrizations and use them repeatedly, to transform a system to a desired topologically equivalent form.

The preceding topological, smooth and orbital equivalences defined globally in $\mathbb{R}^n$ can also be defined locally for some region $U \subset \mathbb{R}^n$. To consider the topological equivalence of systems (2.1) and (2.2) near corresponding equilibria, we have the definition below [47].

Definition 4. *System* (2.1) *near an equilibrium* $\boldsymbol{x}_0$ *and system* (2.2) *near an equilibrium* $\boldsymbol{y}_0$ *are locally topologically equivalent, if there exist a homeomorphism* $\boldsymbol{h} : \mathbb{R}^n \to \mathbb{R}^n$ *defined in a neighborhood* U *of* $\boldsymbol{x}_0$ *that satisfy the following conditions*:

(i) $\boldsymbol{h}(\boldsymbol{x}_0) = \boldsymbol{y}_0$;

(ii) $\boldsymbol{h}$ *maps the orbits of* (2.1) *in* U *to those of* (2.2) *in* V $(V = \boldsymbol{h}(U))$ *while preserving the direction of time.*

In this situation, we may also say for simplicity that the two equilibria, $\boldsymbol{x}_0$ and $\boldsymbol{y}_0$, are topologically equivalent. To give an example, let us consider the planar systems

$$\begin{cases} \dot{x}_1 = -x_1, \\ \dot{x}_2 = -x_2, \end{cases} \quad \text{and} \quad \begin{cases} \dot{y}_1 = -y_1 - y_2, \\ \dot{y}_2 = y_1 - y_2, \end{cases}$$

where the origin is a stable node in the former system but a stable focus in the latter. This is clear as we can check that the homeomorphism $\boldsymbol{y} = \boldsymbol{h}(\boldsymbol{x})$, with $\boldsymbol{h}(\mathbf{0}) = \mathbf{0}$ and

$$\boldsymbol{h}(x_1, x_2) = \begin{bmatrix} \cos\ln\sqrt{x_1^2+x_2^2} & \sin\ln\sqrt{x_1^2+x_2^2} \\ -\sin\ln\sqrt{x_1^2+x_2^2} & \cos\ln\sqrt{x_1^2+x_2^2} \end{bmatrix} \begin{bmatrix} x_1 \\ x_2 \end{bmatrix}$$

for (x_1, x_2) near $(0, 0)$, satisfies the conditions of Definition 4. Such a node–focus equivalence will be further generalized as follows.

2.1.2 Classification of hyperbolic equilibria

We now present some important results on the classification of hyperbolic equilibria, which directly caters for the condition for the occurrence of local bifurcations of equilibria. First, we have the following definition for the so-called hyperbolic equilibrium.

Definition 5. *Let $\boldsymbol{x}_0$ be an equilibrium of system* (2.1) *where the Jacobian matrix has n_-, n_0, and n_+ eigenvalues whose real parts are negative, zero, and positive, respectively ($n_- + n_0 + n_+ = n$). Then, $\boldsymbol{x}_0$ is a hyperbolic equilibrium if $n_0 = 0$.*

A classification of hyperbolic equilibria can be carried out on the basis of local topological equivalence relations, according to two celebrated theorems in the theory of dynamical systems. One of them is the Hartman–Grobman theorem (or called linearization theorem), which asserts that the behavior of a nonlinear system in the neighborhood of a hyperbolic equilibrium is qualitatively the same as that of its linearization.

Theorem 1 ([23, 24, 30, 31])**.** *System* (2.1) *near its hyperbolic equilibrium $\boldsymbol{x}_0$ is locally topologically equivalent to the linearized system, $\dot{\boldsymbol{x}} = \mathbf{J}\boldsymbol{x}$, with $\mathbf{J} = \frac{\partial \boldsymbol{f}}{\partial \boldsymbol{x}}\big|_{\boldsymbol{x}=\boldsymbol{x}_0}$ the Jacobian matrix evaluated at $\boldsymbol{x} = \boldsymbol{x}_0$.*

The other theorem is due to Arnold [7], which gives the sufficient and necessary condition for two hyperbolic linear systems to be topological equivalent.

Theorem 2 ([7])**.** *Two linear systems* (2.1) *and* (2.2) *with hyperbolic equilibria are topologically equivalent, if and only if the numbers of eigenvalues with positive (or negative) real parts are equal for these systems.*

By Theorem 1, Theorem 2 can be generalized from two linear systems to two arbitrary systems: a hyperbolic equilibrium $\boldsymbol{x}_0$ of system (2.1) and a hyperbolic equilibrium $\boldsymbol{y}_0$ of system (2.2) are topologically equivalent, if and only if they have the same numbers n_- (or n_+). This fulfills a classification of all hyperbolic equilibria according to the values of n_+ and n_-. Moreover, the following conclusion is readily drawn: For a hyperbolic equilibrium of a parameter-dependent system, as all the eigenvalues of its Jacobian matrix keep away from the imaginary axis, the equilibrium remains locally topologically equivalent under a sufficiently small smooth parameter perturbation.

2.2 Bifurcations and normal forms

In real-world applications, all dynamical systems depend on some parameters. Specifically, people are interested in the behavior of parameter-dependent systems as a consequence of changed operating conditions or to account for uncertainties. Sometimes, even a slightest perturbation results in a sudden change and a qualitatively distinct system, as the straw that breaks the camel's back: we may say that the system is "structurally unstable" and undergoes a "bifurcation". In this section, the definitions of bifurcation, bifurcation diagram, codimension, and normal form of a bifurcation will be introduced. First, let us consider an n-dimensional, m-parameterized continuous-time system

$$\dot{\boldsymbol{x}} = \boldsymbol{f}(\boldsymbol{x}, \boldsymbol{\alpha}), \quad \boldsymbol{x} \in \mathbb{R}^n, \ \boldsymbol{\alpha} \in \mathbb{R}^m, \tag{2.3}$$

where $\boldsymbol{f}$ is smooth, and give the following definition.

Definition 6. *The parameter-dependent system* (2.3) *undergoes a bifurcation at a bifurcation point $\boldsymbol{\alpha} = \boldsymbol{\alpha}^*$, if in any neighborhood of $\boldsymbol{\alpha}^*$ there always exist values of $\boldsymbol{\alpha}$ such that system* (2.3) *is not topologically equivalent to $\dot{\boldsymbol{x}} = \boldsymbol{f}(\boldsymbol{x}, \boldsymbol{\alpha}^*)$.*

Simply speaking, bifurcation is the appearance of topological non-equivalence under variation of parameters; this applies to both continuous- and discrete-time systems. As can be expected, bifurcations can be local or global. If the variation of parameters only leads to a locally topologically non-equivalent system near an equilibrium, then the bifurcation is local. Otherwise, if the resultant topological non-equivalence cannot be detected in a small neighborhood of an equilibrium, then the bifurcation is said to be global. Following from the introduction in Sec. 2.1.2, it is clear that local bifurcations of an equilibrium only occur when the equilibrium is non-hyperbolic. The non-hyperbolicity of an equilibrium, i.e., existence of eigenvalues with zero real parts, is the (local) bifurcation condition, which locates a bifurcation point.

The set of parameter values where a bifurcation condition is satisfied (i.e., set of bifurcation points) is called a bifurcation boundary. Note that there are bifurcation conditions for global bifurcations, too, so that when the parameter crosses a bifurcation boundary, some bifurcation occurs. Then we have the following definition.

Definition 7. *A bifurcation diagram is a partition of the parameter space of a parameter-dependent system by the bifurcation boundaries for one or more bifurcations such that the system remains topologically equivalent within each region.*

Usually, the partition in a bifurcation diagram is accompanied by representative phase portraits. Besides, we note that the bifurcation boundary in a one-dimensional parameter space is a bifurcation point, but it can also be a bifurcation curve, a bifurcation surface, etc., in parameter spaces with sufficiently high dimensions. For instance, the bifurcation condition of a simple zero eigenvalue $\lambda_1 = 0$ gives a curve on the plane spanned by two parameters, while the bifurcation condition of a double-zero eigenvalue $\lambda_{1,2} = 0$ gives a point. Hence we have the following definition.

Definition 8. *The codimension of a bifurcation is the difference between the dimension of the phase space and the dimension of its corresponding bifurcation boundary.*

With this definition, the bifurcation that corresponds to a simple zero eigenvalue is of codimension one, and the bifurcation that corresponds to a double-zero eigenvalue is of codimension two. In other words, the codimension of a bifurcation can be understood as the minimum number of free parameters that are required to unfold that bifurcation.

By now we have been using the topological equivalence relation between non-parametric systems, or between parametric systems at different parameter values. The bifurcation-related concepts defined above may cause us to consider the equivalence of two families of systems collectively under parameter perturbations, or, the "equivalence relation" between bifurcation diagrams. This is handled by the definitions given below (according to [47]) for system (2.3) and another n-dimensional, m-parameterized system

$$\dot{\boldsymbol{y}} = \boldsymbol{g}(\boldsymbol{y}, \boldsymbol{\beta}), \quad \boldsymbol{y} \in \mathbb{R}^n,\ \boldsymbol{\beta} \in \mathbb{R}^m, \tag{2.4}$$

where $\boldsymbol{g}$ is a smooth function.

Definition 9. *Systems* (2.3) *and* (2.4) *are topologically equivalent if* (i) *and* (ii) *hold*:

(i) *there exists a homeomorphism* $\boldsymbol{T} : \mathbb{R}^m \to \mathbb{R}^m$ *of parameter spaces,* $\boldsymbol{\beta} = \boldsymbol{T}(\boldsymbol{\alpha})$,

(ii) *there exists a parametric homeomorphism* $\boldsymbol{h}_\alpha : \mathbb{R}^n \to \mathbb{R}^n$ *of phase spaces* $\boldsymbol{y} = \boldsymbol{h}_\alpha(\boldsymbol{x})$ *mapping the orbits of* (2.3) *at* $\boldsymbol{\alpha}$ *to those of* (2.4) *at* $\boldsymbol{\beta} = \boldsymbol{T}(\boldsymbol{\alpha})$ *while preserving the direction of time.*

Definition 10. *Systems* (2.3) *near* $(\boldsymbol{x}_0, \boldsymbol{\alpha}_0)$ *and* (2.4) *near* $(\boldsymbol{y}_0, \boldsymbol{\beta}_0)$ *are locally topologically equivalent if the following* (i) *and* (ii) *hold*:

(i) *there exists a homeomorphism* $\boldsymbol{\beta} = \boldsymbol{T}(\boldsymbol{\alpha})$ *defined in a neighborhood of* $\boldsymbol{\alpha} = \boldsymbol{\alpha}_0$ *such that* $\boldsymbol{\beta}_0 = \boldsymbol{T}(\boldsymbol{\alpha}_0)$,

(ii) *there exists a parametric homeomorphism* $\boldsymbol{y} = \boldsymbol{h}_\alpha(\boldsymbol{x})$ *defined in a neighborhood* U_α *of* $\boldsymbol{x} = \boldsymbol{x}_0$ *for every* $\boldsymbol{\alpha}$ *in a neighborhood of* $\boldsymbol{\alpha} = \boldsymbol{\alpha}_0$ *with* $\boldsymbol{h}_{\alpha_0}(\boldsymbol{x}_0) = \boldsymbol{y}_0$, *mapping the orbits of* (2.3)*) in* U_α *to those of* (2.4)*) in* $V_\beta = \boldsymbol{h}_\alpha(U_\alpha)$ *while preserving the direction of time.*

Definitions 9 and 10 generalize the topological equivalence first defined by Definitions 1 and 4 to parameter-dependent systems. In application, we may repeatedly make smooth invertible changes of state variables and time reparametrizations that preserve the direction of time, to transform a parameter-dependent system near a bifurcation into some highly reduced form. The final reduced system is expressed by a polynomial in its state variables, with least possible terms and hopefully with simplest possible coefficients.

Definition 11. *Consider system* (2.4)*, where* $\boldsymbol{y} = \boldsymbol{0}$ *is an equilibrium at* $\boldsymbol{\beta} = \boldsymbol{0}$ *and* $\boldsymbol{\beta} = \boldsymbol{0}$ *is a codimension-m bifurcation point. Assume that*

(i) $\boldsymbol{g}(\boldsymbol{y}, \boldsymbol{\beta})$ *is a polynomial in* $\boldsymbol{y}$*, with minimum possible terms up to a certain degree*,

(ii) *System* (2.4) *near* $(\mathbf{0}, \mathbf{0})$ *is locally topologically equivalent to any generic system* (2.3) *near* $(\boldsymbol{x}_0, \boldsymbol{\alpha}_0)$ *where the same bifurcation conditions are satisfied.*

Then the system (2.4) *can be called a topological normal form for this bifurcation.*

A different concept from the topological normal form is the truncated normal form, which is obtained by abandoning all terms in $\boldsymbol{y}$ higher than a certain degree in the reduced system (2.4). Sometimes, the truncated normal form is still a topological normal form. In some other situations, the behavior of a bifurcation depends on the higher-degree terms, and the truncated normal form is not a topological normal form. The process of transforming a generic system near a bifurcation to its normal form is called normalization. It should be noted that the word "generic" here and in Definition 11 has a meaning: certain genericity conditions should be satisfied. These include non-degeneracy conditions, requiring some critical coefficients to be nonzero during the normalization, and transvesality conditions, requiring the invertibility of the parameter transformation $\boldsymbol{\alpha} \mapsto \boldsymbol{\beta}$.

2.3 Center manifold theorem and reduction principle

Local bifurcations of an equilibrium occur when the equilibrium is non-hyperbolic, where the behavior of the system becomes more difficult to determine than the hyperbolic cases. An important simplification of a non-hyperbolic system is to reduce its dimension to n_0, i.e., the number of eigenvalues with zero real parts, with the help of the center manifold theorem and reduction principle.

Theorem 3 (Center manifold theorem, see [25, 47])**.** *For system* (2.1) *with a* C^r*-smooth function* $\boldsymbol{f}$ $(r \in N_+)$*, assume that* $\boldsymbol{x}_0$ *is a non-hyperbolic equilibrium whose Jacobian matrix has an* n_0*-dimensional (generalized) eigenspace* T^c *associated to the eigenvalues with zero real parts. Then there exists a locally defined,* C^r*-smooth,* n_0*-dimensional invariant manifold* M^c *of* (2.1) *that is tangent to* T^c*. Moreoever, if an orbit stays within a neighborhood* U *of* $\boldsymbol{x}_0$ *for all* $t > 0$ $(t < 0)$*, then the orbit converges to an orbit on* M_c *exponentially as* $t \to +\infty$ $(t \to -\infty)$*.*

The invariant manifold M^c is just a so-called center manifold. When all orbits that stay in U for positive t converge to M^c as $t \to +\infty$, M^c is said to be attracting; when all orbits staying in U for negative t converge to M^c as $t \to -\infty$, the center manifold is said to be repelling. Note that the center manifold of an equilibrium is not necessarily unique.

To reduce a non-hyperbolic system to its essential dynamics on the center manifold, we consider the system (2.1) rewritten in the following form after some affine transformation,

$$\begin{cases} \dot{\boldsymbol{u}} = \mathbf{A}\boldsymbol{u} + \boldsymbol{g}(\boldsymbol{u}, \boldsymbol{v}), \\ \dot{\boldsymbol{v}} = \mathbf{B}\boldsymbol{v} + \boldsymbol{h}(\boldsymbol{u}, \boldsymbol{v}), \end{cases} \tag{2.5}$$

where $\boldsymbol{u} \in \mathbb{R}^{n_0}$, $\boldsymbol{v} \in \mathbb{R}^{n_+ + n_-}$, $\mathbf{A}$ has all its eigenvalues on the imaginary axis while $\mathbf{B}$ has none, and $\boldsymbol{g}$ and $\boldsymbol{h}$ have vanishing linear parts in $\boldsymbol{u}$ and $\boldsymbol{v}$. Because of the tangency between M^c and T^c, the center manifold M^c can be expressed by a function $\boldsymbol{v} = \boldsymbol{M}(\boldsymbol{u}) : \mathbb{R}^{n_0} \mapsto \mathbb{R}^{n_+ + n_-}$. Then we have an important theorem as follows.

Theorem 4 (Reduction principle, see [47]). *System* (2.5) *is locally topologically equivalent to*

$$\begin{cases} \dot{\boldsymbol{u}} = \mathbf{A}\boldsymbol{u} + \boldsymbol{g}(\boldsymbol{u}, \boldsymbol{M}(\boldsymbol{u})), \\ \dot{\boldsymbol{v}} = \mathbf{B}\boldsymbol{v}, \end{cases} \tag{2.6}$$

near the equilibrium $\boldsymbol{x}_0$*. All the systems* (2.6) *that result from different center manifolds* $\boldsymbol{M}(\boldsymbol{u})$ *are locally smoothly equivalent to one another.*

With the reduction principle, the dynamics of the original non-hyperbolic system is successfully decomposed on and off the center manifold as the dynamics of $\boldsymbol{u}$ and $\boldsymbol{v}$ in (2.6), respectively. The former, i.e., the first equation in (2.6), is often called the restriction or restricted dynamics of system (2.5) to its center manifold $\boldsymbol{M}$. The latter can be replaced with $\dot{\boldsymbol{v}} = \mathbf{B}'\boldsymbol{v}$ but still keeping the whole system locally topologically equivalent, where $\mathbf{B}'$ has the same values n_+ and n_- as $\mathbf{B}$ does.

In the parameter-dependent scenario, similar conclusions as above can be obtained. We consider the parameter-dependent system (2.3) with $\boldsymbol{f}$ sufficiently smooth in $(\boldsymbol{x}, \boldsymbol{\alpha})$, and assume that a non-hyperbolic equilibrium $\boldsymbol{x}_0$ exists for $\boldsymbol{\alpha} = \boldsymbol{\alpha}_0$, as in the assumption of Theorem 3. Then, we apply the center manifold theorem to the extended system

$$\begin{cases} \dot{\boldsymbol{x}} = \boldsymbol{f}(\boldsymbol{x}, \boldsymbol{\alpha}), \\ \dot{\boldsymbol{\alpha}} = \mathbf{0}, \end{cases} \tag{2.7}$$

whose Jacobian matrix at $(\boldsymbol{x}_0, \boldsymbol{\alpha}_0)$ has exactly n_0+m zero or purely imaginary eigenvalues. Hence there exists an (n_0+m)-dimensional center manifold M^{ec} for the extended system, and for convenience, we define the (n_0-dimensional) parameter-dependent center manifold M^c_α for the original system (2.3) as

$$M^c_\alpha = M^{ec} \cap \left\{ (\boldsymbol{x}, \boldsymbol{\alpha}') | \boldsymbol{\alpha}' = \boldsymbol{\alpha} \right\}. \tag{2.8}$$

In analogy to Eq. (2.5), the original system (2.3) can be rewritten as

$$\begin{cases} \dot{\boldsymbol{u}} = \mathbf{A}(\boldsymbol{\alpha})\boldsymbol{u} + \boldsymbol{g}(\boldsymbol{u}, \boldsymbol{v}, \boldsymbol{\alpha}), \\ \dot{\boldsymbol{v}} = \mathbf{B}(\boldsymbol{\alpha})\boldsymbol{v} + \boldsymbol{h}(\boldsymbol{u}, \boldsymbol{v}, \boldsymbol{\alpha}), \end{cases} \tag{2.9}$$

where $\mathbf{A}(\boldsymbol{\alpha})$ has all its eigenvalues on the imaginary axis at $\boldsymbol{\alpha} = \boldsymbol{\alpha}_0$ while $\mathbf{B}(\boldsymbol{\alpha})$ has none in a neighborhood of $\boldsymbol{\alpha} = \boldsymbol{\alpha}_0$. Considering the tangency of $M^c_{\alpha_0}$ and T^c, we may express the parameter-dependent center manifold M^c_α near $(\boldsymbol{x}_0, \boldsymbol{\alpha}_0)$ by a function $\boldsymbol{v} = \boldsymbol{M}(\boldsymbol{u}, \boldsymbol{\alpha}) : \mathbb{R}^{n_0} \times \mathbb{R}^m \mapsto \mathbb{R}^{n_+ + n_-}$. Thus the restriction of Eq. (2.9) to the parameter-dependent center manifold is given by

$$\dot{\boldsymbol{u}} = \mathbf{A}(\boldsymbol{\alpha})\boldsymbol{u} + \boldsymbol{g}(\boldsymbol{u}, \boldsymbol{M}(\boldsymbol{u}, \boldsymbol{\alpha}), \boldsymbol{\alpha}). \tag{2.10}$$

The parameter-dependent locally topological equivalence of the original system (2.3) and the suspension of the restricted dynamics (2.10) by a corresponding saddle was due to Shoshitaishvili [83]. This result guarantees that a local bifurcation of equilibria in a high-dimensional system can be essentially captured by the restriction on its parameter-dependent center manifold, Eq. (2.10). Therefore, such a bifurcation in a high-dimensional system adds nothing new compared with the bifurcation occurring in a system with a minimum required dimension, as will be demonstrated next.

2.4 Codimension-one bifurcations

According to the previous introduction, it can be obviously expected that the "minimized" system where codimension-one local bifurcations occur is of dimension one or two, with only one parameter. These bifurcations are the fold bifurcation and the Hopf bifurcation. In this section, we introduce these bifurcations using their normal forms with a minimum possible dimension.

We also provide the formulas by Kuznetsov [47] for computing the critical coefficients of the restriction of a generic n-dimensional system at these bifurcations to the center manifold. For this we assume without loss of generality that the equilibrium at the bifurcation point is $\boldsymbol{x} = \mathbf{0}$, and write the n-dimensional system (2.1) in the form

$$\dot{\boldsymbol{x}} = \boldsymbol{f}(\boldsymbol{x}) = \boldsymbol{f}_1(\boldsymbol{x}) + \boldsymbol{f}_2(\boldsymbol{x}, \boldsymbol{x}) + \boldsymbol{f}_3(\boldsymbol{x}, \boldsymbol{x}, \boldsymbol{x}) + \dots, \tag{2.11}$$

where $\boldsymbol{f}_1(\boldsymbol{x})$ is the linearization $\mathbf{J}\boldsymbol{x}$ ($\mathbf{J}$ being the critical Jacobian matrix), and $\boldsymbol{f}_2$, $\boldsymbol{f}_3$ are the critical multilinear functions defined as

$$\boldsymbol{f}_2(\boldsymbol{x}, \boldsymbol{y}) = \frac{1}{2} \sum_{i,j=1}^{n} \left. \frac{\partial^2 \boldsymbol{f}(\boldsymbol{\theta})}{\partial \theta_i \partial \theta_j} \right|_{\boldsymbol{\theta}=\mathbf{0}} x_i y_j, \qquad \boldsymbol{f}_3(\boldsymbol{x}, \boldsymbol{y}, \boldsymbol{z}) = \frac{1}{6} \sum_{i,j,l=1}^{n} \left. \frac{\partial^3 \boldsymbol{f}(\boldsymbol{\theta})}{\partial \theta_i \partial \theta_j \partial \theta_l} \right|_{\boldsymbol{\theta}=\mathbf{0}} x_i y_j z_l.$$

Obviously, when all the arguments are the same, the multilinear functions simply return the corresponding terms in the Taylor series expansion of the function $\boldsymbol{f}$.

Fold bifurcation

The bifurcation that corresponds to exactly one zero eigenvalue of the linearization of some continuous-time system is called a fold bifurcation. It is also referred to as a limiting point or turning point; it includes some subtypes as well, such as saddle-node, transcritical and pitchfork bifurcations. A normal form of the saddle-node bifurcation is

$$\dot{x} = \beta + x^2 + O(x^3), \tag{2.12}$$

where the $O(x^3)$ terms can be abandoned and the truncated normal form remains locally topologically equivalent. The bifurcation occurs at $\beta = 0$, where $x = 0$ is an equilibrium; for $\beta > 0$, no equilibrium exists locally; for $\beta < 0$, there are a pair of equilibria $x = x_\pm$ locally, with $x_+ > 0$ unstable and $x_- < 0$ stable. A bifurcation diagram showing this is given in Fig. 2.1(a).

A normal form of the transcritical bifurcation is

$$\dot{x} = \beta x + x^2 + O(x^3), \tag{2.13}$$

where the $O(x^3)$ terms can be abandoned and the truncated normal form remains locally topologically equivalent. The bifurcation occurs at $\beta = 0$, where $x = 0$ is an equilibrium; for $\beta > 0$, there are a pair of equilibria, $x = 0$ unstable and $x = x_- < 0$ stable; for $\beta < 0$,

there are a pair of equilibria as well, $x = 0$ stable and $x = x_+ > 0$ unstable. A bifurcation diagram showing this is in Fig. 2.1(b).

The normal form of a pitchfork bifurcation is

$$\dot{x} = \beta x \pm x^3 + O(x^4), \tag{2.14}$$

where the $O(x^4)$ terms can be abandoned and the truncated normal form remains locally topologically equivalent. The bifurcation occurs at $\beta = 0$, and can be categorized as two subtypes. When the term x^3 has coefficient -1, the system has a stable equilibrium $x = 0$ for $\beta \leqslant 0$, which becomes unstable with a pair of stable equilibria $x = x_\pm$ appearing on both sides of $x = 0$ for $\beta > 0$; this is called a supercritical pitchfork bifurcation. When the term x^3 has coefficient $+1$, the equilibrium $x = 0$ is unstable for $\beta \geqslant 0$, and becomes stable with a pair of unstable equilibria $x = x_\pm$ on both sides of $x = 0$ for $\beta < 0$; this is called a subcritical pitchfork bifurcation. The bifurcation diagrams for them are given in Figs. 2.1(c) and (d).

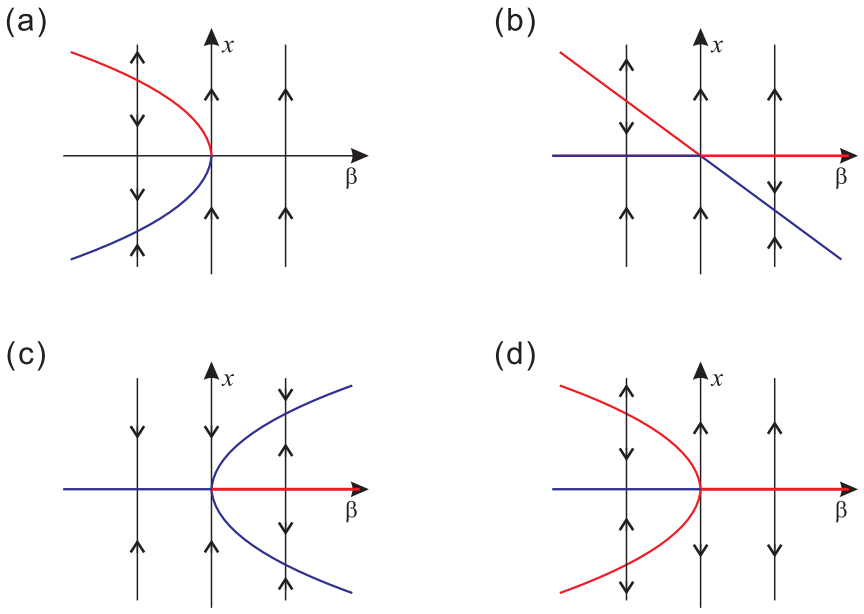

Figure 2.1: Bifurcation diagrams for the fold bifurcation, with blue and red curves indicating stable and unstable equilibria, respectively. (a) saddle-node bifurcation; (b) transcritical bifurcation; (c) supercritical pitchfork bifurcation; (d) subcritical pitchfork bifurcation.

For the n-dimensional system (2.11) at the fold bifurcation (hence $\mathbf{J}$ has a simple zero eigenvalue), we can find the eigenvectors $\boldsymbol{e}_1, \boldsymbol{e}_2 \in \mathbb{R}^n$ for $\mathbf{J}$ and $\mathbf{J}^\top$ such that

$$\mathbf{J}\boldsymbol{e}_1 = \mathbf{0}, \quad \mathbf{J}^\top \boldsymbol{e}_2 = \mathbf{0}, \quad \text{and } \langle \boldsymbol{e}_1, \boldsymbol{e}_2 \rangle = 1,$$

where $\langle \cdot, \cdot \rangle$ denotes inner product in $\mathbb{R}^n$. Then, in the restriction of the system (2.11) to the center manifold, $\dot{u} = bu^2 + cu^3 + O(u^4)$, the coefficients b and c are then given by [47]

$$\begin{aligned} b &= \langle \boldsymbol{e}_2, \boldsymbol{f}_2(\boldsymbol{e}_1, \boldsymbol{e}_1) \rangle, \\ c &= \langle \boldsymbol{e}_2, \boldsymbol{f}_3(\boldsymbol{e}_1, \boldsymbol{e}_1, \boldsymbol{e}_1) \rangle - 4\langle \boldsymbol{e}_2, \boldsymbol{f}_2(\boldsymbol{e}_1, \boldsymbol{f}_2(\boldsymbol{e}_1, \boldsymbol{\theta})) \rangle, \end{aligned} \tag{2.15}$$

where $\boldsymbol{\theta}$ is determined by the bordered system

$$\begin{bmatrix} \mathbf{J} & \boldsymbol{e}_1 \\ \boldsymbol{e}_2 & 0 \end{bmatrix} \begin{bmatrix} \boldsymbol{\theta} \\ \phi \end{bmatrix} = \begin{bmatrix} \boldsymbol{f}_2(\boldsymbol{e}_1, \boldsymbol{e}_1) - \langle \boldsymbol{e}_2, \boldsymbol{f}_2(\boldsymbol{e}_1, \boldsymbol{e}_1) \rangle \boldsymbol{e}_1 \\ 0 \end{bmatrix}.$$

Hopf bifurcation

The bifurcation corresponding to exactly one pair of purely imaginary eigenvalues $\lambda_{1,2} = \pm \mathrm{i}\omega_0$ ($\omega_0 > 0$) of the linearization of a continuous-time system is called a Hopf bifurcation, or Andronov–Hopf bifurcation. The normal form of the Hopf bifurcation is given by

$$\begin{bmatrix} \dot{x}_1 \\ \dot{x}_2 \end{bmatrix} = \begin{bmatrix} \beta & -1 \\ 1 & \beta \end{bmatrix} \begin{bmatrix} x_1 \\ x_2 \end{bmatrix} \pm (x_1^2 + x_2^2) \begin{bmatrix} x_1 \\ x_2 \end{bmatrix} + O(\|\boldsymbol{x}\|^4), \tag{2.16}$$

where the $O(\|\boldsymbol{x}\|^4)$ terms can be abandoned and the truncated normal form remains locally topologically equivalent. Alternatively, letting $z = x_1 + \mathrm{i}x_2$ ($\mathrm{i} = \sqrt{-1}$), the normal form above is expressed in a complex-valued form as

$$\dot{z} = (\beta + \mathrm{i})z \pm z|z|^2 + O(|z|^4), \tag{2.17}$$

where $z \in \mathbb{C}$, $|\cdot|$ denotes the modulus, and abandoning the $O(|z|^4)$ terms does not ruin the locally topological equivalence. The bifurcation occurs at $\beta = 0$, when eigenvalues $\beta \pm \mathrm{i}$ of the linearization about the origin become purely imaginary; the sign of the term $z|z|^2$ determines the subtype. When it is negative, the origin is a stable equilibrium for $\beta \leqslant 0$, and it becomes unstable with a stable limit cycle bifurcating from it for $\beta > 0$; this is called a supercritical Hopf bifurcation. On the contrary, when the sign is positive, the origin is unstable for $\beta \geqslant 0$, and it becomes stable but with an unstable limit cycle bifurcating from it, for $\beta < 0$; this is called a subcritical Hopf bifurcation. Note that at $\beta = 0$, the origin is *nonlinearly* stable or unstable, meaning that the convergence to it or divergence from it is slower than the linearly stable or unstable situation. The scenario of the supercritical Hopf bifurcation of Eq. (2.16) or (2.17) is illustrated in Fig. 2.2.

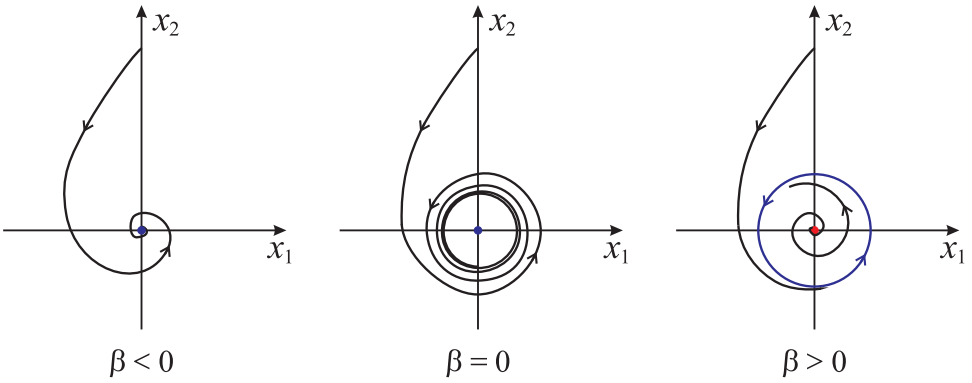

Figure 2.2: Schematic showing the supercritical Hopf bifurcation of system (2.16). Blue and red dots denote stable and unstable equilibria; the stable limit cycle is also in blue.

For the n-dimensional system (2.11) at the Hopf bifurcation (hence $\mathbf{J}$ has eigenvalues $\pm\mathrm{i}\omega_0$), we can find the eigenvectors $\boldsymbol{e}_1, \boldsymbol{e}_2 \in \mathbb{C}^n$ for $\mathbf{J}$ and $\mathbf{J}^\top$ such that

$$\mathbf{J}\boldsymbol{e}_1 = +\mathrm{i}\omega_0\boldsymbol{e}_1, \quad \mathbf{J}^\top\boldsymbol{e}_2 = -\mathrm{i}\omega_0\boldsymbol{e}_2, \quad \text{and } \langle \boldsymbol{e}_1, \boldsymbol{e}_2\rangle = 1.$$

The restricted critical system on the center manifold can have the complex-valued form

$$\dot{u} = l_1(0)u|u|^2 + O(|u|^4),$$

where $l_1(0)$ is called the (critical) first Lyapunov coefficient, whose sign accords with the sign of the degree-three terms in Eqs. (2.16) and (2.17). We can compute it by the formula [47]

$$\begin{aligned} l_1(0) = \frac{1}{2\omega_0}\,\mathrm{Re}\,\big\{ & 6\langle \boldsymbol{e}_2, \boldsymbol{f}_3(\boldsymbol{e}_1, \boldsymbol{e}_1, \overline{\boldsymbol{e}_1})\rangle - 8\langle \boldsymbol{e}_2, \boldsymbol{f}_2\left(\boldsymbol{e}_1, \mathbf{J}^{-1}\boldsymbol{f}_2(\boldsymbol{e}_1, \overline{\boldsymbol{e}_1})\right)\rangle \\ & +4\langle \boldsymbol{e}_2, \boldsymbol{f}_2\left(\overline{\boldsymbol{e}_1}, (2\mathrm{i}\omega_0\mathbf{I} - \mathbf{J}(S_0))^{-1}\boldsymbol{f}_2(\boldsymbol{e}_1, \boldsymbol{e}_1)\right)\rangle\big\}, \end{aligned} \tag{2.18}$$

where $\bar{\cdot}$ denotes complex conjugate. The Hopf bifurcation is supercritical if $l_1(0) < 0$, and it is subcritical if $l_1(0) > 0$.

Finally, let us consider the case of m parameters instead of only one. In the $(n+m)$-dimensional state-parameter space, the locus of a fold or Hopf bifurcation is determined by an equilibrium condition (which is an n-dimensional vector equation) and a bifurcation condition (a scalar equation describing the zero eigenvalue or the zero real parts of eigenvalues). Thus the bifurcation locus (boundary) in the parameter space is generally $(m-1)$-dimensional, that is, curves on a plane, curved surfaces in a parameter space $\mathbb{R}^3$, and the like. Hence, these are the only two types of codimension-one local bifurcations of equilibria.

2.5 Codimension-two bifurcations

When tracking codimension-one bifurcations, two kinds of singularity events may happen: the real parts of additional eigenvalues vanish, or some critical coefficients of the restriction vanish. Both can indicate some unexpected topological behavior for people to "unfold". Since such an event adds one more condition in the state-parameter space, the resultant bifurcation boundary is generally $(m-2)$-dimensional (that is, points on a plane and the like), and we need at least two parameters to unfold it. In this section, we briefly introduce such codimension-two bifurcations; we may realize that there are five kinds of them.

Cusp bifurcation

The cusp bifurcation occurs when the quadratic term coefficient vanishes in a fold bifurcation; in another word, it arises as a consequence of unfolding a degenerate fold bifurcation. The cusp bifurcation occurs in a minimum setting of one-dimensional, two-parameterized systems, and its normal form is given by

$$\dot{x} = \beta_1 + \beta_2 x + \sigma x^3 + O(x^4), \tag{2.19}$$

where $\sigma = \pm 1$, and the truncated normal form (after abandoning the $O(x^4)$ terms) is a topological normal form. When $\sigma = -1$, the bifurcation diagram for the truncated normal form in the $\beta_1\beta_2$-plane comprises the origin as the cusp bifurcation point, and two branches of semi-cubic parabola

$$SN = \left\{(\beta_1, \beta_2) \,\middle|\, \beta_1^2 = \tfrac{4}{27}\beta_2^3,\ \beta_2 > 0\right\},$$

as shown in Fig. 2.3. Here, SN stands for the curve of the saddle-node bifurcation. In the region between the two SN branches, there are three equilibria, $x = 0$ being unstable, and $x = x_\pm$ on both sides being stable; in the other regions (excluding the curve SN and cusp point), $x = 0$ is the unique equilibrium and is stable. These two portraits transform to each other via a saddle-node bifurcation across the curve SN, or via a supercritical pitchfork bifurcation through the cusp point. As the normal form (2.19) remains invariant under $(t, \beta_1, \beta_2) \to (-t, -\beta_1, -\beta_2)$, the bifurcation diagram for $\sigma = +1$ and the current one for $\sigma = -1$ are symmetric about the origin, with the stability of all equilibria and the type of the pitchfork bifurcation changed. For a generic n-dimensional system (2.11) at the cusp bifurcation, the subtype is determined by the sign of the cubic term coefficient c in its restriction, which can be computed according to Eq. (2.15).

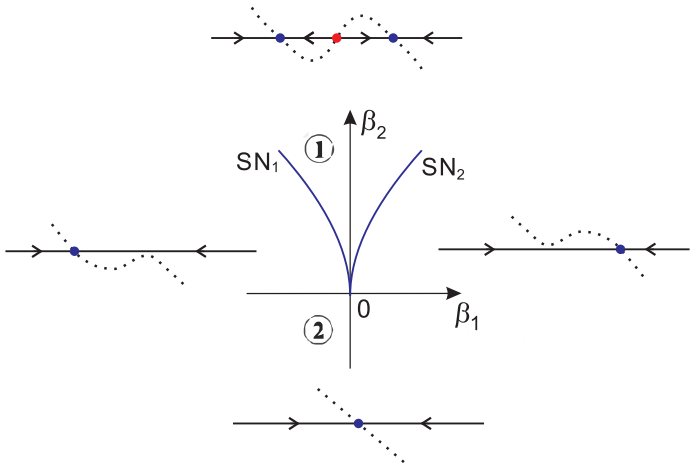

Figure 2.3: Bifurcation diagram for the cusp bifurcation when $\sigma = -1$, with blue and red dots indicating stable and unstable equilibria, respectively.

Bautin bifurcation

The Bautin bifurcation occurs when the first Lyapunov coefficient $l_1(0)$ vanishes in a Hopf bifurcation; in another word, it is a result of unfolding a degenerate Hopf bifurcation. The Bautin bifurcation occurs in a minimum setting of two-dimensional, two-parameterized systems, and its normal form in a complex form is given by

$$\dot{z} = (\beta_1 + \mathrm{i})z + \beta_2 z|z|^2 + \sigma z|z|^4 + O(|z|^6), \tag{2.20}$$

where $\sigma = \pm 1$, and the truncated normal form after abandoning the $O(|z|^6)$ terms is a topological normal form. When $\sigma = -1$, the bifurcation diagram for the truncated normal form in the $\beta_1\beta_2$-plane is composed of the origin as the Bautin bifurcation point and the following bifurcation curves:

(a) $H^- = \{(\beta_1, \beta_2) \,|\, \beta_1 = 0, \beta_2 < 0\}$;

(b) $H^+ = \{(\beta_1, \beta_2) \,|\, \beta_1 = 0, \beta_2 > 0\}$;

(c) $SNL = \{(\beta_1, \beta_2) \,|\, \beta_1 = -\frac{1}{4}\beta_2^2, \beta_2 > 0\}$,

where H^- and H^+ denote supercritical and subcritical Hopf bifurcations, respectively, and SNL stands for the saddle-node bifurcation of limit cycles. As shown in Fig. 2.4, the three curves divide the plane into three regions. Going across the curve H^- from region ① to ②, the stable equilibrium becomes unstable and a stable limit cycle emerges; entering the region ③ across the curve H^+, the equilibrium changes stability again and an unstable limit cycle bifurcates; the two limit cycles with opposite stability collide and annihilate via a saddle-node bifurcation (of limit cycles) on the curve SNL. As the normal form (2.20) remains invariant under $(z, \beta_1, \beta_2, t) \to (\overline{z}, -\beta_1, -\beta_2, -t)$, the bifurcation diagram in the case of $\sigma = +1$ is the reflection of the current one about the origin, with the stability of all limit sets and the types of the Hopf bifurcations changed accordingly.

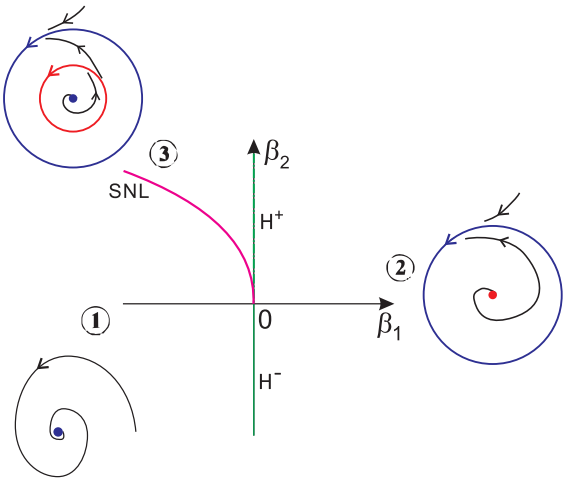

Figure 2.4: Bifurcation diagram for the Bautin bifurcation when $\sigma = -1$, with blue and red indicating stable and unstable equilibria (and limit cycles), respectively. This diagram is a simplified one of Fig. 8.7 in [47] after omitting the phase portraits on the bifurcation boundaries since they can be easily inferred.

Fold–Hopf bifurcation

As its name implies, the fold–Hopf bifurcation of an equilibrium occurs when the linearization has exactly one zero eigenvalue and one pair of non-zero imaginary eigenvalues; in another word, it is a result of the interaction of the fold (say, the saddle-node) and Hopf bifurcations. This type of bifurcation occurs in a minimum setting of three-dimensional,

two-parameterized systems, and its normal form is given in real cylindrical coordinates (ρ, φ, z) by

$$\begin{aligned}
\dot{z} &= \beta_1 + z^2 + \sigma\rho^2 + O\left((z^2+\rho^2)^2\right), \\
\dot{\rho} &= \rho\left[\beta_2 + \theta_1(\beta_1,\beta_2)z + z^2\right] + O\left((z^2+\rho^2)^2\right), \\
\dot{\varphi} &= \omega + \theta_2(\beta_1,\beta_2)z + O\left(z^2+\rho^2\right),
\end{aligned} \tag{2.21}$$

where $\sigma = \pm 1$. The $O(\cdot)$ terms do affect the phase portrait, and the complete bifurcation scenario is unclear yet. The simplified issue of the behavior of the truncated normal form locally for small $|z|$ is expressed by the truncated amplitude system

$$\begin{aligned}
\dot{z} &= \beta_1 + z^2 + \sigma\rho^2, \\
\dot{\rho} &= \rho\left[\beta_2 + \theta_1(\beta_1,\beta_2)z + z^2\right].
\end{aligned} \tag{2.22}$$

The analysis of the system (2.22) provided that $\theta_1(0,0) \neq 0$ yields four subcases. When $\sigma = +1$ and $\theta_1(0,0) > 0$, the codimension-two bifurcation involves the saddle-node and subcritical Hopf bifurcations; when $\sigma = -1$ and $\theta_1(0,0) < 0$, it involves the saddle-node and supercritical Hopf bifurcations. When $\sigma\theta_1(0,0) < 0$, both sub- and supercritical Hopf bifurcations are involved, as well as a Neimark–Sacker bifurcation of limit cycles (or called secondary Hopf bifurcation) that gives birth to a two-dimensional invariant torus. This torus vanishes via some rotating heteroclinic orbit when $\sigma = +1$, $\theta_1(0,0) < 0$, or vanishes via some "blow-up" when $\sigma = -1$, $\theta_1(0,0) > 0$.

Hopf–Hopf bifurcation

The Hopf–Hopf bifurcation occurs when the linearization about an equilibrium has exactly two pairs of imaginary eigenvalues with different norms, indicating the interaction of two Hopf bifurcations. It occurs in a minimum setting of four-dimensional, two-parameterized systems, and its normal form is given in double polar coordinates $(\rho_1, \varphi_1, \rho_2, \varphi_2)$ by

$$\begin{aligned}
\dot{\rho}_1 &= \rho_1\left[\beta_1 + a_{11}(\boldsymbol{\beta})\rho_1^2 + a_{12}(\boldsymbol{\beta})\rho_2^2 + b_1(\boldsymbol{\beta})\rho_2^4\right] + O\left((\rho_1^2+\rho_2^2)^3\right), \\
\dot{\rho}_2 &= \rho_2\left[\beta_2 + a_{21}(\boldsymbol{\beta})\rho_1^2 + a_{22}(\boldsymbol{\beta})\rho_2^2 + b_2(\boldsymbol{\beta})\rho_1^4\right] + O\left((\rho_1^2+\rho_2^2)^3\right), \\
\dot{\varphi}_1 &= \omega_1(\boldsymbol{\beta}) + o(1), \\
\dot{\varphi}_2 &= \omega_2(\boldsymbol{\beta}) + o(1),
\end{aligned} \tag{2.23}$$

where $\boldsymbol{\beta} = [\beta_1 \quad \beta_2]^\top \in \mathbb{R}^2$. Again, the $O(\cdot)$ terms do affect the phase portrait, and the complete bifurcation scenario is unclear yet. Nevertheless, the essential behavior of the full system (2.23) may be approximated by the truncated normal form, which is further described near $\boldsymbol{\beta} = \mathbf{0}$ by the truncated amplitude system

$$\begin{aligned}
\dot{r}_1 &= 2r_1\left[\beta_1 + a_{11}(\boldsymbol{\beta})r_1 + a_{12}(\boldsymbol{\beta})r_2 + b_1(\boldsymbol{\beta})r_2^2\right], \\
\dot{r}_2 &= 2r_2\left[\beta_2 + a_{21}(\boldsymbol{\beta})r_1 + a_{22}(\boldsymbol{\beta})r_2 + b_2(\boldsymbol{\beta})r_1^2\right],
\end{aligned} \tag{2.24}$$

where $r_1 = \rho_1^2$ and $r_2 = \rho_2^2$. The analysis of the system (2.24) indicates two large groups of behavior. The case $a_{11}(\mathbf{0})a_{22}(\mathbf{0}) > 0$ involves Hopf bifurcations (yielding limit cycles)

and the Neimark–Sacker bifurcation (yielding a two-dimensional invariant torus); the case $a_{11}(\mathbf{0})a_{22}(\mathbf{0}) < 0$ involves the bifurcation of a three-dimensional invariant torus out of a two-dimensional one, as well as the blow-up and heteroclinic destruction of the three-dimensional torus. Each case contains a number of subcases, which we do not elucidate here.

Bogdanov–Takens (BT) bifurcation

The Bogdanov–Takens bifurcation (also called double-zero bifurcation), occurs when the linearization about an equilibrium has a non-semisimple double-zero eigenvalue. It occurs in a minimum setting of two-dimensional, two-parameterized systems, and it is the bifurcation that we will mainly deal with later in this thesis. Here, we only give its definition; a detailed introduction of the derivation of its normal form in two-dimensional systems is provided separately in the next section, which will be further used and generalized in Chapter 3.

2.6 Bogdanov–Takens bifurcations

In this section we present relatively detailed fundamentals on codimension-two BT bifurcations. We elucidate the derivation of their normal forms and demonstrate corresponding bifurcation diagrams, with minimum dimensions $n = 2$ and $m = 2$. These results will be necessary in the process of generalizing them to n-dimensional systems in Chapter 3. We consider the following nonlinear planar system:

$$\dot{\boldsymbol{x}} = \boldsymbol{f}(\boldsymbol{x}, \boldsymbol{\alpha}), \quad \boldsymbol{x} \in \mathbb{R}^2,\ \boldsymbol{\alpha} \in \mathbb{R}^2, \tag{2.25}$$

where $\boldsymbol{f}$ is sufficiently smooth in $(\boldsymbol{x}, \boldsymbol{\alpha})$. For the equilibrium and bifurcation conditions, we assume that system (2.25) has an equilibrium $(\boldsymbol{x}_0, \boldsymbol{\alpha}_0)$, $\boldsymbol{f}(\boldsymbol{x}_0, \boldsymbol{\alpha}_0) = \mathbf{0}$, where the Jacobian matrix $\frac{\partial \boldsymbol{f}}{\partial \boldsymbol{x}}\big|_{(\boldsymbol{x}_0, \boldsymbol{\alpha}_0)}$ has a non-semisimple double-zero eigenvalue. Actually, the equilibrium and bifurcation point $(\boldsymbol{x}_0, \boldsymbol{\alpha}_0)$ can be shifted to $(\mathbf{0}, \mathbf{0})$; then, a linear (similarity) transformation that transforms the critical Jacobian matrix to a 2×2 Jordan block brings (2.25) to the following system:

$$\begin{cases} \dot{y}_1 = y_2 + \displaystyle\sum_{0 \leqslant i+j \leqslant d_s} a_{ij}(\boldsymbol{\alpha}) y_1^i y_2^j + O(\|\boldsymbol{y}\|^{d_s+1}), \\ \dot{y}_2 = \displaystyle\sum_{0 \leqslant i+j \leqslant d_s} b_{ij}(\boldsymbol{\alpha}) y_1^i y_2^j + O(\|\boldsymbol{y}\|^{d_s+1}), \end{cases} \tag{2.26}$$

where $a_{ij}(\boldsymbol{\alpha})$, $b_{ij}(\boldsymbol{\alpha}) : \mathbb{R}^2 \to \mathbb{R}$ are smooth functions satisfying $a_{00}(\mathbf{0}) = a_{10}(\mathbf{0}) = a_{01}(\mathbf{0}) = b_{00}(\mathbf{0}) = b_{10}(\mathbf{0}) = b_{01}(\mathbf{0}) = 0$, and d_s is a sufficiently high degree for the state variables with $d_s \geqslant 2$. We continue to use locally smooth invertible transformations, to transform (2.26) into certain topological normal forms. Three cases will be presented.

2.6.1 Saddle-node case

We now introduce variables w_1 and w_2 to denote y_1 and $\dot{y}_1$ in (2.26), respectively, i.e., the parameter-dependent transformation

$$\begin{cases} w_1 = y_1, \\ w_2 = y_2 + \sum\limits_{0 \leqslant i+j \leqslant d_s} a_{ij}(\boldsymbol{\alpha}) y_1^i y_2^j + O(\|\boldsymbol{y}\|^{d_s+1}), \end{cases} \tag{2.27}$$

where the $O(\|\boldsymbol{y}\|^{d_s+1})$ term is the same as that of the first equation in (2.26). The transformation (2.27) is near-identical and smooth in $(\boldsymbol{y}, \boldsymbol{\alpha})$ in a neighborhood of $(\mathbf{0}, \mathbf{0})$; moreover, it is invertible in a neighborhood of $(\mathbf{0}, \mathbf{0})$ by the inverse function theorem, as its Jacobian determinant at $\boldsymbol{y} = \mathbf{0}$ equals $1 + a_{01}(\boldsymbol{\alpha})$. The system (2.26) is then changed to

$$\begin{cases} \dot{w}_1 = w_2, \\ \dot{w}_2 = \sum\limits_{0 \leqslant i+j \leqslant 2} h_{ij}(\boldsymbol{\alpha}) w_1^i w_2^j + O(\|\boldsymbol{w}\|^3), \end{cases} \tag{2.28}$$

where $h_{ij}(\boldsymbol{\alpha}) : \mathbb{R}^2 \to \mathbb{R}$ are smooth functions. After tedious calculations, we can find that

$$\begin{aligned} h_{00}(\boldsymbol{\alpha}) &= b_{00}(\boldsymbol{\alpha}) + O(\|\boldsymbol{\alpha}\|^2), \\ h_{10}(\boldsymbol{\alpha}) &= b_{10}(\boldsymbol{\alpha}) + a_{11}(\boldsymbol{\alpha}) b_{00}(\boldsymbol{\alpha}) - b_{11}(\boldsymbol{\alpha}) a_{00}(\boldsymbol{\alpha}) + O(\|\boldsymbol{\alpha}\|^2), \\ h_{01}(\boldsymbol{\alpha}) &= b_{01}(\boldsymbol{\alpha}) + a_{10}(\boldsymbol{\alpha}) + 2a_{02}(\boldsymbol{\alpha}) b_{00}(\boldsymbol{\alpha}) - [2b_{02}(\boldsymbol{\alpha}) + a_{11}(\boldsymbol{\alpha})] a_{00}(\boldsymbol{\alpha}) + O(\|\boldsymbol{\alpha}\|^2), \\ h_{20}(\boldsymbol{\alpha}) &= b_{20}(\boldsymbol{\alpha}) - a_{20}(\boldsymbol{\alpha}) b_{01}(\boldsymbol{\alpha}) + a_{11}(\boldsymbol{\alpha}) b_{10}(\boldsymbol{\alpha}) - 2a_{20}(\boldsymbol{\alpha}) a_{02}(\boldsymbol{\alpha}) b_{00}(\boldsymbol{\alpha}) + O(\|\boldsymbol{\alpha}\|), \\ h_{11}(\boldsymbol{\alpha}) &= b_{11}(\boldsymbol{\alpha}) + 2a_{20}(\boldsymbol{\alpha}) + 2a_{02}(\boldsymbol{\alpha}) b_{10}(\boldsymbol{\alpha}) - 2a_{11}(\boldsymbol{\alpha}) a_{02}(\boldsymbol{\alpha}) b_{00}(\boldsymbol{\alpha}) + O(\|\boldsymbol{\alpha}\|), \\ h_{02}(\boldsymbol{\alpha}) &= b_{02}(\boldsymbol{\alpha}) + a_{11}(\boldsymbol{\alpha}) + a_{02}(\boldsymbol{\alpha}) b_{01}(\boldsymbol{\alpha}) - 2a_{02}(\boldsymbol{\alpha})^2 b_{00}(\boldsymbol{\alpha}) + O(\|\boldsymbol{\alpha}\|), \end{aligned} \tag{2.29}$$

where the $O(\|\boldsymbol{\alpha}\|)$ and $O(\|\boldsymbol{\alpha}\|^2)$ terms in (2.29) that are not explicitly given all contain a factor $a_{00}(\boldsymbol{\alpha})$, $a_{10}(\boldsymbol{\alpha})$, or $a_{01}(\boldsymbol{\alpha})$; we write Eq. (2.29) in its present form for the evaluation of $h_{ij}(\mathbf{0})$ $(i + j = 2)$ and $h'_{ij}(\mathbf{0})$ $(i + j \leqslant 1$ and the prime denotes partial derivatives with respect to α_1 and $\alpha_2)$, as well as for a secondary transformation to be carried out later. It is clear that $h_{00}(\mathbf{0}) = h_{10}(\mathbf{0}) = h_{01}(\mathbf{0}) = 0$, $h_{20}(\mathbf{0}) = b_{20}(\mathbf{0})$, $h_{11}(\mathbf{0}) = b_{11}(\mathbf{0}) + 2a_{20}(\mathbf{0})$, and $h_{02}(\mathbf{0}) = b_{02}(\mathbf{0}) + a_{11}(\mathbf{0})$.

We then eliminate one of the linear terms in the equation for $\dot{w}_2$ in Eq. (2.28) for all parameter values. This can be done for the w_1 term or w_2 term, by shifting the coordinate w_1, if $h_{20}(\mathbf{0}) \neq 0$ or $h_{11}(\mathbf{0}) \neq 0$, respectively; here, we make the latter choice. We let

$$\begin{cases} v_1 = w_1 - \delta(\boldsymbol{\alpha}), \\ v_2 = w_2, \end{cases} \tag{2.30}$$

which changes the system (2.28) into

$$\begin{cases} \dot{v}_1 = v_2, \\ \dot{v}_2 = \big\{h_{00} + h_{10}\delta + h_{20}\delta^2 + O(\delta^2)\big\} \\ \qquad + \big\{h_{10} + 2h_{20}\delta + O(\delta^2)\big\} v_1 + \big\{h_{01} + h_{11}\delta + O(\delta^2)\big\} v_2 \\ \qquad + \{h_{20} + O(\delta)\} v_1^2 + \{h_{11} + O(\delta)\} v_1 v_2 + \{h_{02} + O(\delta)\} v_2^2 + O(\|\boldsymbol{v}\|^3). \end{cases} \tag{2.31}$$

If $h_{11}(\mathbf{0}) \neq 0$, then the implicit function theorem indicates the existence of some smooth $\delta(\boldsymbol{\alpha})$ in a neighborhood of $\boldsymbol{\alpha} = \mathbf{0}$ such that $h_{01} + h_{11}\delta + O(\delta^2) \equiv 0$; in this case, we have

$$\delta(\boldsymbol{\alpha}) = -\frac{1}{h_{11}(\mathbf{0})} h_{01}(\boldsymbol{\alpha}) + O(\|\boldsymbol{\alpha}\|^2).$$

Accordingly, the system (2.31) is specified as

$$\begin{cases} \dot{v}_1 = v_2, \\ \dot{v}_2 = g_{00}(\boldsymbol{\alpha}) + g_{10}(\boldsymbol{\alpha}) v_1 + g_{20}(\boldsymbol{\alpha}) v_1^2 + g_{11}(\boldsymbol{\alpha}) v_1 v_2 + g_{02}(\boldsymbol{\alpha}) v_2^2 + O(\|\boldsymbol{v}\|^3), \end{cases} \tag{2.32}$$

where $g_{ij}(\boldsymbol{\alpha}) : \mathbb{R}^2 \to \mathbb{R}$ are smooth functions satisfying

$$\begin{aligned} g_{00}(\boldsymbol{\alpha}) &= h_{00}(\boldsymbol{\alpha}) - \frac{1}{h_{11}(\mathbf{0})} h_{10}(\boldsymbol{\alpha}) h_{01}(\boldsymbol{\alpha}) + \frac{h_{20}(\mathbf{0})}{h_{11}(\mathbf{0})^2} h_{01}(\boldsymbol{\alpha})^2 + O(\|\boldsymbol{\alpha}\|^3), \\ g_{10}(\boldsymbol{\alpha}) &= h_{10}(\boldsymbol{\alpha}) - \frac{2h_{20}(\mathbf{0})}{h_{11}(\mathbf{0})} h_{01}(\boldsymbol{\alpha}) + O(\|\boldsymbol{\alpha}\|^2), \end{aligned} \tag{2.33}$$

and $g_{20}(\boldsymbol{\alpha}) = h_{20}(\boldsymbol{\alpha}) + O(\|\boldsymbol{\alpha}\|)$, $g_{11}(\boldsymbol{\alpha}) = h_{11}(\boldsymbol{\alpha}) + O(\|\boldsymbol{\alpha}\|)$, and $g_{02}(\boldsymbol{\alpha}) = h_{02}(\boldsymbol{\alpha}) + O(\|\boldsymbol{\alpha}\|)$. It is clear that $g_{00}(\mathbf{0}) = g_{10}(\mathbf{0}) = 0$, $g_{20}(\mathbf{0}) = h_{20}(\mathbf{0})$, $g_{11}(\mathbf{0}) = h_{11}(\mathbf{0})$, and $g_{02}(\mathbf{0}) = h_{02}(\mathbf{0})$.

We then introduce a new time variable by the time reparametrization

$$d\,t_{\text{old}} = [1 + \theta(\boldsymbol{\alpha}) v_1]\, d\,t_{\text{new}}, \tag{2.34}$$

which is time-direction-preserving near $\boldsymbol{v} = \mathbf{0}$, with the smooth function $\theta(\boldsymbol{\alpha})$ to be found. Now the overdot denotes derivative with respect to the new time and we have the following locally orbitally equivalent system:

$$\begin{cases} \dot{v}_1 = v_2 + \theta(\boldsymbol{\alpha}) v_1 v_2, \\ \dot{v}_2 = g_{00}(\boldsymbol{\alpha}) + [g_{10}(\boldsymbol{\alpha}) + g_{00}(\boldsymbol{\alpha})\theta(\boldsymbol{\alpha})]\, v_1 \\ \qquad + [g_{20}(\boldsymbol{\alpha}) + g_{10}(\boldsymbol{\alpha})\theta(\boldsymbol{\alpha})]\, v_1^2 + g_{11}(\boldsymbol{\alpha}) v_1 v_2 + g_{02}(\boldsymbol{\alpha}) v_2^2 + O(\|\boldsymbol{v}\|^3). \end{cases} \tag{2.35}$$

A secondary transformation by which (2.26) is transformed to (2.28) brings (2.35) to

$$\begin{cases} \dot{u}_1 = u_2, \\ \dot{u}_2 = f_{00}(\boldsymbol{\alpha}) + f_{10}(\boldsymbol{\alpha}) u_1 + f_{20}(\boldsymbol{\alpha}) u_1^2 + f_{11}(\boldsymbol{\alpha}) u_1 u_2 + f_{02}(\boldsymbol{\alpha}) u_2^2 + O(\|\boldsymbol{u}\|^3), \end{cases} \tag{2.36}$$

where we can use Eq. (2.29) to obtain

$$\begin{aligned} f_{00}(\boldsymbol{\alpha}) &= g_{00}(\boldsymbol{\alpha}), \\ f_{10}(\boldsymbol{\alpha}) &= g_{10}(\boldsymbol{\alpha}) + 2g_{00}(\boldsymbol{\alpha})\theta(\boldsymbol{\alpha}), \\ f_{20}(\boldsymbol{\alpha}) &= g_{20}(\boldsymbol{\alpha}) + 2g_{10}(\boldsymbol{\alpha})\theta(\boldsymbol{\alpha}) + g_{00}(\boldsymbol{\alpha})\theta(\boldsymbol{\alpha})^2, \\ f_{11}(\boldsymbol{\alpha}) &= g_{11}(\boldsymbol{\alpha}), \\ f_{02}(\boldsymbol{\alpha}) &= g_{02}(\boldsymbol{\alpha}) + \theta(\boldsymbol{\alpha}). \end{aligned} \tag{2.37}$$

Hence, by taking $\theta(\boldsymbol{\alpha}) = -g_{02}(\boldsymbol{\alpha})$, the u_2^2 term is eliminated, yielding the following system:

$$\begin{cases} \dot{u}_1 = u_2, \\ \dot{u}_2 = \mu_1(\boldsymbol{\alpha}) + \mu_2(\boldsymbol{\alpha}) u_1 + a_2(\boldsymbol{\alpha}) u_1^2 + b_2(\boldsymbol{\alpha}) u_1 u_2 + O(\|\boldsymbol{u}\|^3), \end{cases} \tag{2.38}$$

where $a_2 = h_{20}(\mathbf{0}) + O(\|\boldsymbol{\alpha}\|)$, $b_2 = h_{11}(\mathbf{0}) + O(\|\boldsymbol{\alpha}\|)$, and $\boldsymbol{\mu} = (\mu_1, \mu_2)$ with

$$\mu_1 = h_{00} - \frac{1}{h_{11}(\mathbf{0})} h_{10} h_{01} + \frac{h_{20}(\mathbf{0})}{h_{11}(\mathbf{0})^2} h_{01}^2 + O(\|\boldsymbol{\alpha}\|^3), \tag{2.39a}$$

$$\mu_2 = h_{10} - \frac{2h_{20}(\mathbf{0})}{h_{11}(\mathbf{0})} h_{01} - 2h_{02}(\mathbf{0}) h_{00} + O(\|\boldsymbol{\alpha}\|^2). \tag{2.39b}$$

Finally, if $a_2(\mathbf{0}) b_2(\mathbf{0}) \neq 0$, introducing again a new time variable and new state variables z_1, z_2 by the scaling

$$t_{\text{new}} = \left| \frac{a_2}{b_2} \right| t_{\text{old}}, \quad z_1 = \frac{b_2^2}{a_2} u_1, \quad z_2 = \operatorname{sgn}(a_2 b_2) \frac{b_2^3}{a_2^2} u_2, \tag{2.40}$$

we obtain the normal form below,

$$\begin{cases} \dot{z}_1 = z_2, \\ \dot{z}_2 = \beta_1 + \beta_2 z_1 + z_1^2 + \sigma z_1 z_2 + O(\|\boldsymbol{z}\|^3). \end{cases} \tag{2.41}$$

Here, the sign $\sigma = \operatorname{sgn}(a_2(\mathbf{0}) b_2(\mathbf{0}))$ defines the subtype of the bifurcation, and the unfolding parameters $\boldsymbol{\beta}$ are related to the original parameters $\boldsymbol{\alpha}$ by

$$\begin{aligned} \beta_1(\boldsymbol{\alpha}) &= \frac{b_2(\boldsymbol{\alpha})^4}{a_2(\boldsymbol{\alpha})^3} \mu_1(\boldsymbol{\alpha}), \\ \beta_2(\boldsymbol{\alpha}) &= \frac{b_2(\boldsymbol{\alpha})^2}{a_2(\boldsymbol{\alpha})^2} \mu_2(\boldsymbol{\alpha}). \end{aligned} \tag{2.42}$$

It can be proved that the truncated normal form after abandoning the $O(\|\boldsymbol{z}\|^3)$ terms is a topological normal form. When $\sigma = -1$, the bifurcation diagram for (2.41) in the (β_1, β_2)-plane consists of the origin and the following bifurcation curves:

(a) $H_0^- = \{(\beta_1, \beta_2) \,|\, \beta_1 = 0, \beta_2 < 0\}$;

(b) $SN_\ominus = \{(\beta_1, \beta_2) \,|\, \beta_1 = \frac{1}{4}\beta_2^2 + O(\beta_2^3), \beta_2 < 0\}$;

(c) $SN_\oplus = \{(\beta_1, \beta_2) \,|\, \beta_1 = \frac{1}{4}\beta_2^2 + O(\beta_2^3), \beta_2 > 0\}$;

(d) $HO = \{(\beta_1, \beta_2) \,|\, \beta_1 = -\frac{6}{25}\beta_2^2 + o(\beta_2^2), \beta_2 < 0\}$,

where $SN_\ominus$ and $SN_\oplus$ are the two branches of the curve for saddle-node bifurcations on attracting and repelling center manifolds, respectively, H_0^- denotes a supercritical Hopf bifurcation of the zero equilibrium (origin), and HO stands for the homoclinic bifurcation. As illustrated in Fig. 2.5, these four curves divide the $\beta_1\beta_2$-plane into four regions: there are no equilibria in region ① and a pair of saddle and stable node appear after entering region ②; via the Hopf bifurcation on H_0^-, the stable equilibrium becomes unstable and a stable limit cycle emerges in region ③; then, the limit cycle grows and touches the saddle at the homoclinic bifurcation and disappears after entering ④. As Eq. (2.41) is invariant under $(\tau, u_2, \sigma) \to (-\tau, -u_2, -\sigma)$, the bifurcation diagram for $\sigma = +1$ remains the same, except for different types of bifurcation curves owing to the changes in the stability of the related limit sets. All the fundamentals introduced above follow from [47] with a few corrections.

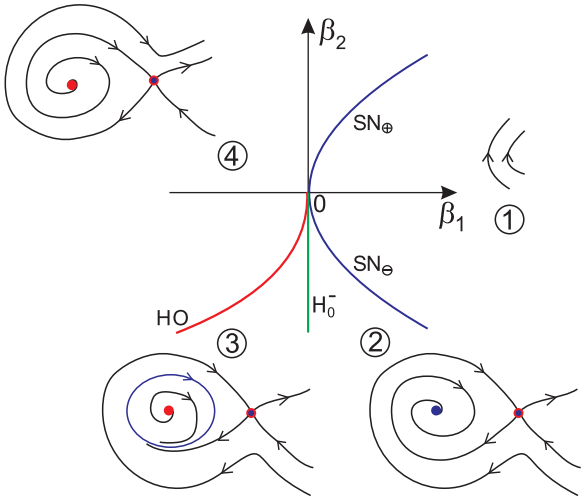

Figure 2.5: Bifurcation diagram for the BT bifurcation of the system (2.41) (the saddle-node case) for $\sigma = -1$. This diagram is a simplified one of that in [47].

2.6.2 Transcritical case

We now present a different unfolding of the BT bifurcation, which, if transformed to the form of (2.41), will not be able to satisfy the transversality condition. In addition to the general hypotheses, we further assume that after appropriate shifts, the origin $\boldsymbol{x} = \boldsymbol{0}$ is an enduring equilibrium under any parameter perturbation around $\boldsymbol{\alpha} = \boldsymbol{0}$. Accordingly, $a_{00}(\boldsymbol{\alpha}) \equiv 0$ and $b_{00}(\boldsymbol{\alpha}) \equiv 0$ in the system (2.26), and the system near $\boldsymbol{y} = \boldsymbol{0}$ is locally topologically equivalent to

$$\begin{cases} \dot{w}_1 = w_2, \\ \dot{w}_2 = \displaystyle\sum_{1 \leqslant i+j \leqslant 2} h_{ij}(\boldsymbol{\alpha}) w_1^i w_2^j + O(\|\boldsymbol{w}\|^3), \end{cases} \tag{2.43}$$

where $h_{ij}(\boldsymbol{\alpha}) : \mathbb{R}^2 \to \mathbb{R}$ are smooth functions given by

$$\begin{aligned} h_{10}(\boldsymbol{\alpha}) &= b_{10}(\boldsymbol{\alpha}) + a_{01}(\boldsymbol{\alpha}) b_{10}(\boldsymbol{\alpha}) - b_{01}(\boldsymbol{\alpha}) a_{10}(\boldsymbol{\alpha}), \\ h_{01}(\boldsymbol{\alpha}) &= b_{01}(\boldsymbol{\alpha}) + a_{10}(\boldsymbol{\alpha}), \\ h_{20}(\boldsymbol{\alpha}) &= b_{20}(\boldsymbol{\alpha}) - a_{20}(\boldsymbol{\alpha}) b_{01}(\boldsymbol{\alpha}) + a_{11}(\boldsymbol{\alpha}) b_{10}(\boldsymbol{\alpha}) + O(\|\boldsymbol{\alpha}\|), \\ h_{11}(\boldsymbol{\alpha}) &= b_{11}(\boldsymbol{\alpha}) + 2a_{20}(\boldsymbol{\alpha}) + 2a_{02}(\boldsymbol{\alpha}) b_{10}(\boldsymbol{\alpha}) + O(\|\boldsymbol{\alpha}\|), \\ h_{02}(\boldsymbol{\alpha}) &= b_{02}(\boldsymbol{\alpha}) + a_{11}(\boldsymbol{\alpha}) + a_{02}(\boldsymbol{\alpha}) b_{01}(\boldsymbol{\alpha}) + O(\|\boldsymbol{\alpha}\|). \end{aligned} \tag{2.44}$$

Here, the $O(\|\boldsymbol{\alpha}\|)$ terms in (2.44) that are not explicitly given all contain a factor $a_{10}(\boldsymbol{\alpha})$ or $a_{01}(\boldsymbol{\alpha})$. Clearly, $h_{10}(\boldsymbol{0}) = h_{01}(\boldsymbol{0}) = 0$, and $h_{20}(\boldsymbol{0}) = b_{20}(\boldsymbol{0})$, $h_{11}(\boldsymbol{0}) = b_{11}(\boldsymbol{0}) + 2a_{20}(\boldsymbol{0})$, and $h_{02}(\boldsymbol{0}) = b_{02}(\boldsymbol{0}) + a_{11}(\boldsymbol{0})$ as in Sec. 2.6.1.

Next, we carry out the time reparametrization as in Eq. (2.34), with which the system is transformed to

$$\begin{cases} \dot{v}_1 = v_2 + \theta(\boldsymbol{\alpha}) v_1 v_2, \\ \dot{v}_2 = h_{10}(\boldsymbol{\alpha}) v_1 + h_{01}(\boldsymbol{\alpha}) v_2 \\ \qquad + \left[h_{20}(\boldsymbol{\alpha}) + h_{10}(\boldsymbol{\alpha}) \theta(\boldsymbol{\alpha}) \right] v_1^2 + \left[h_{11}(\boldsymbol{\alpha}) + h_{01}(\boldsymbol{\alpha}) \theta(\boldsymbol{\alpha}) \right] v_1 v_2 + g_{02}(\boldsymbol{\alpha}) v_2^2 \\ \qquad + O(\|\boldsymbol{v}\|^3). \end{cases} \tag{2.45}$$

A secondary transformation by which (2.26) is transformed to (2.43) brings (2.45) to

$$\begin{cases} \dot{u}_1 = u_2, \\ \dot{u}_2 = f_{10}(\boldsymbol{\alpha})u_1 + f_{01}(\boldsymbol{\alpha})u_2 + f_{20}(\boldsymbol{\alpha})u_1^2 + f_{11}(\boldsymbol{\alpha})u_1u_2 + f_{02}(\boldsymbol{\alpha})u_2^2 + O(\|\boldsymbol{u}\|^3), \end{cases} \tag{2.46}$$

where we can use Eq. (2.44) to obtain

$$\begin{aligned} &f_{10}(\boldsymbol{\alpha}) = h_{10}(\boldsymbol{\alpha}), \quad f_{01}(\boldsymbol{\alpha}) = h_{01}(\boldsymbol{\alpha}), \\ &f_{20}(\boldsymbol{\alpha}) = h_{20}(\boldsymbol{\alpha}) + 2h_{10}(\boldsymbol{\alpha})\theta(\boldsymbol{\alpha}), \\ &f_{11}(\boldsymbol{\alpha}) = h_{11}(\boldsymbol{\alpha}) + h_{01}(\boldsymbol{\alpha})\theta(\boldsymbol{\alpha}), \\ &f_{02}(\boldsymbol{\alpha}) = h_{02}(\boldsymbol{\alpha}) + \theta(\boldsymbol{\alpha}). \end{aligned} \tag{2.47}$$

Hence, by taking $\theta(\boldsymbol{\alpha}) = -h_{02}(\boldsymbol{\alpha})$, the u_2^2 term is eliminated, yielding the following system:

$$\begin{cases} \dot{u}_1 = u_2, \\ \dot{u}_2 = \mu_1(\boldsymbol{\alpha})u_1 + \mu_2(\boldsymbol{\alpha})u_2 + a_2(\boldsymbol{\alpha})u_1^2 + b_2(\boldsymbol{\alpha})u_1u_2 + O(\|\boldsymbol{u}\|^3), \end{cases} \tag{2.48}$$

where $a_2 = h_{20}(\mathbf{0}) + O(\|\boldsymbol{\alpha}\|)$, $b_2 = h_{11}(\mathbf{0}) + O(\|\boldsymbol{\alpha}\|)$, and $\boldsymbol{\mu} = (\mu_1, \mu_2) = (h_{10}, h_{01})$.

Finally, if $a_2(\mathbf{0})b_2(\mathbf{0}) \neq 0$, the same scaling as in Eq. (2.40) brings Eq. (2.48) to the normal form,

$$\begin{cases} \dot{z}_1 = z_2, \\ \dot{z}_2 = \beta_1 z_1 + \beta_2 z_2 + z_1^2 + \sigma z_1 z_2 + O(\|\boldsymbol{z}\|^3). \end{cases} \tag{2.49}$$

Here, the sign $\sigma = \operatorname{sgn}(a_2(\mathbf{0})b_2(\mathbf{0}))$ defines the subtype of the bifurcation, and the unfolding parameters $\boldsymbol{\beta}$ are related to $\boldsymbol{\alpha}$ by

$$\begin{aligned} \beta_1(\boldsymbol{\alpha}) &= \frac{b_2(\boldsymbol{\alpha})^2}{a_2(\boldsymbol{\alpha})^2}\, h_{10}(\boldsymbol{\alpha}), \\ \beta_2(\boldsymbol{\alpha}) &= \left|\frac{b_2(\boldsymbol{\alpha})}{a_2(\boldsymbol{\alpha})}\right| h_{01}(\boldsymbol{\alpha}). \end{aligned} \tag{2.50}$$

Such an unfolding was investigated in [37]; it can also be analyzed by shifting the coordinate z_1 to obtain the normal form in the general case (with a constant but no z_2 term) and then comparing the parameters. Besides, it can be proved that the truncated normal form after abandoning the $O(\|\boldsymbol{z}\|^3)$ terms is a topological normal form. When $\sigma = +1$, the bifurcation diagram for (2.49) in the (β_1, β_2)-plane consists of the origin and the following bifurcation curves:

(a) $T_{\ominus} = \{(\beta_1, \beta_2) \,|\, \beta_1 = 0, \beta_2 < 0\}$;

(b) $T_{\oplus} = \{(\beta_1, \beta_2) \,|\, \beta_1 = 0, \beta_2 > 0\}$;

(c) $H_0^+ = \{(\beta_1, \beta_2) \,|\, \beta_2 = 0, \beta_1 < 0\}$;

(d) $HO_0 = \{(\beta_1, \beta_2) \,|\, \beta_2 = \frac{1}{7}\beta_1 + o(\beta_1), \beta_1 < 0\}$;

(e) $H_{\neq 0}^+ = \{(\beta_1, \beta_2) \,|\, \beta_2 = \beta_1 + O(\beta_1^2), \beta_1 > 0\}$;

(f) $HO_{\neq 0} = \{(\beta_1, \beta_2) \,|\, \beta_2 = \frac{6}{7}\beta_1 + o(\beta_1), \beta_1 > 0\}$,

where $T_\ominus$ and $T_\oplus$ are the two branches of the curve for transcritical bifurcations occurring on attracting and repelling center manifolds; H_0 and $H_{\neq 0}$ denote the Hopf bifurcation of the origin and the nontrivial equilibrium, respectively; HO_0 and $HO_{\neq 0}$ are the curves for homoclinic bifurcations occurring in the limit cycles that arise from H_0^+ and $H_{\neq 0}^+$, respectively. As Eq. (2.49) is invariant under $(\tau, u_2, \beta_2, \sigma) \to (-\tau, -u_2, -\beta_2, -\sigma)$, the bifurcation diagram for $\sigma = -1$ is the reflection of that for $\sigma = +1$ about the β_1-axis, with different types of bifurcation curves owing to the changes in the stability of the related limit sets.

2.6.3 Pitchfork case

Many systems in real-world applications have a $\mathbf{Z}_2$ symmetry and hence an enduring equilibrium, and the BT bifurcation in this case is presented in this subsection. In addition to the general hypotheses, we assume that after appropriate shifts, $\boldsymbol{f}(-\boldsymbol{x}, \boldsymbol{\alpha}) \equiv -\boldsymbol{f}(\boldsymbol{x}, \boldsymbol{\alpha})$ for all $(\boldsymbol{x}, \boldsymbol{\alpha})$ a neighborhood of $(\mathbf{0}, \mathbf{0})$. Accordingly, $a_{ij}(\boldsymbol{\alpha}) \equiv 0$ and $b_{ij}(\boldsymbol{\alpha}) \equiv 0$ for all i, j with $i+j$ an even number in Eq. (2.26), and the system near $\boldsymbol{y} = \mathbf{0}$ is locally topologically equivalent to

$$\begin{cases} \dot{w}_1 = w_2, \\ \dot{w}_2 = \displaystyle\sum_{i+j=1,3} h_{ij}(\boldsymbol{\alpha}) w_1^i w_2^j + O(\|\boldsymbol{w}\|^5), \end{cases} \tag{2.51}$$

where $h_{ij}(\boldsymbol{\alpha}) : \mathbb{R}^2 \to \mathbb{R}$ are smooth functions given by

$$\begin{aligned} h_{10}(\boldsymbol{\alpha}) &= b_{10}(\boldsymbol{\alpha}) + a_{01}(\boldsymbol{\alpha}) b_{10}(\boldsymbol{\alpha}) - b_{01}(\boldsymbol{\alpha}) a_{10}(\boldsymbol{\alpha}), \\ h_{01}(\boldsymbol{\alpha}) &= b_{01}(\boldsymbol{\alpha}) + a_{10}(\boldsymbol{\alpha}), \\ h_{30}(\boldsymbol{\alpha}) &= b_{30}(\boldsymbol{\alpha}) + a_{21}(\boldsymbol{\alpha}) b_{10}(\boldsymbol{\alpha}) + O(\|\boldsymbol{\alpha}\|), \\ h_{21}(\boldsymbol{\alpha}) &= b_{21}(\boldsymbol{\alpha}) + 3a_{30}(\boldsymbol{\alpha}) + 2a_{12}(\boldsymbol{\alpha}) b_{10}(\boldsymbol{\alpha}) + O(\|\boldsymbol{\alpha}\|), \\ h_{12}(\boldsymbol{\alpha}) &= b_{12}(\boldsymbol{\alpha}) + 2a_{21}(\boldsymbol{\alpha}) + a_{12}(\boldsymbol{\alpha}) b_{01}(\boldsymbol{\alpha}) + O(\|\boldsymbol{\alpha}\|), \\ h_{03}(\boldsymbol{\alpha}) &= b_{03}(\boldsymbol{\alpha}) + a_{12}(\boldsymbol{\alpha}) + O(\|\boldsymbol{\alpha}\|). \end{aligned} \tag{2.52}$$

Here the $O(\|\boldsymbol{\alpha}\|)$ terms that are not explicit given represent all terms (i) containing $a_{10}(\boldsymbol{\alpha})$ or $a_{01}(\boldsymbol{\alpha})$, or (ii) containing a product of $a_{30}(\boldsymbol{\alpha})$ or $a_{03}(\boldsymbol{\alpha})$ with $b_{10}(\boldsymbol{\alpha})$ or $b_{01}(\boldsymbol{\alpha})$. These terms are are irrelevant to the evaluation of $h_{ij}(\mathbf{0})$ and unnecessary in a later situation where $a_{10}(\boldsymbol{\alpha}) \equiv a_{01}(\boldsymbol{\alpha}) \equiv a_{30}(\boldsymbol{\alpha}) \equiv a_{03}(\boldsymbol{\alpha}) \equiv 0$. Clearly, $h_{10}(\mathbf{0}) = h_{01}(\mathbf{0}) = 0$.

We then introduce a new time variable by the time reparametrization

$$\mathrm{d}\, t_{\mathrm{old}} = \left[1 + \theta_1(\boldsymbol{\alpha}) v_1^2 + \theta_2(\boldsymbol{\alpha}) v_1 v_2\right] \mathrm{d}\, t_{\mathrm{new}}, \tag{2.53}$$

which preserves the direction of time near $\boldsymbol{v} = \mathbf{0}$ and the $\mathbf{Z}^2$ symmetry, but with the smooth functions $\theta_1(\boldsymbol{\alpha})$ and $\theta_2(\boldsymbol{\alpha})$ to be determined. Now the overdot denotes derivative with respect to the new time and we have the following locally orbitally equivalent system:

$$\begin{cases} \dot{v}_1 = v_2 + \theta_1(\boldsymbol{\alpha}) v_1^2 v_2 + \theta_2(\boldsymbol{\alpha}) v_1 v_2^2, \\ \dot{v}_2 = h_{10}(\boldsymbol{\alpha}) v_1 + h_{01}(\boldsymbol{\alpha}) v_2 \\ \qquad + \left\{h_{30}(\boldsymbol{\alpha}) + h_{10}(\boldsymbol{\alpha}) \theta_1(\boldsymbol{\alpha})\right\} v_1^3 + \left\{h_{21}(\boldsymbol{\alpha}) + h_{01}(\boldsymbol{\alpha}) \theta_1(\boldsymbol{\alpha}) + h_{10}(\boldsymbol{\alpha}) \theta_2(\boldsymbol{\alpha})\right\} v_1^2 v_2 \\ \qquad + \left\{h_{12}(\boldsymbol{\alpha}) + h_{01}(\boldsymbol{\alpha}) \theta_2(\boldsymbol{\alpha})\right\} v_1 v_2^2 + h_{03}(\boldsymbol{\alpha}) v_2^3 + O(\|\boldsymbol{v}\|^5). \end{cases} \tag{2.54}$$

A secondary transformation by which (2.26) is transformed to (2.51) brings (2.54) to

$$\begin{cases} \dot{u}_1 = u_2, \\ \dot{u}_2 = f_{10}(\boldsymbol{\alpha})u_1 + f_{01}(\boldsymbol{\alpha})u_2 + f_{30}(\boldsymbol{\alpha})u_1^3 + f_{21}(\boldsymbol{\alpha})u_1^2u_2 + O(\|\boldsymbol{u}\|^5), \end{cases} \tag{2.55}$$

where we can use Eq. (2.52) to obtain

$$\begin{aligned} &f_{10}(\boldsymbol{\alpha}) = h_{10}(\boldsymbol{\alpha}), \quad f_{01}(\boldsymbol{\alpha}) = h_{01}(\boldsymbol{\alpha}), \\ &f_{30}(\boldsymbol{\alpha}) = h_{30}(\boldsymbol{\alpha}) + 2\theta_1(\boldsymbol{\alpha})h_{10}(\boldsymbol{\alpha}), \\ &f_{21}(\boldsymbol{\alpha}) = h_{21}(\boldsymbol{\alpha}) + \theta_1(\boldsymbol{\alpha})h_{01}(\boldsymbol{\alpha}) + 3\theta_2(\boldsymbol{\alpha})h_{10}(\boldsymbol{\alpha}), \\ &f_{12}(\boldsymbol{\alpha}) = h_{12}(\boldsymbol{\alpha}) + 2\theta_1(\boldsymbol{\alpha}) + 2\theta_2(\boldsymbol{\alpha})h_{01}(\boldsymbol{\alpha}), \\ &f_{03}(\boldsymbol{\alpha}) = h_{03}(\boldsymbol{\alpha}) + \theta_2(\boldsymbol{\alpha}). \end{aligned} \tag{2.56}$$

Hence, by taking

$$\begin{aligned} \theta_1(\boldsymbol{\alpha}) &= -\frac{1}{2}h_{12}(\boldsymbol{\alpha}) + h_{01}(\boldsymbol{\alpha})h_{03}(\boldsymbol{\alpha}), \\ \theta_2(\boldsymbol{\alpha}) &= -h_{03}(\boldsymbol{\alpha}), \end{aligned}$$

we obliterate the $u_1u_2^2$ and u_2^3 terms, and obtain the following final form of Eq. (2.54):

$$\begin{cases} \dot{u}_1 = u_2, \\ \dot{u}_2 = \mu_1(\boldsymbol{\alpha})u_1 + \mu_2(\boldsymbol{\alpha})u_2 + a_3(\boldsymbol{\alpha})u_1^3 + b_3(\boldsymbol{\alpha})u_1^2u_2 + O(\|\boldsymbol{u}\|^5), \end{cases} \tag{2.57}$$

where $a_3 = h_{30}(\mathbf{0}) + O(\|\boldsymbol{\alpha}\|)$, $b_3 = h_{21}(\mathbf{0}) + O(\|\boldsymbol{\alpha}\|)$, and $\boldsymbol{\mu} = (\mu_1, \mu_2) = (h_{10}, h_{01})$.

Finally, if $a_3(\mathbf{0})b_3(\mathbf{0}) \neq 0$, introducing a new time variable and new state variables z_1, z_2 by the scaling

$$t_{\text{new}} = \left|\frac{a_3(\boldsymbol{\alpha})}{b_3(\boldsymbol{\alpha})}\right| t_{\text{old}}, \quad z_1 = \frac{|b_3(\boldsymbol{\alpha})|}{\sqrt{|a_3(\boldsymbol{\alpha})|}}u_1, \quad z_2 = \frac{b_3(\boldsymbol{\alpha})^2}{|a_3(\boldsymbol{\alpha})|^{3/2}}u_2, \tag{2.58}$$

we obtain the normal form below,

$$\begin{cases} \dot{z}_1 = z_2, \\ \dot{z}_2 = \beta_1 z_1 + \beta_2 z_2 + \sigma_1 z_1^3 + \sigma_2 z_1^2 z_2 + O(\|\boldsymbol{z}\|^5). \end{cases} \tag{2.59}$$

The two signs $\sigma_1 = \operatorname{sgn} a_3(\mathbf{0})$ and $\sigma_2 = \operatorname{sgn} b_3(\mathbf{0})$ determine the subtype of this bifurcation, and the unfolding parameters $\boldsymbol{\beta} = (\beta_1, \beta_2)$ are given by

$$\begin{aligned} \beta_1(\boldsymbol{\alpha}) &= \frac{b_3(\boldsymbol{\alpha})^2}{a_3(\boldsymbol{\alpha})^2}h_{10}(\boldsymbol{\alpha}), \\ \beta_2(\boldsymbol{\alpha}) &= \left|\frac{b_3(\boldsymbol{\alpha})}{a_3(\boldsymbol{\alpha})}\right| h_{01}(\boldsymbol{\alpha}). \end{aligned} \tag{2.60}$$

Again, it can be proved that the truncated normal form after abandoning the $O(\|\boldsymbol{z}\|^5)$ terms is a topological normal form. When $\sigma_1 = -1$, $\sigma_2 = -1$, the bifurcation diagram of the system (2.59) in the (β_1, β_2)-plane consists of the origin and the following bifurcation curves:

(a) $P_{\ominus}^{-} = \{(\beta_1, \beta_2) \,|\, \beta_1 = 0, \beta_2 < 0\}$;

(b) $P_{\oplus}^{+} = \{(\beta_1, \beta_2) \,|\, \beta_1 = 0, \beta_2 > 0\}$;

(c) $H_0^- = \{(\beta_1, \beta_2) \,|\, \beta_2 = 0, \beta_1 < 0\}$;

(d) $H_{\neq 0}^+ = \{(\beta_1, \beta_2) \,|\, \beta_2 = \beta_1 + O(\beta_1^2), \beta_1 > 0\}$;

(e) $HO = \{(\beta_1, \beta_2) \,|\, \beta_2 = \frac{4}{5}\beta_1 + O(\beta_1^{3/2}), \beta_1 > 0\}$;

(f) $SNL = \{(\beta_1, \beta_2) \,|\, \beta_2 = \kappa^* \beta_1 + O(\beta_1^{3/2}), \beta_1 > 0\}$, where $\kappa^* \approx 0.752$.

When $\sigma_1 = +1$, $\sigma_2 = -1$, the bifurcation diagram is simpler, comprising the origin and

(a) $P_\ominus^+ = \{(\beta_1, \beta_2) \,|\, \beta_1 = 0, \beta_2 < 0\}$;

(b) $P_\oplus^- = \{(\beta_1, \beta_2) \,|\, \beta_1 = 0, \beta_2 > 0\}$;

(c) $H_0^- = \{(\beta_1, \beta_2) \,|\, \beta_2 = 0, \beta_1 < 0\}$;

(d) $HE = \{(\beta_1, \beta_2) \,|\, \beta_2 = -\frac{1}{5}\beta_1 + O(\beta_1^{3/2}), \beta_1 < 0\}$.

Here, $P_\ominus$ and $P_\oplus$ denote pitchfork bifurcations occurring on attracting and repelling center manifolds, respectively, and HE stands for the heteroclinic bifurcation. Moreover, we use superscripts for pitchfork bifurcations as for Hopf bifurcations (tagged as P^-, H^- when supercritical, or P^+, H^+ when subcritical). As Eq. (2.59) remains invariant under $(\tau, u_2, \beta_2, \sigma_2) \to (-\tau, -u_2, -\beta_2, -\sigma_2)$, the bifurcation diagrams for $\sigma_2 = +1$ are simply the reflections of those for $\sigma_2 = -1$ about the β_1-axis, with the types of the bifurcation curves changed according to the changes in the stability of the related limit sets.

The bifurcation diagrams of the normal form Eq. (2.59) for $\sigma_1 = -1$, $\sigma_2 = -1$ and for $\sigma_1 = +1$, $\sigma_2 = -1$ are depicted in Figs. 2.6 and 2.7, respectively. In Fig. 2.6, the $\beta_1\beta_2$-plane is divided into six regions: a stable equilibrium in region ①, an unstable equilibrium and a stable limit cycle in region ②; crossing P^+ produces a pair of nontrivial equilibria, of which the subcritical Hopf bifurcation creates a pair of unstable limit cycles, in region ④; the two limit cycles merge into a larger unstable one in region ⑤ through the homoclinic bifurcation; finally, the unstable limit cycle annihilates with the stable one after crossing the curve SNL and entering ⑥. In Fig. 2.7, the $\beta_1\beta_2$-plane is divided into four regions: the origin is a saddle in region ①, and becomes stable with a pair of saddles appearing in region ②; the supercritical Hopf bifurcation of the origin yields a stable limit cycle in region ③, which becomes a pair of heteroclinic orbits on the curve HE and disappears after entering region ④. Such bifurcation scenarios will appear again when we analyze the plane wave dynamics of the chaotic neural field model in Chapter 4.

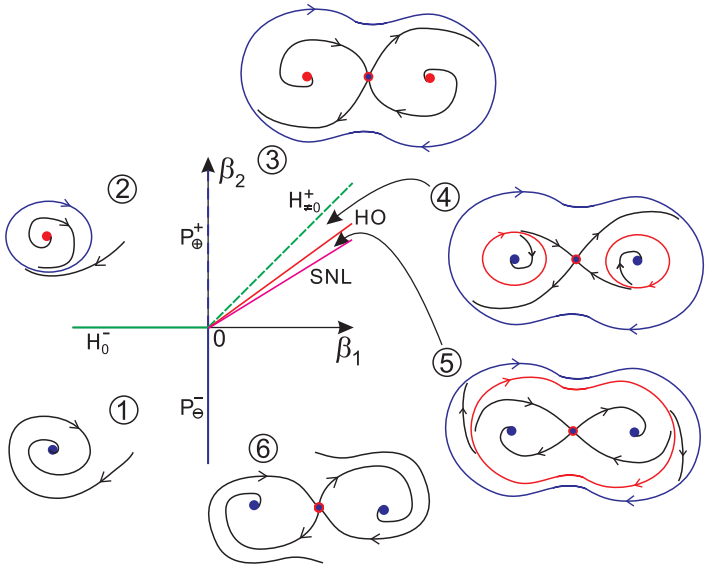

Figure 2.6: Bifurcation diagram for the BT bifurcation of the system (2.59) (the pitchfork case) for $\sigma_1 = \sigma_2 = -1$ (i.e., the homoclinic subtype). This diagram is a simplified one of Fig. 9.10 in [47], where the system (2.57) is treated as the normal form flow for 1:2 resonance.

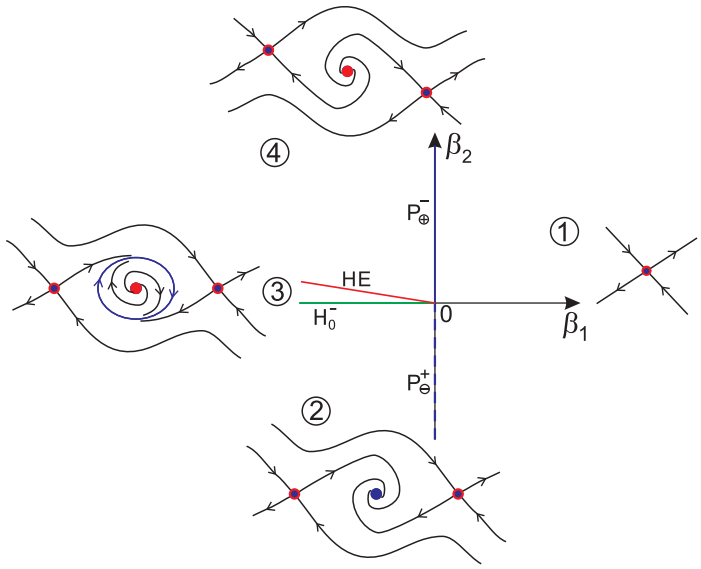

Figure 2.7: Bifurcation diagram for the BT bifurcation of the system (2.59) (the pitchfork case) for $\sigma_1 = +1$ and $\sigma_2 = -1$ (the heteroclinic subtype). This diagram is a simplified one of Fig. 9.9 in [47].

Chapter 3

Normal Form Derivation for BT Bifurcations

The BT bifurcation is quite ubiquitous in various systems that arise from the modeling of mechanical, physical, biological, geographical, and engineering problems. For a laser with an injected signal, the BT bifurcation occurs in the parameter space spanned by the amplitude and frequency detuning of the injection [108]; for the traveling wave solutions in pipe flow, the BT bifurcation occurs in the parameter space spanned by the Reynolds and wave numbers [62]; BT bifurcations also emerge in the Chua circuit [4], coupled homopolar dynamos [64], and even in a box model for the thermohaline circulation of the Atlantic, with the non-thermohaline freshwater fluxes as parameters [91]. Other situations for the occurrence of BT bifurcations include nonlinear oscillators, neuronal/neural systems, and population dynamics (see [40, 92, 107] for examples).

The analysis of a real-world system for BT and other bifurcations is often performed by reducing it to a proper parameter-dependent normal form. Nevertheless, the computation of the normal form of a system can be laborious in practice, particularly when it involves the restriction from higher dimensions to a lower-dimensional center manifold. To calculate the normal forms of general n-dimensional systems efficiently, Kuznetsov established a homological method that combines the procedures of restriction and normalization on the center manifold [50], and obtained explicit formulas for the coefficients of the smooth normal form at the BT bifurcation point up to the fourth order [48]. This homological method is also applicable in the parameter-dependent scenario [10]. Specifically, Kuznetsov considered the computation of parameter-dependent normal forms for the BT bifurcation with this method and used it in an improved homoclinic predictor [49]. The corresponding computation has also been carried out in a $\mathbf{Z}_2$-symmetric system [72]. However, the parameter transformation and transversality conditions therein are not provided in a sufficiently explicit and essential form, and are thus not readily applicable.

To be specific, let us consider the transformation between the parameters $(\alpha_1, \alpha_2) \in \mathbb{R}^2$ of an n-dimensional, $\mathbf{Z}_2$-symmetric system around its BT bifurcation point $\boldsymbol{\alpha} = \mathbf{0}$ and the

parameters $(h_{10}, h_{01}) \in \mathbb{R}^2$ in the corresponding system (2.51) (which can be seen as the normal form only up to a scaling). The previous study [72] found that if we let

$$\begin{bmatrix}\alpha_1\\ \alpha_2\end{bmatrix} = \begin{bmatrix}\alpha_{11} & \alpha_{12}\\ \alpha_{21} & \alpha_{22}\end{bmatrix}\begin{bmatrix}h_{10}\\ h_{01}\end{bmatrix} + \dots,$$

then the coefficients α_{ij} $(i, j = 1, 2)$ can be obtained by solving the linear system

$$\begin{bmatrix}\langle \boldsymbol{\varepsilon}_2, \boldsymbol{f}_1^1(\boldsymbol{e}_1, \cdot)\rangle\\ \langle \boldsymbol{\varepsilon}_1, \boldsymbol{f}_1^1(\boldsymbol{e}_1, \cdot) + \langle \boldsymbol{\varepsilon}_2, \boldsymbol{f}_1^1(\boldsymbol{e}_2, \cdot)\rangle\end{bmatrix}\begin{bmatrix}\alpha_{11} & \alpha_{12}\\ \alpha_{21} & \alpha_{22}\end{bmatrix} = \begin{bmatrix}1 & 0\\ 0 & 1\end{bmatrix}.$$

where $\boldsymbol{e}_1, \boldsymbol{e}_2, \boldsymbol{\varepsilon}_1, \boldsymbol{\varepsilon}_2 \in \mathbb{R}^n$ are generalized eigenvectors and $\boldsymbol{f}_1^1 : \mathbb{R}^n \times \mathbb{R}^2 \to \mathbb{R}^n$ is one of the multilinear function given by the system equation (both to be explained later). The invertibility of the left-most matrix can be a transversality condition, whose satisfaction guarantees the solvability of the above equation and leads to

$$\frac{\partial(h_{10}, h_{01})}{\partial(\alpha_1, \alpha_2)} = \begin{bmatrix}\alpha_{11} & \alpha_{12}\\ \alpha_{21} & \alpha_{22}\end{bmatrix}^{-1} = \begin{bmatrix}\langle \boldsymbol{\varepsilon}_2, \boldsymbol{f}_1^1(\boldsymbol{e}_1, \cdot)\rangle\\ \langle \boldsymbol{\varepsilon}_1, \boldsymbol{f}_1^1(\boldsymbol{e}_1, \cdot) + \langle \boldsymbol{\varepsilon}_2, \boldsymbol{f}_1^1(\boldsymbol{e}_2, \cdot)\rangle\end{bmatrix}. \tag{3.1}$$

This is a good result, but some subtle problems remain. First, here the formula (3.1) is only proved with a prerequisite transversality, and the extension to an m-parameterized case requires the transversality for any two parameters. In fact, Eq. (3.1) holds for an arbitrary number of parameters no matter the transversality condition is satisfied or not, as will be seen later. Second, this formula does not reveal the essential feature of the parameter transformation that (h_{10}, h_{01}) is related with the eigenvalues. Furthermore, there are six more coefficients to be found from a linear system of six equations, for us to know the second-order terms of the parameter transformation.

In this chapter, the homological computation of the universal unfoldings for the BT bifurcation in n-dimensional systems is re-investigated. It is shown that with a reversed expansion of parameters (compared with past studies) the parameter transformation (at least the linear part) can be expressed in quite explicit forms for any dimensionality m of the original parameters. Specifically, the following improvements are made:

(i) Simple formulas are made available for the linear part of the parameter transformation using either the characteristic polynomial or the (generalized) eigenvectors of the Jacobian matrix, in the case of an equilibrium that endures after any parameter perturbation (including but not limited to the $\mathbf{Z}_2$-symmetric case);

(ii) The condition of $\mathbf{Z}_2$-symmetric systems has been generalized compared with that considered in [72] as long as the equilibrium is enduring, and the above-mentioned formulas can be applied within certain subspaces;

(iii) In the general case, the result in [12] is re-derived in a slightly different form and then revised to determine the bifurcation diagram to the second order.

These results accelerate the transversality check and depiction of the bifurcation diagrams, which can be demonstrated by some examples provided in Appendix A.

Chapter 4

Plane Waves in Chaotic Neural Field Model

The spatiotemporal evolution of neurodynamics is often studied on a macroscopic scale using neural field models, i.e., the continuum limits of neural networks, because of the immense number of neurons and synapses in actual situations. One important early work is due to Amari [5], who studied the pattern formation in a neural field that corresponds to a "Mexican hat" synaptic connection. Typical neural field models are of the form

$$\tau_d \frac{\partial u(\boldsymbol{x},t)}{\partial t} = -u(\boldsymbol{x},t) + \int W(\boldsymbol{x},\boldsymbol{y})\, f(u(\boldsymbol{y}, t-|\boldsymbol{x}-\boldsymbol{y}|/v_c))\, d\boldsymbol{y},$$

where $u(\boldsymbol{x},t)$ is the local activity being studied, $W(\boldsymbol{x},\boldsymbol{y})$ is the synaptic connection from the cite $\boldsymbol{y}$ to $\boldsymbol{x}$, f is the output function, and τ_d and v_c here are constants characterizing the decay time and conduction speed, respectively. Different connection schemes, output functions, single-neuron dynamics, and even inhomogeneity have been considered to model various neural phenomena. Specifically of interest is the pattern formation in such models, such as localized bumps or breathers, and traveling waves [14, 17].

The famous model for excitable media, FitzHugh–Nagumo equation, can be deemed as some kind of neural field that corresponds to a network of FitzHugh–Nagumo neurons. The plane wave dynamics of the FitzHugh–Nagumo equation has been investigated in [13, 26, 27] from the perspective of bifurcations in the parameter space (including the wave speed as a parameter). A C-shaped homoclinic bifurcation curve and a U-shaped Hopf bifurcation curve were identified, and the interaction of these bifurcations in such a C–U structure were analyzed in detail.

Neural network models with a potential in solving practical problems can also be platforms for pattern formation. Specifically, the chaotic neuron model [2] uses two variables to describe the neuronal activity with refractoriness, and Hopfield-like neural networks constructed with such chaotic neurons have been used frequently for dynamic associative memory [1, 34, 46, 97]. By restricting the connection to a small local region in a large-scale network, a novel association scheme is realized: stored 2D images appear in fragments and

their boundaries evolve with time, exhibiting moving clusters, traveling plane waves and spiral waves [67].

As the starting step of promoting the application of such an associative cellular CNN, we attempt to analyze its plane wave dynamics under highly simplified conditions. Then, we will approximate the network to a corresponding neural field model, to which we apply bifurcation analysis to study the plane wave dynamics in the parameter space. It will turn out that the analysis of BT bifurcation using the method given in the preceding chapter produces useful information quickly. Some other issues, such as the dispersion relation for small amplitudes and the stability, are also considered. These results demonstrate the representative plane wave dynamics in the parameter space for similar oscillatory media with a $\mathbf{Z}_2$ symmetry and may serve as supplements to the previous analysis of plane wave dynamics in typical excitable media without the $\mathbf{Z}_2$ symmetry.

4.1 Field model for a cellular chaotic neural network (CNN)

The CNN model with a simplified parameter setting and local connection scheme is given in this section. Furthermore, this neural network model is continuized both in space and in time and is thus turned into a neural field model, which facilitates approximate analysis.

4.1.1 Simplified associative cellular CNN

The CNN is a single-layered discrete-time recurrent neural network, composed of chaotic neurons characterized by a refractoriness term and a continuous output function [2]. Each neuron receives feedback inputs from certain neurons in the network and external inputs from outside, where the refractoriness counteracts these inputs. If the total external input to a neuron is temporally constant, it is usually incorporated into another component to obtain a concise expression. Thus, a neuron's state is determined by two state variables and the CNN's dynamics can be described by the following difference equations [1]:

$$\boldsymbol{\zeta}(t) = k_r \boldsymbol{\zeta}(t-1) - \alpha \boldsymbol{x}(t-1) + \boldsymbol{a}, \tag{4.1a}$$

$$\boldsymbol{\eta}(t) = k_f \boldsymbol{\eta}(t-1) + \mathbf{W}\boldsymbol{x}(t-1), \tag{4.1b}$$

$$\boldsymbol{x}(t) = \boldsymbol{s}\left(\boldsymbol{\zeta}(t) + \boldsymbol{\eta}(t)\right), \tag{4.1c}$$

where $\boldsymbol{\zeta} = [\zeta_1\ \zeta_2\ \cdots\ \zeta_n]^\top$, $\boldsymbol{\eta} = [\eta_1\ \eta_2\ \cdots\ \eta_n]^\top$, and $\boldsymbol{x} = [x_1\ x_2\ \cdots\ x_n]^\top$ are time-dependent vectors that represent each neuron's refractory internal state, feedback internal state, and output, respectively, and n is the number of neurons in the network. $\boldsymbol{a} = [a_1\ a_2\ ...\ a_n]^\top$ is also an n-dimensional vector, which denotes the external inputs with the corresponding activation threshold values deducted. $k_r, k_f \in [0, 1)$ are the decay parameters for the two internal states and $\alpha \geqslant 0$ regulates the strength of refractoriness. To make a network, the $n \times n$ matrix $\mathbf{W} = (w_{ij})$ defines the synaptic weight from the jth neuron to the ith neuron with its entry w_{ij}. Finally, the mapping $\boldsymbol{s}$ applies a sigmoidal activation function

to every component of its vectorial argument, i.e., $\boldsymbol{s}(\boldsymbol{y}) = [s(y_1)\ s(y_2)\ \cdots\ s(y_n)]^\top$, where $s(y) = (1+\exp(-y/\epsilon))^{-1}$ and ϵ is a steepness parameter. The dynamics of the CNN model given by Eq. (4.1) is illustrated graphically in Fig. 4.1.

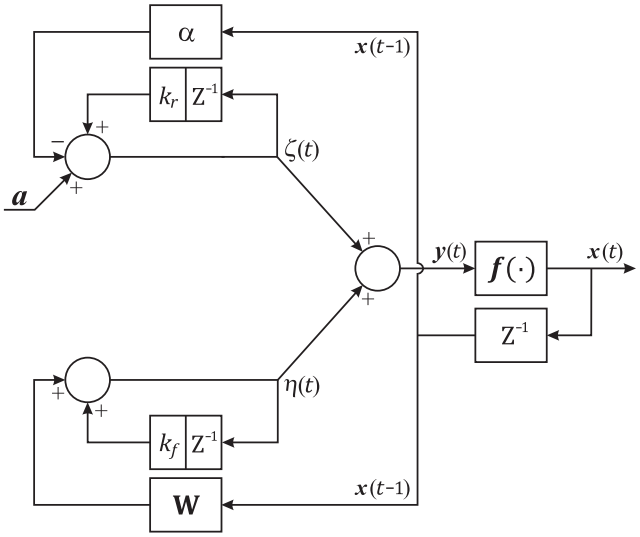

Figure 4.1: Block diagram of the CNN model. Here, Z^{-1} represents backward shift by one time step and it is sometimes combined with constant scaling (by k_r or k_f) for simplicity; the output function $\boldsymbol{f}$ can be the sigmoid function as in Eq. (4.1).

To perform auto-associative memory, several binary images with pixel values mapped from $\{0, 1\}$ to $\{-1, 1\}$ can be stored in the CNN by using an autocorrelation weight matrix as in a Hopfield network. Many CNN-based association models employ this conventional encoding regime, and they either exhibit indeterminate wandering among basal patterns or exclusive visits to only specific patterns ([1, 34, 35, 36, 52, 97]). In addition, grayscale and color images can be memorized in a similar manner except that one pixel corresponds to more than one neuron, e.g., 24 neurons for 24-bit RGB images [66]. In fact, this is the original reported situation where traveling waves emerge in associative CNNs, which carry pieces of different basal patterns and produce mixed outputs. However, we do not consider the image format or the pattern switch/immobilization process, but we focus on the following simplified conditions in our investigation of traveling waves.

(i) The net external input is spatially uniform and all components are $\alpha/2$, i.e., $\boldsymbol{a} = \alpha\mathbf{1}/2$ where $\mathbf{1}$ is the all-ones vector.

(ii) A single checkerboard pattern expressed by $\boldsymbol{e} \in \{0, 1\}^n$ after a row-wise scan is memorized in an $m \times m$ neuronal lattice, where m is even and $m^2 = n$.

(iii) Synaptic connections to the ith neuron are only allowed from a square neighborhood centering around the neuron, which covers $(2d+1)^2$ neurons, and the indices of these neurons are grouped in a set S_i, i.e., $S_i = \{j \mid d_T(i, j), d_L(i, j) \leqslant d\}$, where $d_T(i, j)$ and $d_L(i, j)$ denote the transverse and longitudinal distances between the ith and jth neurons, respectively, for $i, j = 1, 2, ..., n$.

(iv) Periodic boundary conditions are imposed in both directions such that $d_T(i,j) = m/2 - |m/2 - (|i-j| \bmod m)|$ and $d_L(i,j) = m/2 - |m/2 - |\lceil i/m \rceil - \lceil j/m \rceil||$, where $\lceil \cdot \rceil$ signifies the ceiling function and mod denotes the modulo operation that takes the smallest non-negative remainder. In this manner, the weight matrix $\mathbf{W} = (w_{ij})$ is given by

$$w_{ij} = \begin{cases} \beta(2e_i - 1)(2e_j - 1) = (-1)^{i+j+\lceil \frac{i}{m} \rceil + \lceil \frac{j}{m} \rceil} & \text{for } j \in S_i \ (i \in S_j), \\ 0 & \text{otherwise.} \end{cases} \tag{4.2}$$

Condition (i) makes the oscillation range of the refractory states ζ_i symmetric about $\zeta = 0$ between $\pm\alpha/2 \cdot (1 - k_r)^{-1}$, while Condition (ii) leads to an identical synaptic environment for every neuron as well as a symmetric oscillation range about $\eta = 0$ for the feedback states η_i. Their combination ensures the invariance of the system under the transform $(\boldsymbol{\zeta}, \boldsymbol{\eta}) \to (-\boldsymbol{\zeta}, -\boldsymbol{\eta})$ $(\boldsymbol{x} \to \mathbf{1} - \boldsymbol{x})$, and this invariance can be preserved approximately even if the network only has local connections, as assumed in Conditions (iii) and (iv).

In Fig. 4.2, we show the stored pattern $\boldsymbol{e}$ and its reversal $\overline{\boldsymbol{e}}$ for a CNN that comprises $n = 2500$ neurons, where each pixel is filled with a block ■, denoting 1, or a dot $\cdot$, denoting 0. The CNN's output $\boldsymbol{x}$ can be illustrated in a similar manner by distinguishing between a firing neuron ($x_i > 0.5$, denoted as 1) and a resting one ($x_i \leqslant 0.5$, denoted as 0). To allow a clearer visualization, we display a converted output $\boldsymbol{x}^* \in \{0,1\}^n$ instead of the original digitized $\boldsymbol{x}$ by using a pixel-wise XOR operation with $\boldsymbol{e}$, i.e., $x_i^* = e_i \oplus \lceil x_i - 0.5 \rceil$ for $i = 1, 2, ..., n$. This treatment transforms $\boldsymbol{e}$ and $\overline{\boldsymbol{e}}$ to $\boldsymbol{e}^* = \mathbf{0}$ and $\overline{\boldsymbol{e}}^* = \mathbf{1}$, thereby facilitating the observation of the output patterns as the wave in the network transmits the collective activation of $\boldsymbol{e}$ or $\overline{\boldsymbol{e}}$, and the spatiotemporal output is a mixture of both.

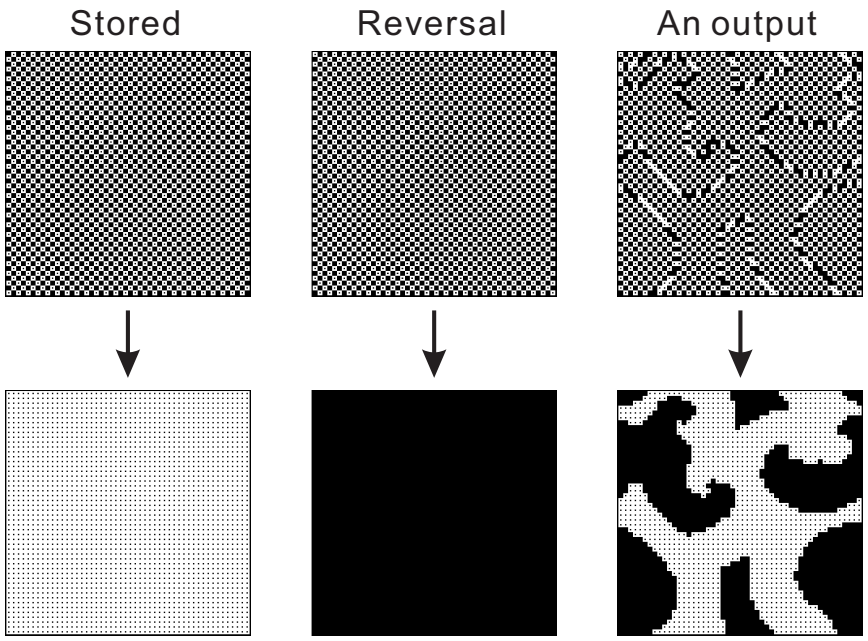

Figure 4.2: The original digitized patterns shown in the top row and their converted versions in the lower row. The stored pattern $\boldsymbol{e}$, its reversal $\overline{\boldsymbol{e}}$, and an example output $\boldsymbol{x}$ are shown from left to right. The differentiation between the stored pattern and its reversal is relative, but we specify it here only for certainty. The necessity of the XOR operation is obvious from this figure and this treatment is used throughout this study when displaying output sequences.

Chapter 5

Spiral Waves in the Cellular Chaotic Neural Network

In two-dimensional spatially extended dynamical systems, other traveling waves than plane waves, for example, spiral waves, may emerge. Spiral waves are quite general phenomena in excitable and oscillatory media and their mathematical models. The celebrated example, spiral wave in the Belousov–Zhabotinsky reaction, has been extensively studied [43, 55, 80, 87, 93]. These constitute a large family of researches about waves and patterns in chemical and biochemical reactions [42]. In recent years, spiral waves have been frequently discovered in the cortex [8, 38, 39, 53, 89, 94], due to the advances in signal detection and imaging technology, and are attracting increasing interest.

For spiral waves (and the chaotic spiral states after breakups), a particular research theme is their control. Several schemes were proposed to eliminate the spiral waves in excitable and oscillatory media. A mesh control scheme for a modified FitzHugh–Nagumo system (also referred to as Barkley model) was proposed in [84], where applying a shock on the mesh lines absorbs the spirals formed inside each block. Another method is to apply an external, periodic input to induce target waves, which can replace the spiral waves and spatiotemporal chaos in the Barkley model and a model for cardiac muscle [103], as well as in networks of Hodgkin–Huxley neurons [59]. In addition, a phase space constraint method was used to remove spiral waves in modified FitzHugh–Nagumo systems [58] and in coupled Chua circuits [96]. For spiral waves in the cortex, despite the belief that their genesis, evolution, and termination are controlled via long-range synaptic connections, the specific control scheme is not clear.

The existent researches above may have some limitations under certain circumstances. These researches usually focus on changing the spiral wave state into a homogeneous state (of the excitable medium), and the possibility of getting other non-spiral wave states was not considered. Another potential limitation is that the control usually needs to be stopped manually after spiral wave elimination, rather than terminated automatically in a self-adaptive manner: this is definitely not biologically realistic as observed in experiments.

As a system with variant reaction-diffusion characteristics, it is definitely possible for the cellular CNN to demonstrate various behavior beyond the Turing stability, including

spiral waves. Further application of the cellular CNN as platforms for associative memory may require schemes for manipulating the traveling wave dynamics, e.g., transforming the spiral wave states to other states. In this chapter, we investigate the spiral wave dynamics in the cellular CNN under the simplified settings, with an emphasis on proposing a dynamic phase space constraint (DPSC) method to eliminate the spiral waves. Compared with the past studies of spiral wave elimination, the following improvements are achieved:

(i) After spiral wave elimination, the control mechanism spontaneously stops, and the network naturally converges to its intrinsic non-spiral states;

(ii) The network can be controlled to not only synchronized states but also various plane wave states; the proportion of synchronized states as the control outcome in all trials, and the proportion of long-period states in both control outcomes are tuned by the control parameter.

5.1 Uncontrolled spiral wave dynamics

In this section, we present the spiral wave dynamics of the simplified cellular CNN under free conditions, i.e., without control. We start with the output sequence of the network in a specific case, demonstrate the amplitude reduction phenomenon near the phase singularity, and then carry out a statistical investigation. The amplitude reduction phenomenon is shown to be an indicator of the existence of spiral waves and will play a role in the flexible control scheme of spiral waves later.

5.1.1 Output sequence of a specific spiral state

We stick to the highly simplified and symmetric setting of parameters and weights in the CNN as described in Sec. 4.1.1. Relevant parameters for the network are set as follows: $k_r = 0.95$, $k_f = 0.15$, $\alpha = 4.0$, $\varepsilon = 0.02$, and the half connection length $d = 2$. Chaotic spiral wave states can be easily generated by assigning random initial values to the internal states of all neurons. Specifically, we randomly selected $\zeta_i(0) \in \left[-\frac{\alpha}{2(1-k_r)}, +\frac{\alpha}{2(1-k_r)}\right]$ and $\eta_i(0) \in \left[-\frac{(2d+1)^2}{2(1-k_f)}, +\frac{(2d+1)^2}{2(1-k_f)}\right]$, for all neurons in a 50×50 neuronal lattice ($i = 1, 2, ..., 2500$), in all our simulations in this chapter.

A typical output sequence of the free cellular CNN, which starts from random internal states, is illustrated in Fig. 5.1. In the early stage of the evolution, a clustering process occurs as a consequence of local connection, where every neuron tends to conform its output to either the stored pattern $\boldsymbol{e}$ (meaning $x_i^* = 0$) or its reversal $\overline{\boldsymbol{e}}$ ($x_i^* = 1$) by following the current status of the majority of its neighboring neurons. This process differs from pattern completion by a Hopfield-type network because the convergence to $\boldsymbol{e}$ or $\overline{\boldsymbol{e}}$ operates locally, thereby producing a mixture of both, and the relatively large refractoriness cancels the fixed points, which gives the clusters ever-changing boundaries. Subsequently, these volatile clusters settle into spiral waves, some of which are less robust

and they may disappear in tens of steps, whereas the remainders are quite stable and they keep rotating for an extremely long period of time. As shown in Fig. 5.1, four spirals are maintained in the upper field of view (FOV) and they rotate once in about 18 time steps. These are the spiral waves that we need to detect and eliminate in later sections.

5.1.2 Amplitude reduction phenomenon

An arising problem is how to determine whether spiral waves exist and where they are in the network. This problem may be solved by checking for the two hallmarks of spiral waves: phase singularity and amplitude reduction. The former is the intersection of all phases, and the latter refers to a phenomenon where the oscillation amplitude is reduced near the phase singularity. To decompose complex oscillatory motion and find the instantaneous phase and amplitude, a powerful tool is the Hilbert transform, which has been applied frequently in experimental signal processing for neural oscillations and brain waves [18, 39, 90, 104]. However, the Hilbert transform might be unsuitable if we need a real-time indicator of spiral waves, since the Hilbert transform requires evaluation of an improper integral. Fortunately, compared with the phase, which is less convenient to calculate, the amplitude reduction is much easier to quantify. Therefore, we utilize this phenomenon and define a local index h_i for the ith neuron,

$$h_i(t) = k_h h_i(t-1) + \log_{10}\left(1 + |\eta_i(t-1)|\right), \tag{5.1}$$

which measures the amplitude of its feedback state η_i (k_h is a decay parameter). With a proper value of k_h, we note that h_i has relatively low values when the neuron is near a phase singularity, and vice versa.

The amplitude reduction in the feedback internal state $\boldsymbol{\eta}$ is related to the working mechanism of the weight matrix $\mathbf{W}$ given by Eq. (4.2). The left-multiplication of $\mathbf{W}$ on an output $\boldsymbol{x}$ yields a vector in which the ith component is

$$\begin{aligned}(\mathbf{W}\boldsymbol{x})_i &= \sum_{j=1}^{n} w_{ij}x_j = (2e_i - 1)\sum_{j\in S_i}(2e_j - 1)x_j \\ &= (2e_i - 1)\sum_{j\in S_i}\left(e_j - |e_j - x_j|\right) = \left[F_i - H_i(\boldsymbol{x})\right](2e_i - 1),\end{aligned} \tag{5.2}$$

where $F_i = \sum_{j\in S_i} e_j$ is the local firing number (the number of "1"'s) for the stored pattern $\boldsymbol{e}$ within the region connected to the ith neuron, and $H_i(\boldsymbol{x}) = \sum_{j\in S_i}|e_j - x_j|$ is a generalized local Hamming distance between $\boldsymbol{x}$ and $\boldsymbol{e}$. The usual Hamming distance counts the number of pixels that differ in two binary strings, whereas $H_i(\boldsymbol{x})$ narrows down the count to the ith neuron's neighborhood S_i, takes continuous arguments in $[\,0, 1\,]^n$ instead of digitized ones, and still returns an approximate value, $H_i(\boldsymbol{x}) \approx \sum_{j\in S_i}|e_j - \lceil x_j - 0.5\rceil| = \sum_{j\in S_i} x_j^*$. In the proposed model, we have $F_i = \left(|S_i| \pm 1\right)/2$, where $|S_i| = (2d+1)^2$ is the size of the local connection region. The phase singularity is revolved around constantly by two intertwining

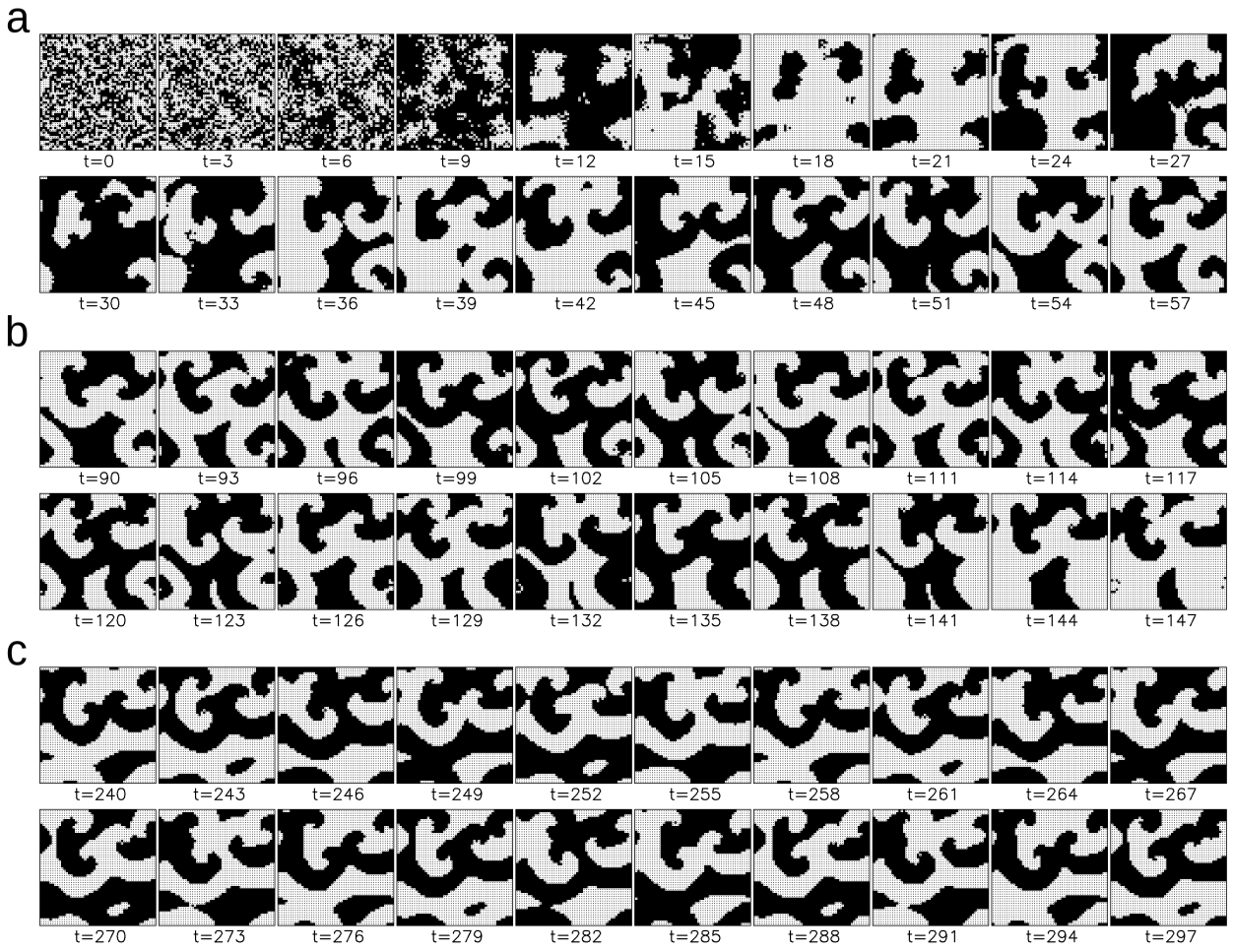

Figure 5.1: Output sequence segments from the network before control, where one out of every three time steps is successively displayed due to space limitations. (a) Clustering occurs in a dozen steps at first, before three pairs of spirals emerge in the upper left, upper right, and lower right parts in the field of view. (b) The lower right pair is unstable and it annihilates at around $t \approx 130$. (c) A spiral wave state is formed by the four remaining spirals, with an approximate period of 18 steps.

output pieces of $\boldsymbol{e}$ and $\overline{\boldsymbol{e}}$, which spiral into it, so the value of $H_i(\boldsymbol{x})$ at this point remains at about $|S_i|/2$, and this greatly attenuates the magnitude of $(\mathbf{W}\boldsymbol{x})_i$ as well as that of η_i because $\mathbf{W}\boldsymbol{x}$ is the dominant part of $\boldsymbol{\eta}$. By contrast, when the entire local output is taken over by $\boldsymbol{e}$ and $\overline{\boldsymbol{e}}$ alternately, the feedback state η_i of a neuron away from the phase singularity may oscillate in a wider range, which is roughly between $\pm|S_i|/2 \cdot (1-k_f)^{-1}$. Finally, the influence of the changing phase is filtered out by the exponential moving average in Eq. (5.1), and sustained low and high values of the local index $h_i(t)$ can be expected for neurons near and far from the phase singularity, respectively.

We now demonstrate the performance of the designed local index h_i for the detection of spiral waves. The value of the parameter k_h is chosen as $k_h = 0.95$. The initial values were set as $h_i(0) = 0$ for all neurons in the network, and these values actually would have little influence on the later values of h_i after a period of time. The location of the spiral wave based on amplitude reduction near phase singularities through the local index h_i is illustrated in Fig. 5.2. We selected two representative neurons, i.e., one (the 1020th) near a phase singularity and the other (the 2270th) in an ordinary position, and we show their motion ($t = 201 \sim 300$) in the ζ–η phase plane in Fig. 5.2(a). Compared with the latter neuron, which circles the origin with a longer distance, the excursion of the former appears to be more uniformly distributed and bound up in a closer region to the origin, where it exhibits apparent amplitude reduction. Accordingly, in the spatial local index profile of Fig. 5.2(b), four deep pits emerge and they clearly mark the sites of phase singularities; the value of h_i there decreases dramatically to less than 10 from about 20, which is the level in most of the area that contains no singularity. Moreover, although Fig. 5.2(b) is a snapshot at $t = 300$, this profile is preserved well in a short period and it only changes slowly with time. These verify the validity of using h_i to find the location of spiral waves.

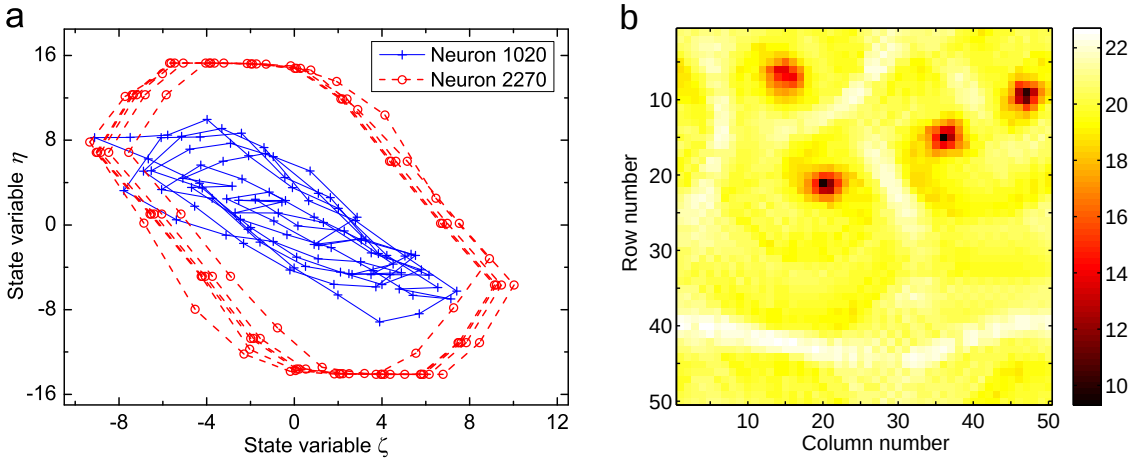

Figure 5.2: Phase singularity detection based on amplitude reduction. (a) The excursions of neurons 1020 and 2270 in the ζ-η plane during $t = 201 \sim 300$. Neuron 1020 is in row 21, column 20, near a phase singularity, and neuron 2270 is 25 rows below neuron 1020 in the FOV. (b) The spatial profile of h_i at $t = 300$. The locations of the four spiral pivots are clearly marked and one of them coincides with neuron 1020.

5.1.3 Statistical investigation of spiral dynamics

We now consider the following issues: the number of spirals that can coexist in the neuronal lattice and whether they have a characteristic rotation frequency. Hence, we performed statistical investigations based on 5000 trials where the CNN started from random initial states, and summarized the simulation results for the network's dynamics in Fig. 5.3.

Figures 5.3(a)∼(c) present the local index profiles with various numbers of spirals and Fig. 5.3(d) gives the frequency distribution of the spiral count. At $t = 10^4$, in 4991 trials, the CNN had 14 non-periodic spiral waves at most, but it evolved spontaneously into a non-spiral periodic state in only 9 trials. We also found that the number of stably existing spirals was always even, as reported in [66], and that spirals could be annihilated in pairs during the CNN's long-term evolution. Thus, the frequency of smaller numbers of spirals ($\leqslant 8$) increased slightly at $t = 10^4$ compared with that at $t = 300$, and the average number of spirals decreased slightly from 7.01 to 6.90 over the same period. These results suggest that chaotic spiral waves could be generated easily and maintained robustly in the locally connected CNN.

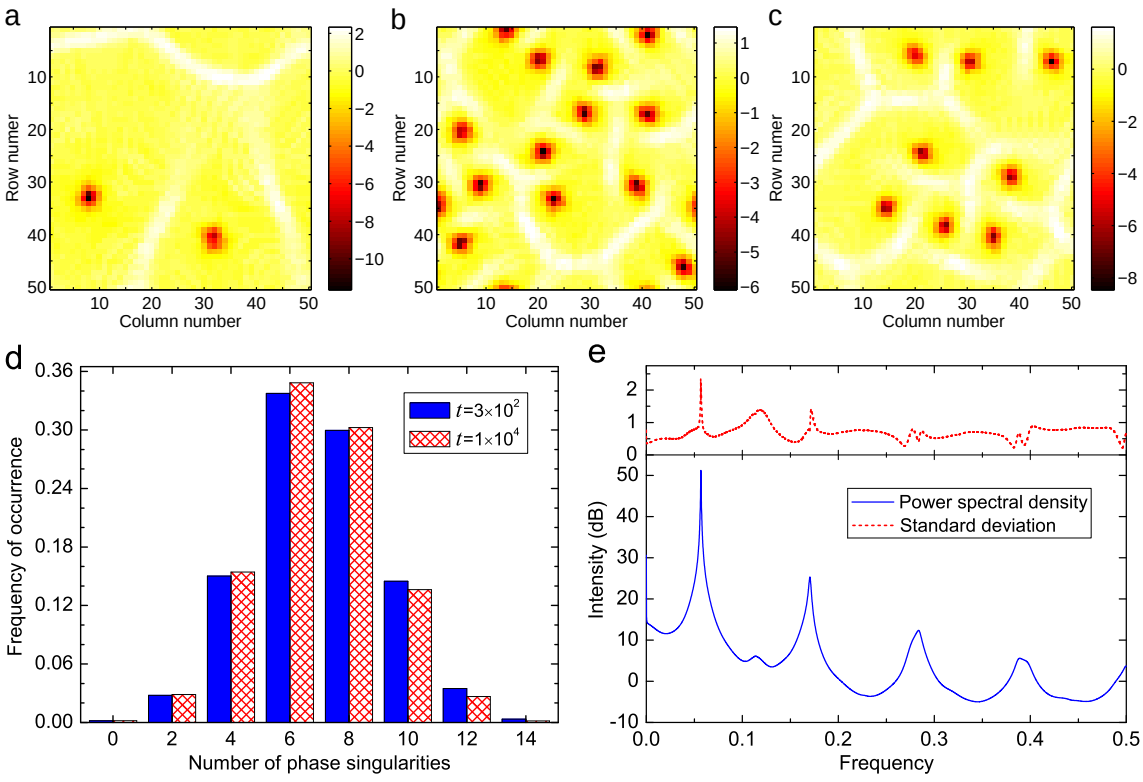

Figure 5.3: Simulation results obtained for uncontrolled networks. (a)∼(c) Spatial profiles of the normalized local index $\frac{h_i-\overline{h}}{\sigma_h}$ ($\overline{h}$ denotes the mean and σ_h is the SD of all h_i in the network at a specific time step) in our simulations, showing 2, 14, and 8 spirals, respectively. (d) The normalized frequency of the number of spirals at $t = 3 \times 10^2$ and $t = 1 \times 10^4$. (e) The grand mean power spectrum for y_i in all 4991 trials. In this case, the SD only considers the difference among trials to demonstrate the consistency of the average power spectra in various spiral wave states, with a maximum of only 2.35 dB.

In addition, in every trial where the spiral waves remained, we calculated the average power spectrum for $y_i(t) = \eta_i(t) + \zeta_i(t)$ over all neurons as a normalized characteristic of the overall network dynamics, and the grand mean and SD obtained over all 4991 trials are shown in Fig. 5.3(e). The relatively sharp peaks indicate nearly periodic motion and the dominant frequency $f_d = 0.0569$ corresponds to an approximate period of $T_a = 17.6$, thereby agreeing with the observations based on the specific case in Section 5.1.1. The limited peak width and SD value also reflect the high consistency of the power spectra for diverse spiral wave states, which implies that the dominant frequency f_d is probably common and that it depends only on the model parameters used in the cellular CNN.

To summarize, the spiral wave states in the network appear to be chaotic, in the sense that neither temporal nor spatial periodicity is found in a long run of the network. At the same time, these spiral wave states have an approximate period: once every this period, the network outputs close spiral patterns that never exactly repeat. These chaotic spiral waves are also "stable", in the sense that after a short transient phase after their births, they can be maintained for a long time with only occasional annihilation; when a small shock perturbation of all the state variables is applied to the network, the sensitivity to initial conditions indicates that it cannot return to the original orbit; nevertheless, the new orbit is still a spiral wave state with the same number of spiral waves as before at least temporarily. In other words, the spiral waves are robust to global small shock perturbation, and we need to use other methods to eliminate them.

5.2 Dynamic phase space constraint (DPSC)

We next turn to the control of the spiral wave dynamics and propose the control method for eliminating spiral waves. We first briefly introduce the historical aspect and basic idea of DPSC, and then describe the specific design for our present task.

5.2.1 Static and dynamic phase space constraint

The idea of using (static) phase space constraint was initially proposed for terminating the chaos (and superchaos) in several systems including the Lorenz system, the Rössler system, and the Hénon map [56]. As indicated by its name, this method used constant threshold values as the boundaries of the allowed range of the state variables, which leads to periodic orbits in place of chaos. Such a control scheme is simple to implement; however, it actually changes the dynamics of the system, and the resultant periodic orbits are no longer those of the original systems.

The phase space constraint method was later applied to control the spatiotemporal chaos in some spatially extended dynamical systems. The spiral waves in several typical models of excitable media (the Barkley model, cardiac muscle model mentioned previously and the model for BZ reaction) can be eliminated and the excitable media finally go to the homogeneous state, after imposing the constraint to the activator variable of the systems

in a certain spatial region [58]. Similar results were obtained for locally-coupled networks composed of Hodgkin–Huxley neurons [59] as well as Chua oscillators [96].

The application of phase space constraint to auto-associative CNNs was also proposed. The dynamic memory retrieval of the associative CNN is seemingly random: it chaotically jumps from one of the stored patterns to another, and this process will never stop. Hence the problem of controlling this chaotic retrieval for information processing emerges. A natural idea is to impose phase space constraint to the refractory internal states $\boldsymbol{\eta}$ of the neurons, which are responsible for the occurrence of chaotic dynamics in the CNN. This was attempted first in [32], where the output of the network converged to only one of the stored patterns, under static constraints. In spite of the successful termination of chaos, the dynamics of the network under such static constraints is almost degenerate into that of the Hopfield neural network. Thus, more flexible constraint schemes, where the limiting threshold values are no longer simply constant, were proposed [36, 52]. Then the associative CNN would be controlled to a periodic orbit, where the only visited stored pattern is the one that is most similar to the initial pattern of the network.

The basic idea of DPSC is to construct a control signal u from the feedback internal states $\boldsymbol{\eta}$, which contain information about the retrieval of the network, and then constrain $\boldsymbol{\zeta}$ within an allowable range modulated by u, as shown schematically in Fig. 5.4. In [52], the control signal $u(t)$ was chosen as the average of the instant values of $|\eta_i(t)|$ over all neurons, which has a larger value if the network has a closer output to one of its stored patterns. Then the refractory states ζ_i were truncated by a limiting threshold $\zeta^*(t)$ that increases with the control signal, so that the network was set free when it retrieved some stored pattern and was constrained when it was about to jump out of this pattern. With a proper setting, the network was finally trapped to a periodic motion around this stored pattern. For a different purpose (e.g., eliminating spiral waves), the specific design of the control signal formation and control exertion procedures of DPSC may vary accordingly, but follow a similar fashion.

5.2.2 DPSC for eliminating spiral waves in cellular CNN

We first demonstrate in a half-quantitative manner the effectiveness of eliminating spiral waves in the cellular CNN using a static phase space constraint. We believe that, if there are spiral waves rotating periodically in the network, such states cannot be maintained under a sufficiently small upper limit ζ^* for the absolute value of the refractory states ζ_i.

Let us imagine that a wavefront dividing $\boldsymbol{e}$ and $\overline{\boldsymbol{e}}$ sweeps over a neuron, whose representing point in the ζ-η phase plane, (ζ_i^0, η_i^0) at time t_0 satisfying $-\eta_i^0 < \zeta_i^0 < 0$ or $-\eta_i^0 > \zeta_i^0 > 0$, moves across the line $\zeta + \eta = 0$ to (ζ_i^1, η_i^1) at $t = t_0 + 1$. We can expect that this transition would happen at a similar level of $|\zeta_i|$ for different neurons regardless of their distances from the phase singularity; this is a natural consequence of the fact that these neurons must share a common period in the spiral, and the neurons of the same phase almost share a common motion in $\zeta_i(t)$ according to Eq. (4.1); the scaled output $2s(y) - 1$

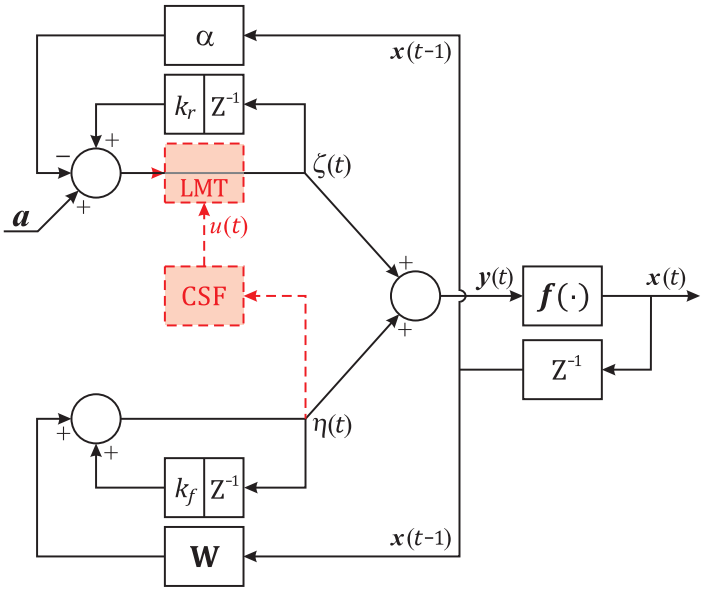

Figure 5.4: Block schematic of the CNN model under DPSC (parallel to Fig. 4.1), where CSF is short for control signal formation, and LMT is an amplitude limiter.

here with a small ϵ is approximately deemed to be the sign function $\operatorname{sgn} y$. On the other hand, this single neuron's output transition occurs if and only if $(\zeta_i^0 + \eta_i^0)(\zeta_i^1 + \eta_i^1) < 0$, which in a free network amounts to

$$\left(\zeta_i^0 + \eta_i^0\right)\left[k_r\zeta_i^0 + k_f\eta_i^0 - \frac{1}{2}\alpha \operatorname{sgn}(\zeta_i^0 + \eta_i^0) + \left(\mathbf{W}\boldsymbol{x}^0\right)_i\right] < 0, \tag{5.3}$$

where $\boldsymbol{x}^0$ is the output of the network at $t = t_0$. Then using Eq. (5.2), we obtain a rough necessary condition for the transition above as either of the following formulas:

$$H_i(\boldsymbol{x}^0) < F_i + \frac{1}{2}\alpha + (k_r - k_f)\zeta', \tag{5.4a}$$

$$H_i(\boldsymbol{x}^0) > F_i - \frac{1}{2}\alpha - (k_r - k_f)\zeta', \tag{5.4b}$$

where (5.4a) applies to the wavefront of partial $\boldsymbol{e}$ propagating into $\overline{\boldsymbol{e}}$ while (5.4b) applies the other way around, with ζ' (> 0) signifying the approximate level of $|\zeta_i^0|$. By contrast, when a threshold value ζ^* is imposed on ζ_i so that ζ^1 and ζ^0 are fixed at $\zeta^1 = \zeta^0 = \pm\zeta^*$, the relation $(\zeta_i^0 + \eta_i^0)(\zeta_i^1 + \eta_i^1) < 0$ becomes

$$\left(\zeta_i^0 + \eta_i^0\right)\left[\zeta_i^0 + k_f\eta_i^0 + \left(\mathbf{W}\boldsymbol{x}^0\right)_i\right] < 0, \tag{5.5}$$

and it then gives a necessary condition for the output transition as either of the following formulas:

$$H_i(\boldsymbol{x}^0) < F_i + (1 - k_f)\zeta^*, \tag{5.6a}$$

$$H_i(\boldsymbol{x}^0) > F_i - (1 - k_f)\zeta^*, \tag{5.6b}$$

which are the counterparts of (5.4a) and (5.4b), respectively. With the spiral wavefront propagating toward its convex side, a neuron is able to conform its output to the minority

of neurons in its neighborhood, i.e., the neurons on the concave side of the wavefront whose number is less than $\frac{1}{2}|S_i|$. Nevertheless, Eqs. (5.4) and (5.6) indicate that there still exists a minimum requirement for the number of the minority neurons. In particular, Eq. (5.6b) requires a partial pattern $\boldsymbol{e}$ (or $\overline{\boldsymbol{e}}$) containing a minimum of approximately $\frac{1}{2}|S_i|-(1-k_f)\zeta^*$ neurons in S_i for the activation of $\boldsymbol{e}$ (or $\overline{\boldsymbol{e}}$) to propagate and replace $\overline{\boldsymbol{e}}$ (or $\boldsymbol{e}$) at the ith neuron's site, and the value of the threshold, ζ^*, determines this requirement. With a sufficiently small ζ^*, the critical value for $H_i(\boldsymbol{x}^0)$ gets close to $\frac{1}{2}|S_i|$ (as required in the Hopfield network) so that the wave propagation cannot continue in the spiral, especially near the phase singularity where the wavefront has a larger curvature and Eq. (5.6) is more difficult to satisfy. In this way, the constraint of ζ_i has an effect of smoothing those curved wavefronts and the spiral waves can thus be eliminated. A schematic for this explanation is given in Fig. 5.5.

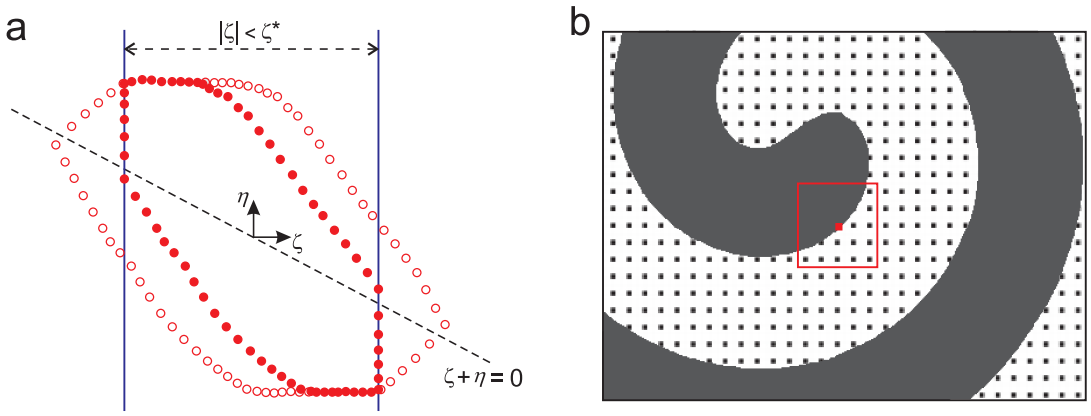

Figure 5.5: Schematics explaining the mechanism of a static PSC for eliminating spiral waves. (a) The excursions of neurons in the ζ–η phase space without and with the limiting threshold ζ^*, where the scatter plots are not real trajectories but only demonstrate the effect of a PSC schematically. (b) A spiral wave rotating anti-clockwise, where the local connection region surrounding a neuron near the wavefront is boxed. The "black" neurons are less than a half of the neurons in this region and the spiral wave may still propagate; however, when ζ^* becomes small enough, the minimum required number of these neurons increases and this propagation cannot be maintained.

The preceding argument reveals that a static phase space constraint as in [32] is already able to eliminate spiral waves; in this study, we hope further to guide the system into a spiral-free state of its original dynamics (4.1) using a DPSC that allows for a quit mechanism for the control. For our purpose, the control signal must be based on detection of the existence and non-existence of spiral waves, which may be achieved by checking for the amplitude reduction. Hence we choose

$$u(t) = \min h_i(t), \tag{5.7}$$

where min takes the minimum of all h_i over the whole network ($i = 1, 2, ..., n$); a small control signal u denotes the existence of spiral waves and a large u indicates the opposite.

Under the current parameter setting, Fig. 5.2 implies that a u value as low as 10 might accompany spiral waves and it might increase to roughly 20 when the spirals are gone.

The next key is to establish negative feedback between the exerted constraint and the network's output, i.e., the constraint should be strengthened with the presence of spiral waves and fade with their extinction, requiring that $\zeta^*(u)$ should be an increasing function of the control signal u. In this study, we truncate the refractory state $\boldsymbol{\zeta}$ such that

$$\zeta^*(t) = c_0 + \exp\left(c_1 + c_2 u\left(t\right)\right), \tag{5.8a}$$

$$\zeta_i(t) \to \pm\zeta^*(t), \text{ if } |\zeta_i(t)| > \zeta^*(t), \tag{5.8b}$$

where c_0, c_1 and c_2 are control parameters, and this is the same form of control exertion as what was used in [52]. By assigning appropriate parameter values, $\zeta^*(u)$ will increase beyond the typical range of the uncontrolled ζ_i after all of the spiral waves disappear and the CNN may converge to an intrinsic non-spiral state while its evolving rule is unaltered. Here we select the control parameters in Eq. (5.8) as $c_0 = 4.0$, $c_1 = -10.0$, and $c_2 = 0.60$ in all subsequent simulations, unless stated otherwise. Another parameter involved in the DPSC module is the decay parameter k_h in Eq. (5.1), which will still be fixed at $k_h = 0.95$. We next demonstrate the performance of the entire control scheme and analyze the network's intra- and post-control dynamics.

5.3 Controlled dynamics under DPSC

In this section, we apply the DPSC scheme designed in the preceding section to the cellular CNN in spiral wave states. We will illustrate the process of directing the network from a spiral wave into a plane wave state by a case study, demonstrate the effectiveness of DPSC and the features of the controlled dynamics from a statistical point of view, and then investigate the parameter dependence of control results and control processes.

5.3.1 Specific control case

Here we work on the specific example described in Sec. 5.1.1 to show how the spiral waves are eliminated by the DPSC. To provide a complete overview, Fig. 5.6 shows the control process as the time series for the control signal $u(t)$ compared with the case using no control. We discarded the data before $t = 200$ to avoid considering the transient stage when $h_i(t)$, $u(t)$ and the output $\boldsymbol{x}$ had yet to settle. Subsequently, $u(t)$ became steady and remained at around 10 for hundreds of steps, but it also never exceeded 12 for at least 10^4 steps in the uncontrolled case (see Fig. 5.6(a) and the insets), thereby indicating persistent spiral wave activity. By contrast, Fig. 5.6(b) shows that $u(t)$ tended to increase after the control was initiated at $t = 301$, before declining prior to $t = 400$, and reaching a high value of approximately 21.8. In addition, the proportion of neurons affected directly by the time-varying limit $\zeta^*\left(t\right)$ in the network was $80 \sim 90\%$ after the start of control,

but it declined sharply after $t = 400$, and finally fixed at zero after several weak bounces. According to these results, we can infer that the spiral waves were removed successfully and that the network was converted into an intrinsic non-spiral state, which was actually a PW state as we will show later. The duration of control was 170 steps and its last effect was observed at $t = 470$, where the average proportion of neurons affected during this period was 0.596 with a standard deviation (SD) of 0.377.

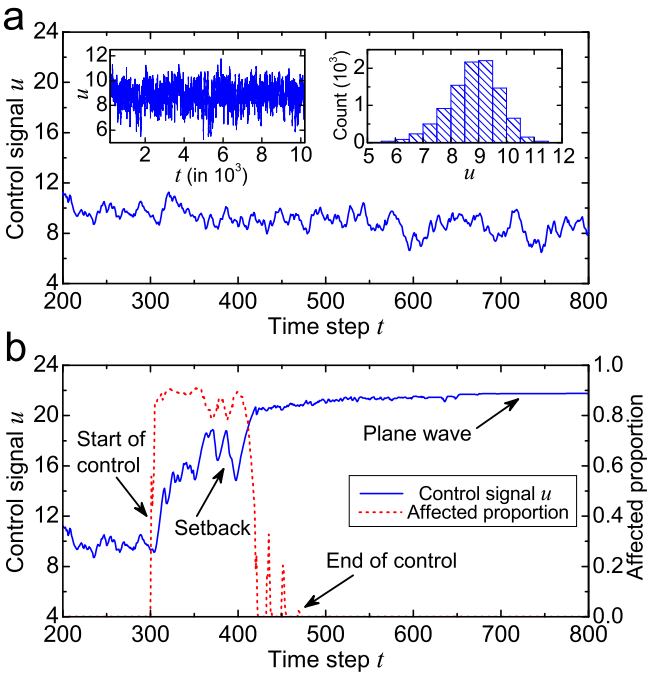

Figure 5.6: The specific control process is illustrated based on the evolution of the control signal compared with the uncontrolled case. (a) $u(t)$ in the uncontrolled CNN. The long-term evolution over 10^4 time steps and the corresponding histogram for $u(t)$ are shown in the insets. (b) The evolution of $u(t)$ with control initiated at $t = 301$. The proportion of constrained neurons is also plotted to show the automatic ending of the DPSC.

As the most straightforward way of understanding the control process, the output sequences extracted at different stages are shown in Fig. 5.6. When the control started, the spirals stopped rotating and they underwent gradual deformation as an apparent extension of the previous clustering process, before yielding a propagating cluster. Next, this cluster continued to move downward where its two ends reached out and started to curl, which is a well accepted mechanism for generating spiral waves in an excitatory medium. However, these processes were obstructed by DPSC and recorded only as the setback in Fig. 5.6(b), before the two ends of the cluster collided to yield an antecedent of the PW. As time passed, the undulating shape of the wavefronts flattened progressively and the CNN finally converged to an ideal PW state with equal numbers of neurons to output $x_i^* = 1$ and $x_i^* = 0$. The wave speed was two pixels per step and examinations of all the internal state variables confirmed that the system had an exact period of 25 steps after control.

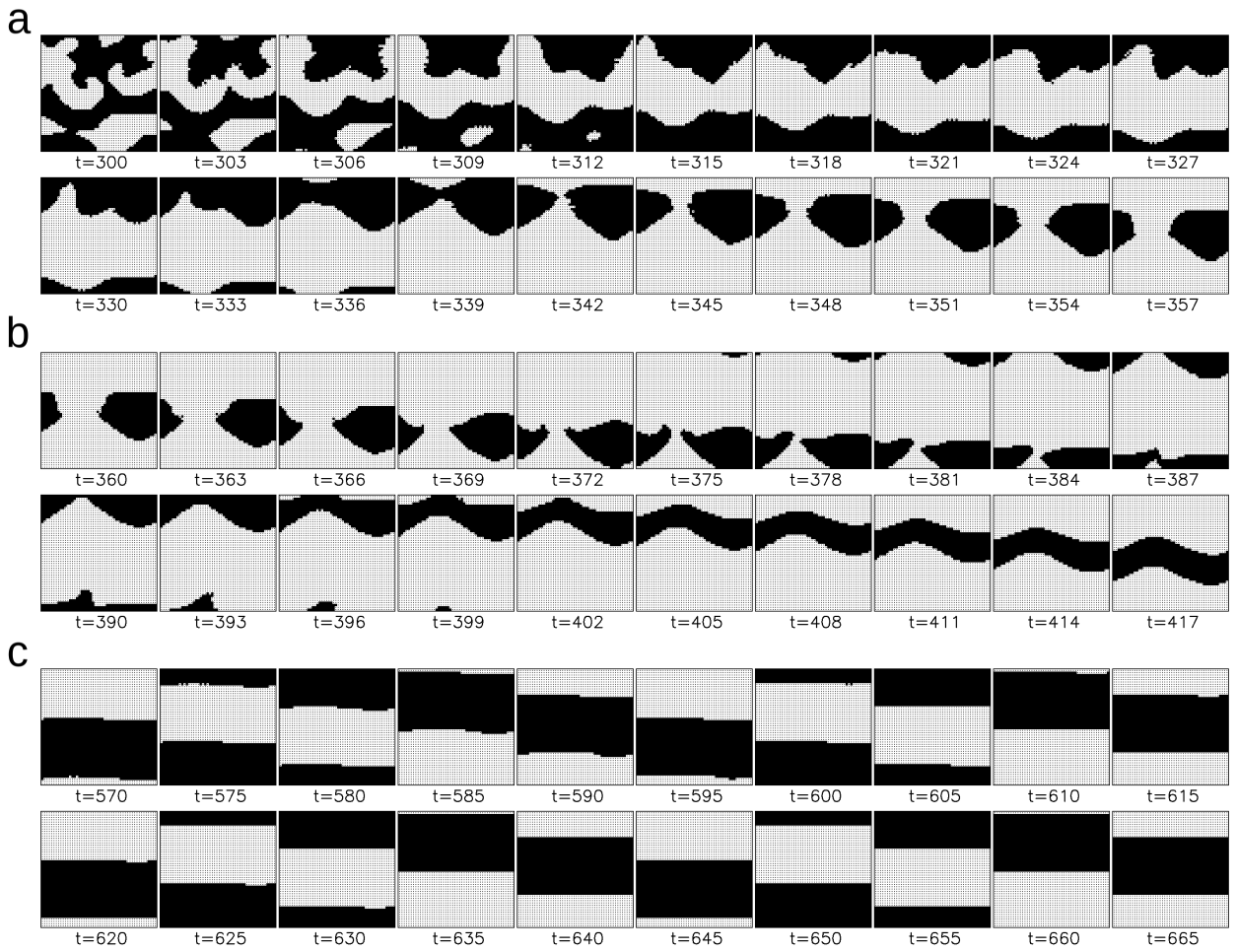

Figure 5.7: Output sequence segments from the network with control initiated at $t = 301$. (a) The spirals stopped rotating and a moving cluster appeared. (b) The cluster evolved into an incipient PW instead of spiral waves reappearing. (c) Ideal PW patterns were formed after the edges flattened. The output is displayed once every three steps in (a) and (b), and every five steps in (c).

The image sequence described above emphasizes the digitized spatial patterns due to saturated outputs, but we now consider the internal oscillation of certain individual neurons. Figure 5.8 shows the time series of $y_i(t) = \zeta_i(t) + \eta_i(t)$ for the 1020th neuron and 2270th neuron, which were located near and away from a singularity, respectively. Before control, $y_{1020}(t)$ exhibited amplitude reduction compared with $y_{2270}(t)$, whereas during control, $y_{1020}(t)$ and $y_{2270}(t)$ adjusted themselves with hampered and slowed oscillations, occasionally with almost identical or opposite values when both were subject to the threshold $\zeta^*(t)$. After the end of control, $y_{1020}(t)$ and $y_{2270}(t)$ finally achieved a period-25 oscillation with a common phase and amplitude. Given that these two neurons represented different binary values in the basal pattern, then $y_{1020}(t)$ and $y_{2270}(t)$ actually had opposite phases in the wave of activated memory, which agrees with the fact that these two neurons were spatially separated by half a wavelength in the direction of wave propagation.

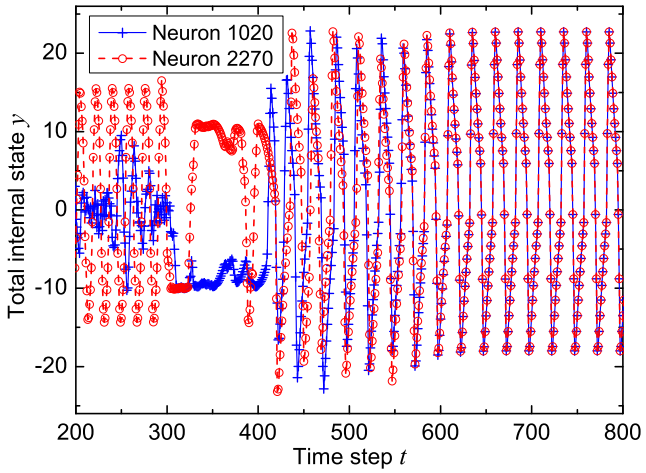

Figure 5.8: Oscillation of the total internal state before, during, and after control for two representative neurons.

5.3.2 Statistical investigation of controlled dynamics

After capturing some basic features of our controlled model in the case study described above, we considered the following issues: the success rate of spiral wave elimination using DPSC and the control results that can be obtained; and, if various control results can be obtained, whether the corresponding control processes have distinct properties.

A subsequent simulation of the system in the 4991 cases mentioned in Sec. 5.1.3 with DPSC initiated at $t = 301$ demonstrated the high success rate of spiral wave elimination and multiple possible control results. In all 4991 cases with persistent spiral waves, the CNN was directed to one of its intrinsic non-spiral periodic states in less than 10^4 steps, where the DPSC terminated automatically. These states could be classified into two categories, each with three different observed periods, and their frequencies are listed in Table 5.1. In 77.8% of the trials, the CNN was controlled to an SO with a period of 63,

126, or 188, whereas in the other trials, the network fell into an orbit of PW, with a period of 25, 49, or 98. Within each category, we also observed an approximate multiple-aliquot relationship among the period lengths where the states of the shortest period appeared most frequently.

Table 5.1: Frequencies of different types of control results.

Type	Period	Count (Rate)	Total
SO	$T = 63$	3586 (71.8%)	3883 (77.8%)
	$T = 126$	100 (2.00%)	
	$T = 188$	197 (3.95%)	
PW	$T = 25$	993 (19.9%)	1108 (22.2%)
	$T = 49$	101 (2.02%)	
	$T = 98$	14 (0.281%)	

Further information about the control-induced states is summarized briefly in Fig. 5.9 in terms of the schematic output sequences and grand mean power spectra of the total internal state $y_i(t)$. The spatiotemporal output of the period-25 PW states shifted downward (equivalently, upward, leftward, or rightward) and the relevant power spectra were isolated lines at multiples of the dominant frequency $f_d = 0.0400$. For the PW states of period 49 and 98, the wave propagated at an oblique angle of 45°, while the dominant frequency was kept at $f_d = 0.0408$ ($T_a = 24.5$), so a neuron circled two or four times in the ζ–η plane during an exact period of the network. In addition, the SO states exhibited few wave characteristics other than synchronization of all the neurons and oscillation of the entire network between complete $\boldsymbol{e}$ and $\overline{\boldsymbol{e}}$ in its spatiotemporal output. The basic cycle of the oscillation was $T_a = 31.5$ or 31.3 steps ($f_d = 0.0317$ or 0.0319), and the period-63, 126, and 188 orbits comprised two, four, and six cycles, respectively. Moreover, states in the same period were not necessarily equivalent, e.g., period-25 PW states were identified with 24 or 26 rows of neurons to output $x_i^* = 1$, in addition to those with 25 rows. These analyses of the pre- and post-control dynamics demonstrated the signature frequencies of different types of states, i.e., $f_d \approx 0.057$ for a spiral wave, 0.040 for PW, and 0.032 for SO, which are reminiscent of the frequency modulation in the rodent visual cortex [39].

In the rest of this subsection, we concentrate on the control process, especially the statistical differences between the processes leading to PW and those leading to SO. In the time domain, we consider quantities including the duration of control, the mean and SD of the affected neuron proportion during control, and the product of the first two as a measure of the total amount of control. The results of our trials in the plane spanned by the average affected proportion and the duration of control on a logarithmic scale are plotted in Fig. 5.10(a), together with a mean–SD plot of the affected proportion in the inset. Clearly, the PW-inducing control processes were more spread and they generally had longer durations (several hundred steps) than the SO-inducing control processes (a

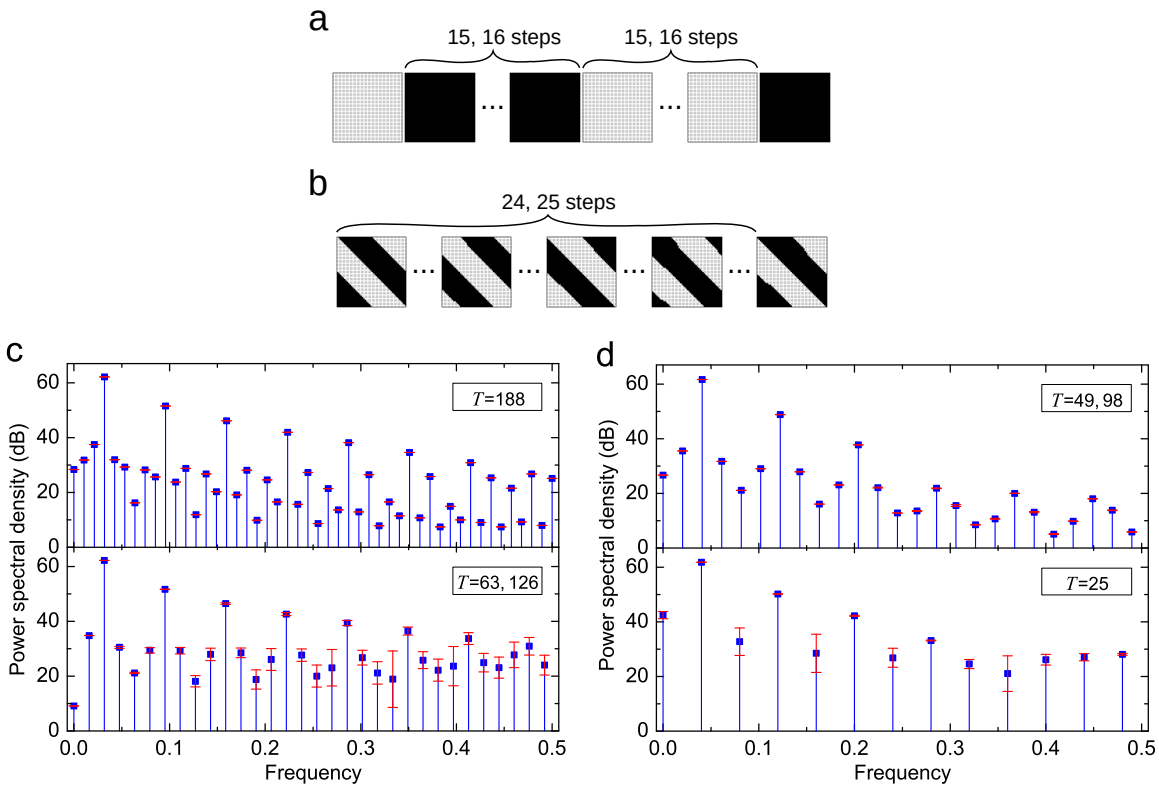

Figure 5.9: Dynamics of the post-control periodic states. Schematic output sequences are shown for the basic cycles of (a) the SO states and (b) the PW states of period-49 and 98, as well as the grand mean power spectra of $y_i(t)$ for (c) the SO states and (d) the PW states. In (c) and (d), the spectral density values are specified according to a frequency interval of 10^{-4}, where the error bars indicate the SD among trials with the same type of control result.

few dozen), and this situation was similar to the amount of control. However, according to the data points distributed to the left of those for SO, the PW-inducing processes had smaller mean proportions of affected neurons, where a smaller mean also corresponded to a larger SD. The bounces in the control before its disappearance, as shown in Fig. 5.6, were responsible for the small mean and large SD of the affected proportion of neurons.

In the frequency domain, the grand mean power spectra of $y_i(t)$ differed during the PW- and SO-inducing control processes from those before or after control as well as from each other, as shown in Fig. 5.10(b). Compared with the pre- and post-control dynamics, the range of lower frequencies made the main contribution to the intra-control dynamics, which supports the evidence for gradual adjustment during control obtained from the case study described in Section 5.3.1. In addition, when the spectral density of the SO-inducing processes decayed monotonically with an increasing frequency, its counterpart for PW exhibited several peaks, which may also have originated from the almost controlled oscillation during the late stage of control when the bounces occurred.

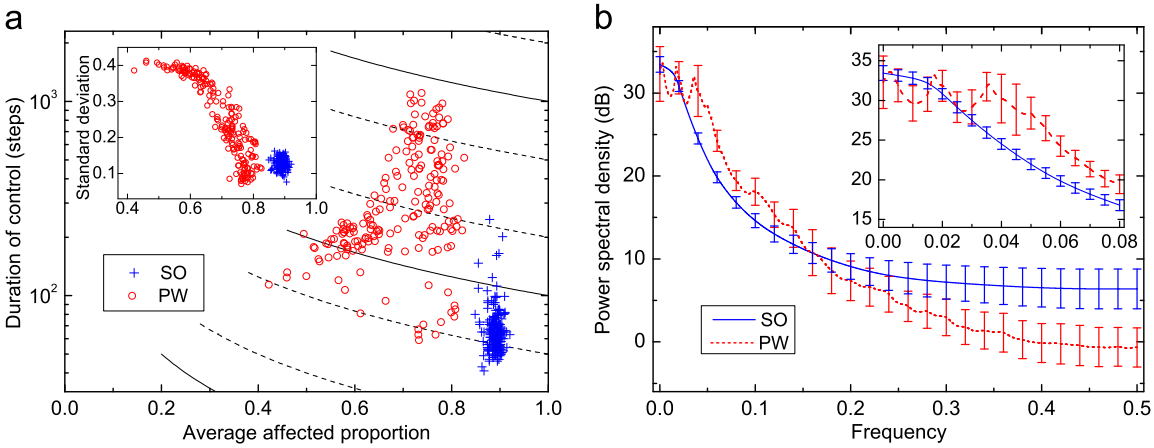

Figure 5.10: Statistical analysis of the intra-control dynamics. (a) Plots of the duration of control and the SD of the affected proportion versus the average affected proportion. Isolines of the total control amount are drawn in the former plot, where their iso-values are readable from the right edge. For clarity, 200 data points are shown for SO and for PW in both plots. (b) The grand mean power spectra for $y_i(t)$ during SO- and PW-inducing control processes. The error bars represent the SD among the mean power spectra of the same type, which were interpolated to obtain their values at a common frequency.

5.3.3 Control parameter dependence

The performance of the proposed DPSC method was also examined with other control parameter values and this subsection provides a brief description of the dependence of the control results and processes on the parameter c_2. We found that spiral waves were almost always eliminated for the investigated values of c_2, but the control results varied greatly, as illustrated in Fig. 5.11. We categorized the control result according to the following features: (i) whether it was free, i.e., whether the constraint vanished; (ii) whether it was SO or propagation, where the latter was not only PW because we could not exclude the possibility of propagating clusters or other patterns without plane edges, especially when the network was not free; (iii) whether it had the shortest exact period, i.e., 63 for SO or 25 for propagation. For $0.550 \lesssim c_2 \lesssim 0.565$, most of the control trials ended with free SO states and only the remaining 3% led to non-free propagation. For even smaller c_2 values, non-free SO states could also appear. By contrast, when $c_2 \gtrsim 0.570$, the propagation states were free PW states after control, where the percentage increased with c_2 and reached 32.9% when $c_2 = 0.630$. In addition, a larger c_2 value, which indicated a weaker overall constraint, made it more likely for the post-control network to have longer periods. Thus, for SO, the period-126 and period-188 states continued to approach the share of the period-63 states, and for PW, states emerged with various long periods, some of which reached up to several thousand steps, or with no period found within 10^4 steps and they became increasingly frequent, especially when $c_2 > 0.610$.

In addition to the partial selectivity of the control results, the variations in the parameter c_2 also modulated the control processes. Figure 5.12 plots the results of control

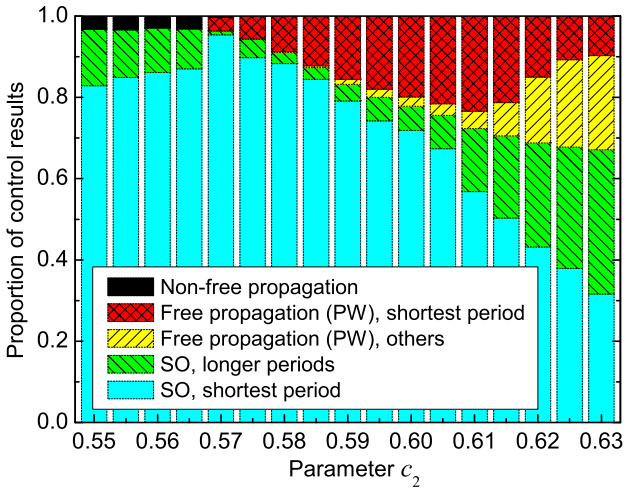

Figure 5.11: Proportions of different types of control results as functions of the control parameter c_2.

processes conducted at different values of c_2, which are characterized as the average affected proportion on the horizontal axis, the duration of control on the vertical axis, and their product, i.e., the cumulative affected proportion, on the isolines. Increases in c_2 only caused a slight displacement of the ensemble of SO-inducing processes in the plot, thereby suggesting that there were small decreases in all three quantities, whereas they caused fairly dramatic changes in the scatter of the PW-inducing processes. When $c_2 = 0.570$, most of the PW-inducing processes lasted longer but much lower average proportions were affected, and thus the cumulative affected proportions were almost equal compared with the SO-inducing processes. When $c_2 = 0.580$, another cluster emerged in the region that represented higher cumulative affected proportions, which was roughly divided from the existing one by the isoline at a value of 1×10^2. Further increases in c_2 caused continuous shifts in most of the PW-inducing processes toward a larger total amount of control, and when $c_2 = 0.620$, there was a distinct distribution from the beginning, which was relatively concentrated in terms of the average affected proportion but dispersed in terms of the control duration.

5.4 Discussion

Our method for removing spiral waves from a locally connected CNN using a DPSC has extended the possible applications of this method, which was originally implemented in a fully connected associative CNN to trap its memory retrieval in a periodic orbit [52]. Analogies and differences can be observed by comparing the previous study with the present one. When designing the control signal as a task-specific indicator of the network's state, the magnitude $|\eta_i|$ always has a core role and it is exploited well due to the effect of the weight matrix $\mathbf{W}$ on the output $\boldsymbol{x}$ and the dominance of $\mathbf{W}\boldsymbol{x}$ in the feedback internal state $\boldsymbol{\eta}$. In the previous study, the CNN's departure from or its approach to the

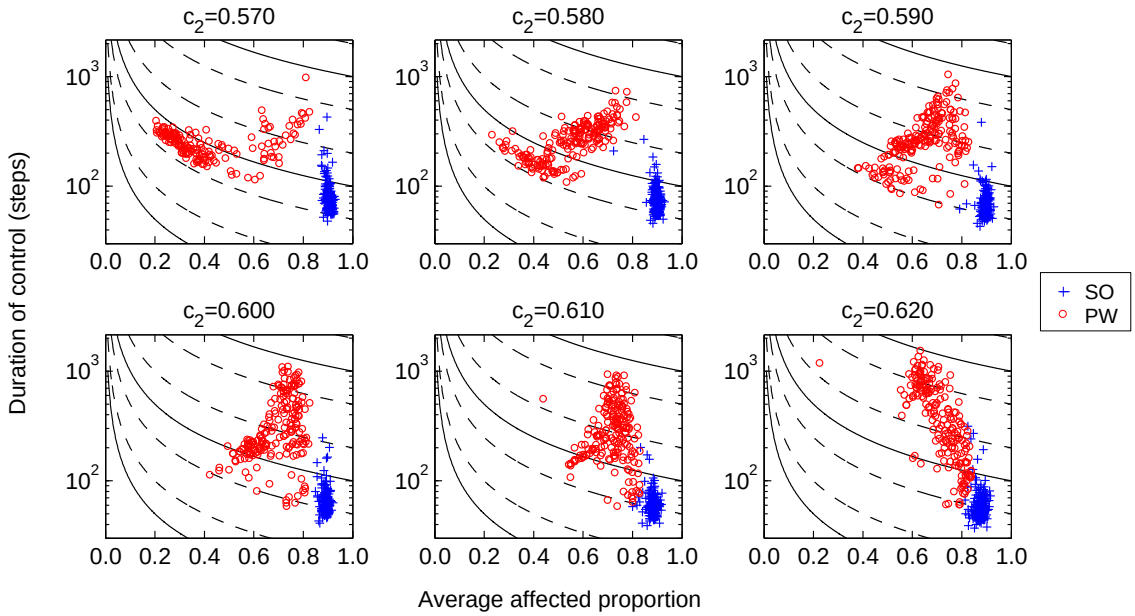

Figure 5.12: Modulation of the control processes by varying the control parameter c_2. For both SO and PW, 200 data points are presented in each plot for clarity.

basal patterns at step $t-1$ were reflected by its small or large control signal at step t, followed by tighter or looser control at step $t+1$, respectively. However, in the current study, the amplitude reduction had to be detected by a temporal moving average, so the control signal and dynamic constraint increased and decreased at a far slower rate in response to the extinction and emergence of spiral waves. Therefore, the intra-control dynamics of the network during spiral wave elimination had a quite different low-frequency feature compared with the previous study. To exert control, limiting the refractory states prevented certain neurons from crossing the line $\zeta+\eta=0$ in the ζ–η plane, which hindered the CNN's itinerancy or evolution where such crossings were indispensable. In the previous study, the transition to other basal patterns was stopped and the CNN was kept in situ, whereas in the present study, spiral rotations were terminated and clustering progressed instead. Importantly, the CNN in [52] could not settle in a stored pattern, so the dynamic constraint never ceased and it became an integrated part of the variant associative CNN model. By contrast, free SO and PW were permitted states in the locally connected CNN, so the DPSC disappeared automatically without altering the network model when these states were reached.

A partially or locally connected CNN could encode the same patterns (or other information) as a fully connected CNN but it would use significantly fewer synapses, which is advantageous for its hardware implementation and numerical simulation. This is even clearer when we consider large-scale networks, e.g., the CNN described in [66] stored color images with more than 10^6 neurons and each neuron received inputs from just a few hundred. In addition, the full auto-associative weight matrix sometimes tends to reduce the

dimension of the feedback internal state, so a partially connected CNN may actually have a higher dimension and richer dynamics. Traveling waves of patterned activity arise from local connections and they provide a novel mechanism of association as propagating alterations of cell assemblies, rather than the conventional global state transition. To facilitate the use of these networks in associative memory and other areas, the DPSC and other appropriate control methods are needed to regulate the network's complex behavior. In this study, we focused on a highly simplified, symmetric case with a single checkerboard memory, which formed an associative CNN, but mathematically it amounts to a nonlinear oscillator network with local excitatory connections. Generalizing the proposed DPSC method to multiple stored patterns and the corresponding associative dynamics should be considered in future research.

As previously mentioned, spiral waves are modeled by diverse spatially extended dynamical systems that are categorized according to their discreteness or continuity in time, space and state variables, which include cellular automata, discrete-time and continuous-time neural networks, and partial differential equations. In the present study, the DPSC control of spiral waves is implemented in a discrete-time CNN, but it can also be realized in a continuous-time neural network, where the smoothing effect discussed in Section 5.2.2 works in a sense of time integration; that is, the limiting threshold prevents the neurons from receiving adequate input during a certain time interval to change its state in the wavefront of large curvatures, so the wave near the singularity is slowed down and the spiral is hence smoothed. Besides, the cyclic motion of the neurons in the CNN in wave propagation consists of alternating slow and fast processes, and their dynamics can be demonstrated to be similar to coupled van der Pol oscillators or FitzHugh–Nagumo neurons. This implies the possibility of applying the DPSC scheme to more general oscillatory and excitable media expressed by neural networks and even by partial differential equations, since a certain difference stencil for the Laplace operator in the numerical solution of reaction-diffusion equations is just equivalent to some local connection scheme in the neural network model. Such a generality is partially verified by the spiral wave suppression using phase space constraint in coupled Chua circuits [96] and modified FitzHugh–Nagumo systems [58], except for the use of fixed threshold values rather than dynamic ones. Although the constraint therein was intermittent and concurrent with the threshold exceeding at some sampled site, no exact feedback mechanism existed between the evolution of spirals and the progression of control, and the system was controlled only to a homogeneous state. On the contrary, with a well devised control signal, our proposed DPSC scheme might help to find additional propagation modes and accomplish more flexible control results after eliminating spiral waves in other spatially extended dynamical systems.

Despite some simplification in the details, the simulation of the cellular CNN reproduced certain aspects of the spiral wave dynamics found in the mammalian neocortex [39]. The experimental study showed that the spiral waves generally corresponded to a higher oscillation frequency than PWs or other patterns in the same cortical region, which is

called the frequency modulation effect. In the present model, the characteristic frequencies of spiral wave, PW, and SO states had a similar relationship, probably because of shortcut excursions in the phase plane when the neurons are organized by spiral waves. Moreover, the pairing of spiral waves with opposite rotating directions was observed frequently during experimental sleep-like states [39], where the delta-dominant state is more favorable for the occurrence of spirals than the theta-dominant state because the former is influenced less by subcortical rhythms. In our simulation, these pairings were almost certain when the spiral waves were sustained stably without control because the equiphase curve for a phase value starting from a phase singularity had to end at another. It is considered that the in vivo control of spiral waves in the cortex is due to long-range and nonlocal connections, such as thalamocortical and corticocortical connections, and thus clarifying these control mechanisms and using appropriate neuron models would produce more biologically realistic simulations. In addition, there have been many reports and analyses of traveling waves in the nervous system, but their functional roles are not well understood. The possible functions of traveling wave dynamics could also be explored in the future using cellular CNNs and relevant control methods as a platform.

In this chapter, the spiral wave dynamics in the cellular CNN have been investigated with an emphasis on its control. The amplitude reduction phenomenon is demonstrated as a hallmark of spiral waves, and the amplitude-reduced feedback internal states are used to construct a control signal; the control signal then modulates a limiting threshold to constrain the refractory internal states. Such a DPSC scheme successfully eliminates the chaotic spiral waves and redirects the network into its intrinsic PW or SO states. The pre-, intra-, and post-control dynamics are compared, which feature different characteristics in the frequency domain. The PW-inducing and SO-inducing control processes are distinct, where the former generally had longer durations but smaller average proportions of affected neurons in the network. The study of parameter dependence indicates a partial selectivity between controlling to PW and SO, where the control processes are modulated as well. The simulation phenomenologically reproduces a few aspects of the experimentally observed spiral wave dynamics in the mammalian cortex such as the frequency modulation. This study also expands the applicability of DPSC in controlling CNNs, facilitating the future application of cellular CNNs in associative memory.

Chapter 6

Epilogue: Conclusions and Prospects

The idea of using the evolution of dynamical systems to solve problems naturally has been of interest to people and implemented in various ways in recent years. A fresh, interesting and yet important example is the solution of Sudokus as boolean satisfiability problems using the transient chaos of designed dynamical systems [16]. Looking back to the history, we may find that the idea of using dynamics for problem-solving can date back at least to the invention of the Hopfield neural network: it evolves to an attractor that corresponds to the local minimum of an energy function, and is thus used for associative memory or classification into memory patterns that have been stored as attractors.

The introduction of chaotic dynamics into Hopfield-like neural networks, as with the associative CNNs, has reshaped their associative dynamics [1]. The memory retrieval is no longer a converging process but an ever-changing, non-stop one, where the output jumps from one stored pattern to another in a seemingly random way: This is just the traditional regime, global transition, for chaotic memory retrieval. Several CNN-based models have been developed [34, 35, 52], which obtained controlled periodic associative dynamics that share some similarity with the chaotic–periodic transition in rabbit's olfactory system [86].

In recent research, restriction of the synaptic weights to a local region of each neuron has provided a new perspective for the chaotic memory retrieval [66, 67]. The transition among stored patterns is no longer a global transition, but a sequential local one that has a spatial phase structure. Such a wave-like new regime of memory retrieval is advantageous for its implementation on large-scale networks with a highly reduced number of connections, and it also reflects the feature of strong local synaptic connections in a real brain. People may be interested in how the propagating waves of patterns can be utilized for applications and how this may help in understanding the information processing in the brain, where traveling waves are also increasingly observed and studied [39, 90, 104].

Further development of the existent model sometimes requires knowledge of the fundamental properties including those of the wave dynamics. We may expect to develop an associative network model where a local input can be classified and the information can

then be transmitted to another specific site by inducing a directional traveling wave; this actually requires a fairly high extent of free manipulation of the wave dynamics. In this case, if we hope to control the dynamics of the network (for example, spiral wave) to some plane wave state via a certain method (for example, parameter modulation), we should at least know with what parameters the expected plane wave dynamics can exist. This triggers the investigation of the wave dynamics of a cellular CNN, especially the dynamics in the parameter space. On the other hand, the construction of feasible control scheme for the wave dynamics is also needed in creating such models; the existent studies on the control of the spatiotemporal pattern formation (including chaos) naturally reminded people of the possibility of generalizing them for the current scenario.

Hence this thesis attempts to cast some light upon the wave dynamics in the cellular CNN under the background of the wave-like association regime as well as the traveling brain waves. The wave dynamics is a big topic that is related to almost every aspect of the theory and application of dynamical systems. Accordingly, this thesis not only deals with the wave dynamics itself but also involves the study of bifurcation and chaos control. Summarizing the results that we acquired, the following conclusions can be drawn.

- The neural field model corresponding to the cellular CNN accommodates abundant traveling wave dynamics. Although it can be deemed simply as a variant reaction-diffusion system with singular spatial coupling, various traveling waves are possible even in only one spatial dimension. Periodic waves exist for all speeds, and fold of periodic waves appears frequently. Periodic waves may have symmetric shapes, or only oscillate around a nontrivial equilibria. The periodic waves can end with pulses (solitary waves) or end with single fronts/backs.

- Bifurcations of higher codimensions turn out to be useful in the analysis of the plane waves. The network or field model itself depends on parameters, and the traveling wave coordinate introduces an additional parameter, the wave speed. The analysis of high-codimensional bifurcations clearly reveals the existence and fate of the wave solutions in the parameter space. In this study, the analytical computation of the parameter-dependent normal form of the BT bifurcation produces a bifurcation diagram as a function of the wave speed, providing important information on the wave solutions in a condensed way.

- Despite its simplification, the cellular CNN produces spiral wave dynamics that is to some extent similar to the observed cortical spiral waves. Some natural examples include the pairing of two spirals rotating in opposite directions and the amplitude reduction near the phase singularity. The spiral wave has a higher frequency than the plane wave in the same environment in the cortex, which is called “frequency modulation”; this effect is also reproduced. There is a more subtle similarity in the enhanced drift and termination of spiral waves with the presence of control. These

may imply the universality of the observed cortical spiral dynamics in oscillatory media and the possibility of using simple models to realize their functionality (if we know it).

- The applicability of DPSC as a control method is expanded. The DPSC proposed here not only synchronizes the network but also transforms spiral wave states into plane wave states; the DPSC here works with negative feedback and ceases automatically, leaving the CNN unaltered. These are different features that separate it from other existing methods for eliminating spirals. On the other hand, as the DPSC has been applied to fully connected associative CNNs, we believe that the DPSC family is advantageous in realizing the manipulation of the associative dynamics of CNNs.

After the summary above, some prospective advances of the current study are discussed at the end of the thesis.

- The bifurcation analysis of the traveling wave system is not completed yet. The two singularities on the BT bifurcation curve indicate codimension-three bifurcations, where additional bifurcation curves may emanate and partition the parameter space; another codimension-two bifurcation in the system, the zero–Hopf bifurcation, is not clarified, which may involve tori and other complex wave behavior. Further analysis of these bifurcations would yield more specific and comprehensive conclusions about the wave dynamics.

- The cellular CNN considered in this thesis is highly simplified and symmetric. The bias of the neurons in the CNN may be deviated from the present setting, so that the network dynamics cannot be reduced to be homogeneous; there may be multiple stored patterns, so that the spatial coupling may have more complicated forms; the synaptic footprint may have a distinct profile, so that the corresponding neural field model is also different. In that case, the present result and method should be revised or generalized, and resultant new characteristics remain to be discovered.

- The control of the traveling wave dynamics in the cellular CNN needs to be further developed. The present DPSC control realizes the conversion of spiral wave states to non-spiral states; however, the conversion the other way around is not considered. The present DPSC demonstrates a dependence of the control results on the control parameter in a statistical sense, but the control target cannot be designated during a certain run. In addition, as scroll waves may appear in a three-dimensional medium, we are interested in whether and how the DPSC can be used to control scroll waves. Moreover, the generalization of the current scheme to associative memory of multiple patterns remains to be considered.

There is still a long way to go, before we can freely manipulate the various wave dynamics in the network and use it for real-world applications. This is not the end but the beginning.

Related Publications

1. Yang Li, Makito Oku, Guoguang He, and Kazuyuki Aihara. *Elimination of spiral waves in a locally connected chaotic neural network by a dynamic phase space constraint*, Neural Networks, **88** (2017), 9–21. doi: 10.1016/j.neunet.2017.01.002. [1]

2. Yang Li, Hiroshi Kokubu, and Kazuyuki Aihara. *Explicit transversality conditions and local bifurcation diagrams for Bogdanov–Takens bifurcations on center manifolds*, under review in Physica D: Nonlinear Phenomena. [2]

[1] This is the formal published journal article whose contents cover Sec. 4.1.1 and Chapter 5 of this thesis.
[2] The contents of this paper correspond to Chapter 3 as well as Appendix A of this thesis.

Acknowledgments

This thesis would have never materialized without the help, support, and encouragement from many people, toward whom I would like to extend my sincere gratitude. First and foremost, I heartily appreciate the long-lasting and invaluable guidance and support from my supervisor, Prof. Kazuyuki Aihara. He provided a highly indulging environment where I was able to freely propel the research, yet he is consistently present to help when there is any problem. His wealth of knowledge, rigorous attitude to science, and diligence in work has also educated me and made him the role model that I am always indebted to.

I would like to thank Prof. Yoko Yamaguchi, Prof. Takayasu Matsuo, Prof. Gouhei Tanaka, and Prof. Hiromichi Nagao for their kind participation in the examination committee in their busy schedules. Their comments and opinions helped to improve the current thesis and inspire new ideas for my future research as well.

I am deeply thankful to Prof. Hiroshi Kokubu in Kyoto University. I am honored that I had an opportunity to discuss pleasantly with him when he clarified my confusions so that I could complete the third chapter. I would like to thank Prof. Motomasa Komuro, who spent time considering my question, discussing with me, and giving me instructions on the numerical continuation of bifurcations.

I feel lucky to have spent more than three years in the Laboratories for Mathematics, Lifesciences, and Informatics, where the professors, researchers, staff, and students were all creating a comfortable atmosphere for study. Specifically, I am obliged to Dr. Makito Oku, who has contributed a lot to our lab and helped me in every aspect; I am beholden to Dr. Kai Morino, Dr. Fang Duan, Dr. Masashi Kajita, and Dr. Muyuan Xu, who have been offering me much valuable advice and sharing with me much useful knowledge; my enjoyment of the time here has also been owing to the goodness of many members in the big lab, including Ryota Mori, Yoshitaka Haribara, Zhiqiang Tong, Hiromasa Sakaguchi, Hideyuki Miyahara, Yaxuan Mao and others. Besides, the support and cooperation offered by the secretary group have been indispensable and will not be forgotten.

I acknowledge the support and convenience rendered by the staff of the department administration office and the Office of International Relations, as an international student.

I acknowledge the financial support from the Ministry of Education, Culture, Sports, Science and Technology (MEXT) of Japan and the coordination from China Scholarship Council. It is a pleasure to have the opportunity of furthering my studies and pursuing my doctoral degree with the MEXT scholarship.

At this point, some important scenes and moments during the past few years occur to me. I remember when Prof. Guoguang He became my undergraduate advisor, the very person that inspired my initial interest in chaotic dynamics and recommended me to the Aihara lab; I remember the moment when I applied for the MEXT scholarship with other applicants and the time when we studied together in Changchun. We have been working in separate places all over Japan, and may everything go well and every dream come true for all of us.

Words are never adequate to express my gratitude to my beloved family. I cannot be too thankful to my darling Yanlin Gao, a lovely lady who married me, accompanied me, comforted me, and helped me with my life in spite of her own busy schedules of study. I am deeply grateful to all my family in my small, quiet hometown of Jincheng, Shanxi, and being thousands of miles away does not attenuate my feeling of their selfless care, unyielding support, and profound love. In particular, I am fortunate and proud to have a great mother, Mrs. Hualing Su, who has sacrificed so much for her children without regret. I would quote an ancient Chinese poem[1] to deliver my thoughts for her, as I did twenty years ago as a primary school pupil,

The thread in hand a mother weaves,
    And her boy's garment is thus made.
She sews and sews before he leaves,
    For fear he'd be homeward delayed.
Could the kindness a grass receives
    From the spring sun be clean repaid?[2]

Yang Li
November 20, 2017

[1] A household poem originally entitled *Yóuzǐ Yín* by Meng Jiao (also Meng Chiao, 751–814AD) in the Tang dynasty. It is known more as *The Song of a Wandering Son* literally, or simply *A Traveller's Song* or *Wanderer's Song* in English translation.

[2] This version of translation is entitled *Song of the Parting Son*, due to Shunfa Cao, *Towards beauty in form: tidbits on Chinese–English translation of ancient poetry*, National Defense Industry Press, Beijing, 2007 (in Chinese).

Bibliography

[1] M. Adachi and K. Aihara, *Associative dynamics in a chaotic neural network*, Neural Networks **10** (1997), 83–98.

[2] K. Aihara, T. Takabe, and M. Toyoda, *Chaotic neural networks*, Physics Letters A **144** (1990), 333–340.

[3] K. Aihara, T. Yamada, and M. Oku, *Chaotic neural networks and beyond*, Chaos, CNN, Memristors and Beyond: A Festschrift for Leon Chua (Singapore) (A. Adamatzky and G. Chen, eds.), World Scientific, Singapore, 2013, pp. 259–270.

[4] A. Algaba, E. Freire, E. Gamero, and A. J. Rodríguez-Luis, *On the Takens-Bogdanov bifurcation in the Chua's equation*, IEICE Transactions on Fundamentals of Electronics, Communications and Computer Sciences **E82-A** (1999), 1722–1728.

[5] S. Amari, *Dynamics of pattern formation in lateral-inhibition type neural fields*, Biological Cybernetics **27** (1977), 77–87.

[6] K. M. Aquino, M. M. Schira, P. A. Robinson, P. M. Drysdale, and M. Breakspear, *Hemodynamic traveling waves in human visual cortex*, PLoS Computational Biology **8** (2012), e1002435.

[7] V. I. Arnold, *Ordinary differential equations*, The MIT Press, Cambridge, MA, 1980, Translated by Silverman, Richard A.

[8] W. M. Bement, M. Leda, A. M. Moe, A. M. Kita, M. E. Larson, A. E. Golding, C. Pfeuti, K.-C. Su, A. L. Miller, A. B. Goryachev, and G. von Dassow, *Activator-inhibitor coupling between rho signalling and actin assembly makes the cell cortex an excitable medium*, Nature Cell Biology **17** (2015), 1471–1483.

[9] F. Berezovskaya and G. Karev, *Bifurcation approach to analysis of travelling waves in some taxis–cross-diffusion models*, Mathematical Modelling of Natural Phenomena **8** (2013), 133–153.

[10] W.-J. Beyn, A. Champneys, E. Doedel, W. Govaerts, Yu. A. Kuznetsov, and B. Sandstede, *Numerical continuation, and computation of normal forms*, Handbook of Dynamical Systems (Amsterdam) (B. Fiedler, ed.), vol. II, Elsevier, Amsterdam, 2002, pp. 149–219.

[11] T. W. Carr and T. Erneux, *Hopf bifurcation of the class-b multimode laser*, Physical Review A **50** (1994), 724–731.

[12] F. A. Carrillo, F. Verduzco, and J. Delgado, *Analysis of the Takens–Bogdanov bifurcation on m-parameterized vector fields*, International Journal of Bifurcation and Chaos **20** (2010), 995–1005.

[13] A. R. Champneys, V. Kirk, E. Knobloch, B. E. Oldeman, and J. Sneyd, *When Shilnikov meets Hopf in excitable systems*, SIAM Journal of Applied Dynamical Systems **6** (2007), 663–693.

[14] S. Coombes, *Waves, bumps, and patterns in neural field theories*, Biological Cybernetics **93** (2005), 91–108.

[15] M. Courbage, *On the abundance of traveling waves in 1D infinite cellular automata*, Physica D: Nonlinear Phenomena **103** (1997), 133–144.

[16] M. Ercsey-Ravasz and Z. Toroczkai, *The chaos within sudoku*, Scientific Reports **2** (2012), 725.

[17] B. Ermentrout, *Neural networks as spatio-temporal pattern-forming systems*, Reports on Progress in Physics **61** (1998), 353–430.

[18] W. J. Freeman, *Hilbert transform for brain waves*, Scholarpedia **2** (2007), no. 1, 1338.

[19] W. J. Freeman and J. M. Barrie, *Analysis of spatial patterns of phase in neocortical gamma EEGs in rabbit*, Journal of Neurophysiology **84** (2000), 1266–1278.

[20] M. Gerhardt, H. Schuster, and J. J. Tyson, *A cellular automaton model of excitable media including curvature and dispersion*, Science **247** (1990), 1563–1566.

[21] B. J. Glasser, I. G. Kevrekidis, and S. Sundaresan, *One- and two-dimensional travelling wave solutions in gas-fluidized beds*, Journal of Fluid Mechanics **306** (1996), 183–221.

[22] M. Grace and M.-T. Hütt, *Predictability of spatio-temporal patterns in a lattice of coupled FitzHugh–Nagumo oscillators*, Journal of the Royal Society Interface **10** (2013), 20121016.

[23] D. M. Grobman, *Homeomorphism of systems of differential equations*, Doklady Akademii Nauk SSSR **128** (1959), 880–881, In Russian.

[24] D. M. Grobman, *Topological classification of neighborhoods of a singularity in n-space*, Matematicheskii Sbornik **56(98)** (1962), 77–94, In Russian.

[25] J. Guckenheimer and P. J. Holmes, *Nonlinear oscillations, dynamical systems, and bifurcations of vector fields*, Applied Mathematical Sciences, vol. 42, Springer-Verlag, New York, 1983.

[26] J. Guckenheimer and C. Kuehn, *Homoclinic orbits of the Fitzhugh-Nagumo equation: the singular-limit*, Discrete and Continuous Dynamical Systems Series S **2** (2009), 851–875.

[27] J. Guckenheimer and C. Kuehn, *Homoclinic orbits of the Fitzhugh-Nagumo equation: Bifurcations in the full system*, SIAM Journal of Applied Dynamical Systems **9** (2010), 138–153.

[28] M. Haissaguerre, M. Hocini, A. Denis, A. J. Shah, Y. Komatsu, S. Yamashita, M. Daly, and et al., *Driver domains in persistent atrial fibrillation*, Circulation **130** (2014), 530–538.

[29] M. E. Harris-White, S. A. Zanotti, S. A. Frautschy, and A. C. Charles, *Spiral intercellular calcium waves in hippocampal slice cultures*, Journal of Neurophysiology **79** (1998), 1045–1052.

[30] P. Hartman, *A lemma in the theory of structural stability of differential equations*, Proceedings of the American Mathematical Society **11** (1960), 610–620.

[31] P. Hartman, *On the local linearization of differential equations*, Proceedings of the American Mathematical Society **14** (1963), 568–573.

[32] G. He, Z. Cao, H. Chen, and P. Zhu, *Controlling chaos in a neural network based on the phase space constraint*, International Journal of Modern Physics B **17** (2003), 4209–4214.

[33] G. He, Z. Cao, P. Zhu, and H. Ogura, *Controlling chaos in a chaotic neural network*, Neural Networks **16** (2003), 1195–1200.

[34] G. He, L. Chen, and K. Aihara, *Associative memory with a controlled chaotic neural network*, Neurocomputing **71** (2008), 2794–2805.

[35] G. He, M. D. Shrimali, and K. Aihara, *Partial state feedback control of chaotic neural network and its application*, Physics Letters A **371** (2007), 228–233.

[36] G. He, M. D. Shrimali, and K. Aihara, *Threshold control of chaotic neural network*, Neural Networks **21** (2008), 114–121.

[37] P. Hirschberg and E. Knobloch, *An unfolding of the Takens-Bogdanov singularity*, Quarterly of Applied Mathematics **49** (1991), 281–287.

[38] X. Huang, W. C. Troy, Q. Yang, H. Ma, C. R. Laing, S. J. Schiff, and J.-Y. Wu, *Spiral waves in disinhibited mammalian neocortex*, The Journal of Neuroscience **24** (2004), 9897–9902.

[39] X. Huang, W. Xu, J. Liang, K. Takagaki, X. Gao, and J.-Y. Wu, *Spiral wave dynamics in neocortex*, Neuron **68** (2010), 978–990.

[40] W. Jiang and Y. Yuan, *Bogdanov–Takens singularity in Van der Pol's oscillator with delayed feedback*, Physica D: Nonlinear Phenomena **227** (2007), 149–161.

[41] K. Kaneko and T. Yanagita, *Coupled maps*, Scholarpedia **9** (2014), no. 5, 4085.

[42] R. Kapral and K. Showalter (eds.), *Chemical wave and patterns*, Understanding Chemical Reactivity, vol. 10, Springer Science+Business Media, Dordrecht, the Netherlands, 1995.

[43] J. P. Keener and J. J. Tyson, *Spiral waves in the Belousov-Zhabotinskii reaction*, Physica D: Nonlinear Phenomena **21** (1986), 307–324.

[44] P. Kent and J. Elgin, *Travelling-waves of the Kuramoto–Sivashinsky equation: period-multiplying bifurcations*, Nonlinearity **5** (1992), 899–919.

[45] N. Kopell and L. N. Howard, *Plane wave solutions to reaction-diffusion equations*, Studies in Applied Mathematics **52** (1973), 291–328.

[46] J. Kuroiwa, N. Masutani, S. Nara, and K. Aihara, *Sensitive response of a chaotic wandering state to memory fragment inputs in a chaotic neural network model*, International Journal of Bifurcation and Chaos **14** (2004), 1413–1421.

[47] Yu. A. Kuznetsov, *Elements of applied bifurcation theory*, 3 ed., Applied Mathematical Sciences, vol. 112, Springer-Verlag, New York, 2004.

[48] Yu. A. Kuznetsov, *Practical computation of normal forms on center manifolds at degenerate Bogdanov–Takens bifurcations*, International Journal of Bifurcation and Chaos **15** (2005), 3535–3546.

[49] Yu. A. Kuznetsov, H. G. E. Meijer, B. Al-Hdaibat, and W. Govaerts, *Improved homoclinic predictor for Bogdanov–Takens bifurcation*, International Journal of Bifurcation and Chaos **24** (2014), 1450057.

[50] Yuri. A. Kuznetsov, *Numerical normalization techniques for all codim 2 bifurcations of equilibria in ODE's*, SIAM Journal on Numerical Analysis **36** (1999), 1104–1124.

[51] Y.-W. Lam, L. B. Cohen, and M. R. Zochowski, *Odorant specificity of three oscillations and the DC signal in the turtle olfactory bulb*, European Journal of Neuroscience **17** (2003), 436–446.

[52] Y. Li, P. Zhu, X. Xie, H. Chen, K. Aihara, and G. He, *Controlling a chaotic neural network for information processing*, Neurocomputing **110** (2013), 111–120.

[53] Y. Lu, W. Truccolo, F. B. Wagner, C. E. Vargas-Irwin, I. Ozden, J. B. Zimmermann, T. May, N. S. Agha, J. Wang, and A. V. Nurmikko, *Optogenetically induced spatiotemporal gamma oscillations and neuronal spiking activity in primate motor cortex*, Journal of Neurophysiology **113** (2015), 3574–3587.

[54] E. V. Lubenov and A. G. Siapas, *Hippocampal theta oscillations are travelling waves*, Nature **459** (2009), 534–539.

[55] J. Luengviriya, P. Porjai, M. Phantu, M. Sutthiopad, B. Tomapatanaget, and M *Meandering spiral waves in a bubble-free Belousov–Zhabotinsky reaction with pyrogallol*, Chemical Physics Letters **588** (2013), 267–271.

[56] X.-S. Luo, *Using phase space compression to control chaos and hyperchaos*, Acta Physica Sinica **48** (1999), 402–407, in Chinese.

[57] J. Ma, Y. Jia, C.-N. Wang, and W.-Y. Jin, *Transition of spiral wave in a model of two-dimensional arrays of Hindmarsh–Rose neurons*, International Journal of Modern Physics B **25** (2011), 1653–1670.

[58] J. Ma, Y. Jia, M. Yi, J. Tang, and Y.-F. Xia, *Suppression of spiral wave and turbulence by using amplitude restriction of variable in a local square area*, Chaos, Solitons and Fractals **41** (2009), 1331–1339.

[59] J. Ma, C.-N. Wang, W.-Y. Jin, and Y. Wu, *Transition from spiral wave to target wave and other coherent structures in the networks of Hodgkin–Huxley neurons*, Applied Mathematics and Computation **217** (2010), 3844–3852.

[60] S. C. Mancas and S. R. Choudhury, *Traveling wavetrains in the complex cubic–quintic Ginzburg–Landau equation*, Chaos, Solitons and Fractals **28** (2006), 834–843.

[61] J. M. McNamee and V. Y. Pan, *Numerical methods for roots of polynomials* II, Studies in Computational Mathematics, vol. 16, Elsevier, Amsterdam, Netherlands, 2013.

[62] F. Mellibovsky and B. Eckhardt, *Takens–Bogdanov bifurcation of travelling-wave solutions in pipe flow*, Journal of Fluid Mechanics **670** (2011), 96–129.

[63] H. Miyagi, T. Ohshiro, and K. Yamashita, *Generalized Lyapunov function for Liénard-type non-linear systems*, International Journal of Control **48** (1988), 805–812.

[64] I. M. Moroz, R. Hide, and A. M. Soward, *On self-exciting coupled Faraday disk homopolar dynamos driving series motors*, Physica D: Nonlinear Phenomena **117** (1998), 128–144.

[65] M. Murata, *Multidimensional traveling waves in the Allen–Cahn cellular automaton*, Journal of Physics A: Mathematical and Theoretical **48** (2015), 255202.

[66] M. Oku and K. Aihara, *Associative dynamics of color images in a large-scale chaotic neural network*, Nonlinear Theory and Its Applications, IEICE **2** (2011), 508–521.

[67] M. Oku and K. Aihara, *Traveling waves in locally connected chaotic neural networks and their phenomenological modeling*, Advances in Cognitive Neurodynamics (III): Proceedings of the Third International Conference on Cognitive Neurodynamics - 2011 (Dordrecht, Netherlands) (Y. Yamaguchi, ed.), Springer Netherlands, 2013, pp. 213–219.

[68] S. V. Pandit and J. Jalife, *Rotors and the dynamics of cardiac fibrillation*, Circulation Research **112** (2013), 849–862.

[69] J. Park, *Bifurcation and stability of the generalized complex Ginzburg–Landau equation*, Communications on Pure and Applied Analysis **7** (2008), 1237–1253.

[70] J. Park and P. Strzelecki, *Bifurcation to traveling waves in the cubic–quintic complex Ginzburg–Landau equation*, Analysis and Applications **13** (2015), 395–412.

[71] T. M. Patten, C. J. Rennie, P. A. Robinson, and P. Gong, *Human cortical traveling waves: dynamical properties and correlations with responses*, PLoS ONE **7** (2012), e38392.

[72] G. Peng and Y. Jiang, *Computation of universal unfolding of the double-zero bifurcation in $\mathbf{Z}_2$-symmetric systems by a homological method*, Journal of Difference Equations and Applications **19** (2013), 1501–1512.

[73] O. Peters, C. G. Schipke, Y. Hashimoto, and H. Kettenmann, *Different mechanisms promote astrocyte Ca^{2+} waves and spreading depression in the mouse neocortex*, The Journal of Neuroscience **23** (2003), 9888–9896.

[74] S. V. Petrovskii and H. Malchow, *A minimal model of pattern formation in a prey-predator system*, Mathematical and Computer Modelling **29** (1999), 49–63.

[75] L. Pivka, *Autowaves and spatio-temporal chaos in CNNs—Part I: A tutorial*, IEEE Transactions on Circuits and Systems I: Fundamental Theory and Applications **42** (1995), 638–649.

[76] O. Podvigina, V. Zheligovsky, E. L. Rempel, A. C.-L. Chian, R. Chertovskih, and P. Muñoz, *Two-parameter bifurcation study of the regularized long-wave equation*, Physical Reivew E **92** (2015), 032906.

[77] J. D. M. Rademacher and B. Sandstede, *Computing absolute and essential spectra using continuation*, Physica D: Nonlinear Phenomena **229** (2007), 166–183.

[78] D. Rubino, K. A. Robbins, and N. G. Hatsopoulos, *Propagating waves mediate information transfer in the motor cortex*, Nature Neuroscience **9** (2006), 1549–1557.

[79] T. K. Sato, I. Nauhaus, and M. Carandini, *Traveling waves in visual cortex*, Neuron **75** (2012), 218–229.

[80] B. Schmidt and M *Forced parallel drift of spiral waves in the Belousov-Zhabotinsky reaction*, Physical Reiview E **55** (1997), 4390–4393.

[81] J. A. Sherratt, *Numerical continuation methods for studying periodic travelling wave (wavetrain) solutions of partial differential equations*, Applied Mathematics and Computation **218** (2012), 4684–4694.

[82] J. A. Sherratt, *Numerical continuation of boundaries in parameter space between stable and unstable periodic travelling wave (wavetrain) solutions of partial differential equations*, Advances in Computational Mathematics **39** (2013), 175192.

[83] A. N. Shoshitaishvili, *Bifurcations of topological type at singular points of parametrized vector fields*, Funktsional. Anal. i Prilozhen. **6** (1972), 97–98, in Russian, with English translation Functional Analysis and Its Applications **6**(2), 169–170.

[84] S. Sinha, A. Pande, and R. Pandit, *Defibrillation via the elimination of spiral turbulence in a model for ventricular fibrillation*, Physical Review Letters **86** (2001), 3678–3681.

[85] S. Sinha and S. Sridhar, *Patterns in excitable media: Genesis, dynamics, and control*, CRC Press, Boca Raton, FL, 2014.

[86] C. A. Skarda and W. J. Freeman, *How brains make chaos in order to make sense of the world*, Behavioral and Brain Sciences **10** (1987), 161–173.

[87] L. B. Smolka, B. Marts, and A. L. Lin, *Effect of inhomogeneities on spiral wave dynamics in the Belousov-Zhabotinsky reaction*, Physical Review E **72** (2005), 056205.

[88] J. Sneyd, A. LeBeau, and D. Yule, *Traveling waves of calcium in pancreatic acinar cells: model construction and bifurcation analysis*, Physica D: Nonlinear Phenomena **145** (2000), 158–179.

[89] K. Takagaki, C. Zhang, J.-Y. Wu, and F. W. Ohl, *Flow detection of propagating waves with temporospatial correlation of activity*, Journal of Neuroscience Methods **200** (2011), 207–218.

[90] K. Takahashi, M. Saleh, R. D. Penn, and N. G. Hatsopoulos, *Propagating waves in human motor cortex*, Frontiers in Human Neuroscience **5** (2011), 40.

[91] S. Titz, T. Kuhlbrodt, and U. Feudel, *Homoclinic bifurcation in an ocean circulation box model*, International Journal of Bifurcation and Chaos **12** (2002), 869–875.

[92] S. Tsuji, T. Ueta, H. Kawakami, H. Fujii, and K. Aihara, *Bifurcations in two-dimensional Hindmarsh–Rose type model*, International Journal of Bifurcation and Chaos **17** (2007), 985–998.

[93] V. K. Vanag and I. R. Epstein, *Segmented spiral waves in a reaction-diffusion system*, Proceedings of the National Academy of Sciences of the United states of America **100** (2003), 14635–14638.

[94] J. Viventi, D.-H. Kim, L. Vigeland, E. S. Frechette, J. A. Blanco, Y.-S. Kim, and et al., *Flexible, foldable, actively multiplexed, high-density electrode array for mapping brain activity in vivo*, Nature Neuroscience **14** (2011), 1599–1605.

[95] V. Volpert and S. Petrovskii, *Reaction–diffusion waves in biology*, Physics of Life Reviews **6** (2009), 267–310.

[96] C.-N. Wang, J. Ma, Y. Liu, and L. Huang, *Chaos control, spiral wave formation, and the emergence of spatiotemporal chaos in networked Chua circuits*, Nonlinear Dynamics **67** (2012), 139–146.

[97] Z. Wang, H. Fan, and K. Aihara, *An associative network with chaotic neurons and dynamic synapses*, International Journal of Bifurcation and Chaos **17** (2007), 3085–3097.

[98] A. T. Winfree, *Varieties of spiral wave behavior: An experimentalist's approach to the theory of excitable media*, Chaos **1** (1991), 303–334.

[99] J.-Y. Wu, L. Guan, and Y. Tsau, *Propagating activation during oscillations and evoked responses in neocortical slices*, The Journal of Neuroscience **19** (1999), 5005–5015.

[100] J.-Y. Wu, X. Huang, and C. Zhang, *Propagating waves of activity in the neocortex: what they are, what they do*, The Neuroscientist **14** (2008), 487–502.

[101] Y. Yi and Z. Liu, *The bifurcations of traveling wave solutions of the Kundu equation*, Journal of Applied Mathematics **2013** (2013), 137475.

[102] G. Yu, J. Ma, Y. Jia, and J. Tang, *Dynamics of spiral wave in the coupled Hodgkin–Huxley neurons*, International Journal of Modern Physics B **24** (2010), 4555–4562.

[103] H. Zhang, B. Hu, and G. Hu, *Suppression of spiral waves and spatiotemporal chaos by generating target waves in excitable media*, Physical Review E **68** (2003), 026134.

[104] H. Zhang and J. Jacobs, *Traveling theta waves in the human hippocampus*, The Journal of Neuroscience **35** (2015), 12477–12487.

[105] K. Zhang and J. Han, *Bifurcations of traveling wave solutions for the* $(2 + 1)$*-dimensional generalized asymmetric Nizhnik–Novikov–Veselov equation*, Applied Mathematics and Computation **251** (2015), 108–117.

[106] Y. Zhao, S. A. Billings, and A. F. Routh, *Identification of excitable media using cellular automata models*, International Journal of Bifurcation and Chaos **17** (2007), 153–168.

[107] H. Zhu, S. A. Campbell, and G. S. K. Wolkowicz, *Bifurcations analysis of a predator-prey system with nonmonotonic functional response*, SIAM Journal on Applied Mathematics **63** (2002), 636–682.

[108] M. G. Zimmermann, M. A. Natiello, and H. G. Solari, *Global bifurcations in a laser with injected signal: Beyond Adler's approximation*, Chaos **11** (2001), 500–513.